

FACULTY OF ENGINEERING
DEPARTMENT OF CIVIL ENGINEERING
STRUCTURAL MECHANICS
KASTEELPARK ARENBERG 40 B-3001 LEUVEN



KATHOLIEKE
UNIVERSITEIT
LEUVEN

ENGINEERING DEPARTMENT
MECHANICS, MATERIALS AND DESIGN
DYNAMICS AND VIBRATION
TRUMPINGTON STREET CB2 1PZ CAMBRIDGE UK



CAMBRIDGE
UNIVERSITY

The vibration response of piled foundations to inertial and underground railway induced loadings

Promoters:
prof. dr. ir. G. Degrande
dr. ir. H.E.M. Hunt

Assessors:
ir. K.A. Kuo
dr. ir. S. François

A dissertation submitted
for the degree of
Civil Engineer

by

Pieter COULIER

FACULTY OF ENGINEERING
DEPARTMENT OF CIVIL ENGINEERING
STRUCTURAL MECHANICS
KASTEELPARK ARENBERG 40 B-3001 LEUVEN



KATHOLIEKE
UNIVERSITEIT
LEUVEN

ENGINEERING DEPARTMENT
MECHANICS, MATERIALS AND DESIGN
DYNAMICS AND VIBRATION
TRUMPINGTON STREET CB2 1PZ CAMBRIDGE UK



CAMBRIDGE
UNIVERSITY

The vibration response of piled foundations to inertial and underground railway induced loadings

Promotors:
prof. dr. ir. G. Degrande
dr. ir. H.E.M. Hunt

Assessors:
ir. K.A. Kuo
dr. ir. S. François

A dissertation submitted
for the degree of
Civil Engineer

by

Pieter COULIER

© Copyright by K.U.Leuven

Without written permission of the promotors and the author it is forbidden to reproduce or adapt in any form or by any means any part of this publication. Requests for obtaining the right to reproduce or utilize parts of this publication should be addressed to K.U.Leuven, Faculty of Engineering - Kasteelpark Arenberg 1, B-3001 Heverlee (Belgium). Tel. +32-16 32 13 50 & Fax. +32-16 32 19 88.

A written permission of the promotors and the author is also required to use the methods, products, schematics and programs described in this work for industrial or commercial use, and for submitting this publication in scientific contests.

To Papa, Moeke, Nele & Lara

Our greatest weakness lies in giving up. The most certain way to succeed is always to try just one more time.

Thomas Alva Edison (1847-1931)

If we knew what we were doing, it wouldn't be called research, would it?

Albert Einstein (1879-1955)

Preface

This MSc thesis is the culmination of my career as a student in civil engineering. The work described in this dissertation was carried out at Cambridge University and K.U.Leuven between September 2009 and May 2010, within the frame of an Erasmus exchange programme.

I wish to thank my promotors Professor Geert Degrande and Dr. Hugh Hunt for their believe in me, the motivating support and the knowledgeable guidance. Without their help, this unique experience would not have been possible. I am also greatly indebted to Kirsty Kuo for her enormous encouragement and enthusiastic guidance. I would like to thank her for the interest in my work and the useful discussions we had. Furthermore, I am grateful to Stijn François for proofreading this dissertation and for his helpful comments.

I would like to thank Trinity College for giving me the opportunity to be accommodated in such an exciting environment from September 2009 until January 2010. I also want to extend a word of thanks to my colleagues at the DVRO who have helped to make this research experience very enjoyable.

I would like to thank all my friends at the university for making the five years of studying in Leuven an interesting and pleasurable part of my life. Finally, I owe much gratitude to my parents and grandparents for their endless support. Without their help, I would not be the person that I am today.

Pieter Coulier
May 2010

Summary

Vibrations and re-radiated noise in buildings induced by (underground) railway traffic are a major environmental concern. Vibrations are generated at the wheel-rail interface and propagate through the soil into buildings, where they cause annoyance to inhabitants. During the last decades, a lot of research has been performed to search for efficient and cost-effective vibration countermeasures.

This dissertation is concerned with the dynamic behaviour of piled foundations. A model for piled foundations which accounts for the fundamental behaviour of each pile and the interaction between neighbouring piles, through wave propagation in the soil, is developed. It is a boundary element model, formulated in the frequency domain, based on an existing single pile model.

The model is used to validate the Pipe-in-Pipe (PiP) model for piles, a computationally efficient model for piled foundations based on the homonymic model for vibrations from underground railways. The models are found to be in good agreement, which offers great perspectives to use the PiP model as an engineering tool.

The influence of adjacent piles on the response of a certain pile is investigated by means of a power flow analysis. It will be demonstrated that the effect is strongly dependent on the relative positions of the piles compared to the position of the load applied. Moreover, a tendency to wave scattering is revealed when the wavelength approaches the distance between piles and load.

Ultimately, the response of piled foundations to underground railway induced loadings is investigated. Uncoupling of source (railway track) and receiver (piled foundations) is assumed, resulting in a two-step approach. The model is once more used to validate the PiP model for piles. Several aspects, such as the effect of the foundation design, the contribution of horizontal and rotational motion, the importance of pile-soil-pile interactions and the isolation performance of base isolation are examined. Results suggest that steel springs are preferred to rubber bearings, as the isolation frequency can be lowered more significantly. Moreover, it will become clear that the current boundary element model has the ability to reveal the complexity of the situation, which cannot be achieved by means of simplified models.

Samenvatting

Trillingen en herafgestraald geluid in gebouwen veroorzaakt door (ondergronds) spoorverkeer zijn een belangrijke vorm van milieuhinder die steeds meer aandacht krijgt. Trillingen worden gegenereerd door de dynamische interactie tussen de wielen en de rails. Ze planten zich voort als elastische golven in de ondergrond en exciteren nabijgelegen gebouwen via de funderingen, wat hinder veroorzaakt voor de bewoners. Gedurende de laatste decennia is er uitgebreid onderzoek verricht naar efficiënte en rendabele maatregelen om deze hinder te beperken.

Deze verhandeling heeft betrekking op het dynamisch gedrag van paalfunderingen. Er wordt een model voor paalfunderingen ontwikkeld dat zowel het fundamenteel gedrag van elke paal als de interactie tussen nabije palen inrekent. Het betreft een randelementenmodel, geformuleerd in het frequentiedomein, en is gebaseerd op een bestaand model voor één enkele paal.

Het model wordt gebruikt om het *Pipe-in-Pipe* (PiP) model voor palen te valideren. Dit is een rekenkundig efficiënt model voor paalfunderingen, en is gebaseerd op het gelijknamige model voor trillingen ten gevolge van ondergronds spoorverkeer. Uit de resultaten blijkt er een goede overeenstemming te zijn tussen beide modellen, wat perspectieven biedt om het PiP model voor palen als ingenieurstoepassing te gebruiken.

De invloed van naburige palen op de respons van een bepaalde paal wordt onderzocht door middel van een *power flow* analyse. Er wordt aangetoond dat deze invloed sterk afhankelijk is van de relatieve posities van de beschouwde palen ten opzichte van de locatie van de aangebrachte last. Verder wordt een tendens tot golfverstrooiing waargenomen als de golflengte de afstand tussen de palen en de belasting benadert.

Tenslotte wordt de respons van paalfunderingen op door ondergronds spoorverkeer geïnduceerde trillingen onderzocht. Er wordt een ontkoppeling van de bron (spoor) en de ontvanger (paalfundering) verondersteld, wat resulteert in een numerieke modellering bestaande uit twee stappen. Het model wordt eens te meer gebruikt om het PiP model voor palen te valideren. Verschillende aspecten, zoals het effect van het funderingsontwerp, de bijdrage van horizontale en rotationele trillingen, het belang van paalinteracties en de efficiëntie van isoleringsmaatregelen worden onderzocht. De resultaten suggereren dat stalen veren te verkiezen zijn boven rubberen ondersteuning, aangezien er lagere isolatiefrequenties kunnen bekomen worden. Bovendien blijkt dat het ontwikkelde randelementenmodel over het vermogen beschikt om de complexiteit van de situatie te onthullen, iets wat niet bereikt kan worden door middel van vereenvoudigde modellen.

Contents

Preface	i
Summary	ii
Samenvatting	iii
Contents	iv
List of Figures	xii
List of Tables	xii
List of Symbols	xiii
1 Introduction	1
1.1 Ground-borne vibrations	1
1.2 Modelling the source and receiver	2
1.3 Objectives of the research	3
1.4 Outline of the dissertation	4
2 The single pile BE model	5
2.1 The soil and the soil-pile interface	6
2.2 The pile model	8
2.2.1 Longitudinal behaviour	8
2.2.2 Transverse behaviour	9
2.2.3 The assembled pile model	11
2.3 Coupling the pile and soil	12

2.4	Validation and illustration	13
2.5	Conclusion	14
3	Extensions of the single pile BE model	16
3.1	Timoshenko beam theory	16
3.1.1	Equations	16
3.1.2	Results	19
3.2	Power flow analysis	21
3.3	Incorporation of a building model: a semi-infinite column	25
3.4	Geometrical extensions	31
3.5	Conclusion	31
4	Validation of the PiP model for piles	32
4.1	The PiP model for piles	32
4.2	Infinite pile	32
4.2.1	Equations	33
4.2.2	Comparison	33
4.3	Finite pile	36
4.3.1	Equations	36
4.3.2	Comparison	36
4.4	Conclusion	38
5	The multiple pile BE model	39
5.1	Two adjacent piles with unconstrained pile-heads	39
5.1.1	Equations	39
5.1.2	Validation	42
5.1.3	Illustration	45
5.2	Two adjacent piles with semi-infinite columns	48
5.2.1	Equations	48
5.2.2	Illustration	48
5.3	Conclusion	49
6	The shadow effect	50

6.1	Introduction	50
6.2	Models	50
6.3	Results	51
6.3.1	Vertical point load at 25 Hz	51
6.3.2	Vertical point load at frequencies up to 80 Hz	53
6.4	Conclusion	55
7	The response of piled foundations to underground railway induced loadings	56
7.1	Validation of the two-step approach (subdomain formulation)	57
7.2	The Pipe-in-Pipe model for underground railways	59
7.3	The BE pile model	60
7.4	Results for a single pile	61
7.5	Results for a four-pile group	63
7.6	Case study	64
7.6.1	Comparison of the pile designs	65
7.6.2	The significance of horizontal and rotational motion	66
7.6.3	The significance of pile-soil-pile interactions (PSPI)	67
7.6.4	Efficiency of base isolation	68
7.7	Conclusion	69
8	Conclusions and recommendations for further work	70
8.1	Conclusions	70
8.2	Recommendations for further work	71
	Bibliography	72
A	Integral transformations	A-1
A.1	Fourier transform with respect to time	A-1
A.2	Fourier transform with respect to a spatial coordinate	A-1
B	The Boundary Element Method	B-1
B.1	The elastodynamic problem	B-1
B.2	The dynamic (Betti-Rayleigh) reciprocity theorem	B-2

B.3	The fundamental solution	B-2
B.4	The boundary integral equations	B-3
B.5	Numerical solution	B-4
C	Transformation matrix for coupling the pile and soil	C-1
D	The Pipe-in-Pipe model for underground railways	D-1
D.1	The original PiP model for a tunnel in a full-space	D-1
D.1.1	Modelling the track and train	D-2
D.1.2	Elastic continuum equations	D-3
D.1.3	Modelling the tunnel	D-5
D.1.4	Modelling the soil	D-6
D.1.5	Coupling the tunnel and the soil	D-6
D.2	The modified PiP model for a tunnel in a half-space	D-7
D.2.1	Displacements at the tunnel-soil interface	D-7
D.2.2	The equivalent internal source	D-8
D.2.3	The far-field displacements	D-9
E	Matrix expressions	E-1
E.1	Two adjacent piles with unconstrained pile-heads	E-1
E.2	Two adjacent piles with semi-infinite columns	E-2
E.3	Tunnel and piles with semi-infinite columns	E-3
E.3.1	Two piles	E-3
E.3.2	Four piles	E-4

List of Figures

1.1	Vibrations from multiple sources propagate through and along the surface of the ground, interacting with buried objects, before being perceived in the building as vibration or re-radiated noise [46].	2
2.1	The boundary element mesh of the single pile model developed by Talbot [46], here for the case of $N_1 = N_2 = 21$, $N_{sp} = 85$	6
2.2	Pile model (drawn horizontally), for the case of $N_p = 6$. The dots represent the nodes, the dashed lines delimit the boundary elements of the soil-pile interface. Only the (x_1, x_3) -plane is shown.	8
2.3	Illustration of the coupling between the soil and pile models. All pile nodes are coupled to those of the surrounding boundary elements (represented by dashed lines), except the pile-head node. The free surface discretization is not shown.	12
2.4	Displacement field predicted by the single pile BE model due to a unit vertical load applied at the pile-head, at 50 Hz. The three-dimensional view (a) clearly illustrates the concentric circular wavefronts. The vertical cross-section (b) shows that the model correctly predicts the Rayleigh wavelength of 3.75 m.	15
3.1	Lateral deformation of a Timoshenko beam. Note that the normal rotates by an amount β_{x_2} which is not equal to $\frac{\partial u_1}{\partial x_3}$	18
3.2	Flexibility coefficients (a) F_{11} , (b) F_{33} , (c) F_{44} and (d) F_{41} vs. dimensionless frequency a_0 , as computed using Euler beam theory (dashed line) and Timoshenko beam theory (solid line). The real parts I_{ij} are given as plain lines, while the absolute value of the imaginary parts J_{ij} are marked by crosses. Following parameters are used in the calculation: $L_p/d_p = 10.6$, $\mu_p/\mu_s = 100$, $\rho_s/\rho_p = 0.75$, $\nu_s = 0.40$ and $\nu_p = 0.25$	20
3.3	Power flow analysis for a unit (a)-(b) horizontal, (c)-(d) vertical and (e)-(f) moment load \mathbf{f}_{ph} applied at the pile-head. Figures (a), (c) and (e) clearly demonstrate the conservation of energy. The power flow distribution at 25 Hz is illustrated in (b), (d) and (f). The pile body is filled with a grey shadow of which the darkness indicates the magnitude of the power flowing through the pile's section. The arrows perpendicular to the boundary elements correspond to power flowing through the pile skin.	23

3.4	Power flow analysis for a prescribed horizontal traction \mathbf{p}_{fs} at a distance $R = 3.50$ m from the pile-head. Figure (a) clearly demonstrates the conservation of energy. The power flow distribution at 25 Hz is illustrated in (b).	24
3.5	Representation of the simplistic building model.	25
3.6	Longitudinal excitation of a semi-infinite bar.	25
3.7	Power flow analysis for a prescribed horizontal traction \mathbf{p}_{fs} at a distance $R = 3.50$ m from the pile-head. A simplistic building model is incorporated in the model. Figure (a) clearly demonstrates the conservation of energy. The power flow distribution at 25 Hz is illustrated in (b).	29
3.8	Representation of the simplistic base-isolated building model.	29
3.9	Three modes of deformation of a rubber isolation bearing.	30
3.10	Coupling of the pile and the base-isolated semi-infinite column at the pile-head.	31
3.11	Possible approximations of the circular pile soil interface (top view).	31
4.1	Relative magnitude of (a) transverse and (b) longitudinal pile displacements in a full-space, in function of the longitudinal coordinate and the frequency. The zero pile coordinate indicates the excitation point.	34
4.2	Transverse driving point FRF of an infinite pile vs. dimensionless frequency a_0 , as computed using configuration 1 (crossed line), configuration 2 (dash-dot line), configuration 3 (dotted line), configuration 4 (dashed line) and the PiP model for piles (solid line).	35
4.3	Longitudinal driving point FRF of an infinite pile vs. dimensionless frequency a_0 , as computed using configuration 1 (crossed line), configuration 2 (dash-dot line), configuration 3 (dotted line), configuration 4 (dashed line) and the PiP model for piles (solid line).	36
4.4	Transverse driving point FRF of a finite pile vs. dimensionless frequency a_0 , as computed using configuration 1 (dotted line), configuration 2 (dash-dot line), configuration 3 (dashed line) and the PiP model for piles (solid line).	37
4.5	Longitudinal driving point FRF of a finite pile vs. dimensionless frequency a_0 , as computed using configuration 1 (dotted line), configuration 2 (dash-dot line), configuration 3 (dashed line) and the PiP model for piles (solid line).	38
5.1	Schematic illustration of two adjacent piles.	39
5.2	Dynamic interaction factors α_{ij} vs. dimensionless frequency a_0 , as computed using configuration 1 (dotted line), configuration 2 (dash-dot line), configuration 3 (dashed line) and Kaynia's model (solid line). The real parts $\Re(\alpha_{ij})$ are given as plain lines, while the imaginary parts $\Im(\alpha_{ij})$ are marked by crosses.	44

5.3	Real and imaginary parts of the dynamic interaction factors α_{ij} vs. dimensionless frequency a_0 , as computed using configuration 1 (dotted line), configuration 2 (dash-dot line), configuration 3 (dashed line), the PiP model for piles (solid line) and Kaynia's model (circles). The different pile separation distances s are marked on the figures.	45
5.4	Displacement field (multiplied with a factor 2×10^9) predicted by the multiple pile BE model due to a unit vertical load applied at pile-head A, at 50 Hz.	46
5.5	Power flow analysis for a prescribed horizontal traction \mathbf{p}_{fs} collinear with the piles. The load is located at a distance $R = 1.50$ m from pile-head A, while the centre-to-centre spacing s between the piles equals 2 m. Figure (a) clearly demonstrates the conservation of energy. The power flow distribution at 25 Hz is illustrated in (b).	47
5.6	Power flow analysis for a prescribed horizontal traction \mathbf{p}_{fs} collinear with the piles. The load is located at a distance $R = 1.50$ m from pile-head A, while the centre-to-centre spacing s between the piles equals 2 m. A simplistic building model is incorporated in the model. Figure (a) clearly demonstrates the conservation of energy. The power flow distribution at 25 Hz is illustrated in (b).	49
6.1	Single pile.	50
6.2	Pile in the shadow of another one.	51
6.3	Shadow effect for a unit vertical load at 25 Hz.	52
6.4	Power flow insertion gain vs. angle β , for a unit vertical load at 25 Hz.	52
6.5	Power flow insertion gain as a function of angle β and frequency f , for a unit vertical load.	53
6.6	Two adjacent piles with centre-to-centre spacing $s = 2$ m. A unit vertical load is applied at a location characterized by $R = 3.50$ m and $\beta = 90^\circ$	54
6.7	Power flow distribution around the pile-heads of (a) the original single pile and (b) the shadowed pile, due to a unit vertical load at 25 Hz, applied at a location characterized by $R = 3.50$ m and $\beta = 90^\circ$	54
6.8	Power flow distribution around the pile-heads of (a) the original single pile and (b) the shadowed pile, due to a unit vertical load at 75 Hz, applied at a location characterized by $R = 3.50$ m and $\beta = 90^\circ$	54
7.1	Illustration of the two-step approach used to calculate the response of piled foundations to underground railway induced vibrations. (a) The PiP model for underground railways is utilized to calculate displacements and tractions in the soil, and (b) these are applied as generalized loadings to the BE pile model.	57
7.2	Real and imaginary parts of the pile-head responses H_{ii} vs. dimensionless frequency a_0 , as computed straightforwardly (solid line) and using the subdomain formulation (dashed line).	58

7.3	Location of a single pile with length $L_p = 20$ m. The tunnel is located at a depth of 25 m beneath the free surface, and the pile has an offset of 10 m with respect to the tunnel axis. The horizontal (u_2^{ph}) and vertical (u_3^{ph}) pile-head response are investigated.	61
7.4	(a)-(b) Horizontal and (c)-(d) vertical pile-head response due to underground railway induced loadings, with comparison to the greenfield vibration levels (bold line). The results are calculated using Novak's model (dotted line), the PiP model for piles (solid line) and the BE pile model (circles).	62
7.5	Vertical pile-head response of (a) the outer and (b) the inner piles due to underground railway induced loadings, with comparison to the greenfield vibration levels (bold line). The results are calculated using the PiP model for piles (solid line) and the BE pile model (circles).	63
7.6	Two different pile designs analysed in the case study.	64
7.7	Power flow analysis for the two-pile (dashed line) and four-pile (solid line) design. The plain lines represent \bar{P}_{in} , while the circles represent \bar{P}_{out} .	65
7.8	Power flow distribution for (a) the four-pile and (b) the two-pile design at 25 Hz.	66
7.9	Relative contribution of the horizontal $\bar{P}_{\text{hor}}/\bar{P}_{\text{tot}}$ (dashed line), vertical $\bar{P}_{\text{ver}}/\bar{P}_{\text{tot}}$ (solid line) and rotational $\bar{P}_{\theta}/\bar{P}_{\text{tot}}$ (dotted line) components to the total mean power flow into the semi-infinite columns of (a) the outer and (b) the inner piles.	67
7.10	Horizontal \bar{P}_{hor} (dashed line), vertical \bar{P}_{ver} (solid line) and rotational \bar{P}_{θ} (dotted line) components of the total mean power flow into the semi-infinite columns of (a) the outer and (b) the inner piles.	67
7.11	Total mean power flow into the semi-infinite columns vs. frequency f , as computed using the current BE pile model (solid line) and a model that disregards PSPI (dashed line).	68
7.12	Total mean power flow into the semi-infinite columns vs. frequency f , in case of an unisolated building model (solid line) and in case of base isolation with isolation frequencies of 15 Hz (dashed line), 10 Hz (dash-dot line) and 5 Hz (dotted line).	69
B.1	Two elastodynamic states of the body Ω . The infinite domain is represented by the dashed circle [46].	B-4
B.2	Transformation from the global coordinate system (x_1, x_2, x_3) to the intrinsic coordinates (ξ_1, ξ_2) .	B-6
D.1	Continuous floating slab track (FST).	D-2
D.2	Illustration of the shifting principle [14].	D-3
D.3	(a) Components of the PiP model, and (b) the displacement and stress vectors.	D-4
D.4	The methodology of the modified PiP model.	D-7
D.5	The equivalent internal source is represented by M line loads $\tilde{\mathbf{F}}_j$ along a virtual cylinder with radius r_i .	D-8

List of Tables

2.1	Soil and pile parameters used in the illustration of the single pile BE model. Several elastic constants are given to characterize the soil and pile ($E, \nu, \mu, \lambda, c_s, c_p$), but only two of them are independent of each other.	14
3.1	Maximum relative differences between Euler-Bernoulli and Timoshenko beam theory for the case of Figure 3.2.	21
4.1	Soil and pile parameters used in the validation of the PiP model for piles.	34
4.2	Parameters of the four BE pile model configurations used in the validation of the PiP model for piles, in case of an infinite pile in a full-space.	35
4.3	Parameters of the three BE pile model configurations used in the validation of the PiP model for piles, in case of a finite pile in a half-space.	37
5.1	Soil and pile parameters used in the validation of the multiple pile model.	42
5.2	Parameters of the three BE pile model configurations used in the validation of the multiple pile model.	42
7.1	Soil, tunnel and pile parameters used to calculate the response of piled foundations to underground railway induced vibrations.	61
7.2	Parameters of the two different pile designs.	64
D.1	Differences in definitions between Tadeu and PiP.	D-10
D.2	(Anti)symmetry of the displacements $u_j(x, y)$ and stresses $\sigma_{ij}(x, y)$	D-13

List of Symbols

The following list provides an overview of symbols used throughout the text. The physical meaning of the symbols is explained in the text. Vectors, matrices and tensors are denoted by bold characters.

The general symbols, conventions and abbreviations are collected in the first two sections. The remaining symbols are categorized in sections referring to the chapters where they are first introduced.

General symbols and conventions

(x_1, x_2, x_3)	Cartesian coordinates
(r, θ, x)	cylindrical coordinates
$\partial^n / \partial \diamond^n$	n^{th} order partial derivative with respect to the variable \diamond
$\dot{\diamond}$	first order time derivative of the variable \diamond
$\ddot{\diamond}$	second order time derivative of the variable \diamond
$\Re(\diamond)$	real part of the variable \diamond
$\Im(\diamond)$	imaginary part of the variable \diamond
\diamond^*	complex conjugate of the variable \diamond
\diamond^{-1}	inverse of the matrix \diamond
\diamond^T	transpose of the matrix \diamond
$\det(\diamond)$	determinant of the matrix \diamond
I	identity matrix
δ_{ij}	Kronecker Delta
$\delta(\diamond)$	Dirac Delta function
i	imaginary unit $\sqrt{-1}$
t	time
f	frequency
ω	circular frequency

Acronyms

BE	Boundary Element
EDT	ElastoDynamicsToolbox
FE	Finite Element
FRF	Frequency Response Function
PF	Power Flow
PFIG	Power Flow Insertion Gain
PiP	Pipe-in-Pipe
PSPI	Pile-Soil-Pile Interactions

The single pile BE model

A_p	pile cross-sectional area
b_p	width of soil-pile interface elements
c_p	pressure wave velocity
c_s	shear wave velocity
c_R	Rayleigh wave velocity
d_p	pile diameter
E	Young's modulus
\mathbf{f}_p	pile force vector
\mathbf{f}_{ph}	pile-head force vector
h_p	height of soil-pile interface elements
\mathbf{H}_p	pile frequency response function matrix
\mathbf{H}_s	soil frequency response function matrix
I_p	pile second moment of inertia
L_p	pile length
M	bending moment
N_{fs}	number of free surface elements
N_p	number of pile nodes
N_{sp}	number of soil-pile interface elements
\mathbf{p}_{fs}	free surface traction vector
\mathbf{p}_{sp}	soil-pile interface traction vector
\mathbf{Q}_1	transformation matrix coupling the pile and soil
T	shear force
\mathbf{u}_{fs}	free surface displacement vector
\mathbf{u}_p	pile displacement vector
\mathbf{u}_{ph}	pile-head displacement vector
\mathbf{u}_{sp}	soil-pile interface displacement vector
β_\diamond	hysteretic material damping ratio of the elastic modulus \diamond

λ	first Lamé constant
μ	second Lamé constant (shear modulus)
ν	Poisson's ratio
ρ	density

Extensions of the single pile BE model

a_0	dimensionless frequency
c_B	bending wave velocity
c_L	longitudinal wave velocity
F_{ij}	flexibility coefficient
\mathbf{H}_b	building frequency response matrix
\mathbf{H}_c	semi-infinite column frequency response matrix
k	shear correction factor
\mathbf{k}	isolation bearing frequency response matrix
\overline{P}	total mean power flow
R	pile-load distance
W_b	bending moment driving point impedance
W'_b	coupling term between shear and bending
Z_b	shear force driving point impedance
Z_{long}	longitudinal driving point impedance
γ	shear deformation angle
κ_{x_2}	bending curvature

The multiple pile BE model

s	pile separation distance
α_{ij}	dynamic interaction factor

The response of piled foundations to underground railway induced loadings

$\tilde{\mathbf{G}}^{\text{half}}$	two-and-a-half-dimensional half-space Green's functions for displacements
$\tilde{\mathbf{G}}_{\sigma}^{\text{half}}$	two-and-a-half-dimensional half-space Green's functions for stresses
\mathbf{p}^{inc}	incident traction field
\mathbf{u}^{inc}	incident displacement field
ε_{ij}	small strain tensor
ε_{vol}	volumetric strain
σ_{ij}	Cauchy stress tensor

Chapter 1

Introduction

1.1 Ground-borne vibrations

Vibrations and re-radiated noise in buildings induced by railway traffic are a major environmental concern. Vibrations are generated at the wheel-rail interface due to wheel and rail unevenness. The vehicle-track interaction results in dynamic axle loads which are transferred by the track to the soil. The vibrations propagate as elastic waves in the surrounding soil and excite nearby buildings through their foundations (Figure 1.1).

These vibrations are an important source of annoyance in the built environment. Even at small amplitudes, they can cause disturbance of sensitive equipment [17]. Furthermore, they cause discomfort to inhabitants. In a frequency range from 1 to 80 Hz, the vibrations manifest themselves as structural vibrations, while a disturbing rumbling noise re-radiated from floors and walls may be perceived when bending resonances are excited, mainly in the frequency range from 16 to 250 Hz. Finally, there is some evidence that they may give rise to structural damage in historical buildings [20].

During the last decades, a lot of research has been performed to search for efficient and cost-effective vibration countermeasures. Generally spoken, there are three categories of methods to decrease ground-borne vibrations in buildings.

It is obvious that tackling the problem at the source is preferred, as it has an effect on several buildings. Some of these countermeasures are low-stiffness train suspensions, ballast mats, soft railpads and floating slabtracks (FST). FST is often used for underground railways, and involves the incorporation of rubber bearings or steel springs between the rail-supporting concrete slab and the tunnel bed. FST is generally regarded as one of the most effective source-countermeasures; however, recent research [14, 21, 46] suggests that the performance of FST is not as impressive as initially assumed.

A second isolation method consists of the modification of the transmission path. Several options are possible, e.g. open trenches or a row of piles. The effectiveness of these barriers is largely dependent on their dimensions relative to the wavelength of the vibration. Furthermore, these kind of solutions are often difficult to implement in practice.

Finally, measures taken at the building enclose the use of base isolation. Steel springs or rubber bearings are placed between the building and its foundation to isolate the building from the motion of the ground. The efficiency of this method has been investigated thoroughly by Talbot [46].

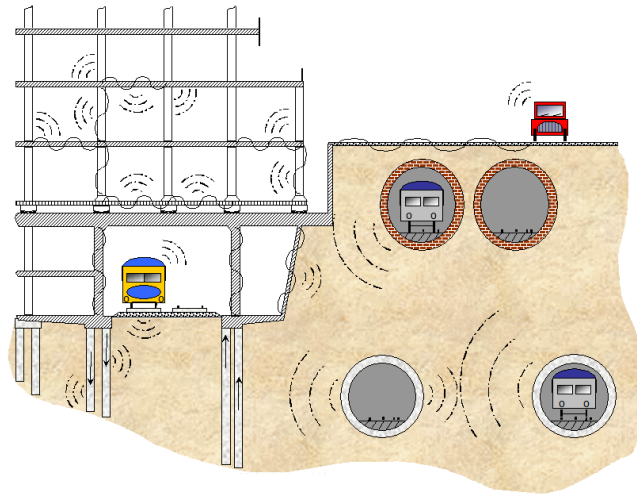


Figure 1.1: Vibrations from multiple sources propagate through and along the surface of the ground, interacting with buried objects, before being perceived in the building as vibration or re-radiated noise [46].

1.2 Modelling the source and receiver

For each of the components of the ground-borne vibration problem, several ways of modelling have been explored. Models may be formulated in the time or frequency domain. Modelling in the frequency domain is the most appropriate, as the problem may be treated as linear due to the low strain amplitudes and the fact that the response is of sufficient duration.

The finite element (FE) method is one of the most widely used numerical techniques in structural analysis. Two-dimensional models are preferred to restrict computation times, but suffer from some important disadvantages. As these models assume the system to be invariant in the anti-plane direction, the wave propagation is not modelled correctly (e.g. spherical wavefronts are modelled as cylindrical, thus underestimating the radiation damping in the soil). Furthermore, simplifications have to be made to model the three-dimensional moving train load. Fully three-dimensional models are rare, as they require considerable computing power to achieve reasonable results, especially at higher frequencies. Although the FE method is widely used, it suffers from a fundamental problem when modelling semi-infinite domains such as the ground. The element mesh should extend towards infinity, but has to be curtailed at a finite distance. As a consequence, the results are distorted due to fallacious wave reflections at the artificial boundary. Several techniques have been proposed to circumvent these difficulties, e.g. the use of infinite elements [5], or the incorporation of artificially high material damping [35].

In contrast to the FE method, the boundary element (BE) method is ideally suited to model problems with unbounded domains. The governing equations may be represented by a system of boundary integral equations, and therefore, only the boundary has to be discretized. The radiation of waves to infinity is inherently accounted for. The BE method is nowadays considered as one of the most flexible and rigorous methods for analysing the dynamic behaviour of piles and pile groups.

Within the frame of the EC Growth 2000 project CONVURT, two complementary numerical models have been developed for the prediction of vibrations due to underground railway traffic. The first source model has been developed jointly by the Division of Structural Mechanics of K.U.Leuven and Ecole Centrale Paris [8, 12]. A FE formulation is used for the tunnel and a BE model for the soil to account for the dynamic soil-structure interaction. It is assumed that the geometry of the tunnel and the track is periodic, e.g. due to the fact that the tunnel has been built up from similar segments. This allows for a Floquet transformation of the coordinate in the longitudinal direction of the track and the tunnel, and leads to a solution of the original 3D problem based on a model for a unit cell of the periodic tunnel. The second source model is the Pipe-in-Pipe (PiP) model and has been developed at Cambridge University [14, 15]. This model considers in its basic formulation a circular tunnel embedded in a homogeneous full-space. Both tunnel and soil are modelled using elastic continuum equations. A very efficient solution of the governing equations of motion is obtained by means of integral transformations. The model has been extended recently to account for a rigid bedrock, the layered character of the soil and the free surface [23]. The PiP model is computationally very efficient and has been validated extensively by means of the coupled FE-BE model. Therefore, it can be used as an engineering tool.

At the receiver side, the dynamic response of the foundation and building is computed using similar techniques as in the seismic analysis of structures. Novak [37] developed an analytical model for the longitudinal and transverse behaviour of a single pile, but it is incapable of modelling the interaction between several piles. The model developed by Kaynia [24] uses the BE method and is capable of modelling the interaction between neighbouring piles, known as pile-soil-pile interactions (PSPI). Talbot [46] has presented a generic model of an infinite base-isolated building, using periodic structure theory. It is a linear model which couples a three-dimensional BE model of the piled foundation with a two-dimensional portal frame model of the building. He also introduced the concept of power flow insertion gain (PFIG) as a single useful measure of isolation performance. Kuo [27] has taken advantage of the principles of the PiP model for underground railways to obtain a very efficient model for piled foundations, the so-called Pipe-in-model for piles.

Whilst many well-established models exist for the dynamic behaviour of piled foundations, either due to an incident seismic wavefield or an inertial loading, there is no evidence in the literature for a comprehensive model of piled foundations subject to a wavefield generated by an underground railway. It is thought that the lack of such a model is due to the complexity of modelling such a system, particularly the large number of elements required (and subsequent increase in computation time) when using FE or BE models [28].

1.3 Objectives of the research

As cities become more densely populated, less interesting areas near (underground) railways will be used for building construction. In addition to this, modern construction techniques consist of continuous light-weight structures with inherently low damping. Grootenhuis [19] shows that a typical train spends more than enough time passing a building to establish a full state of resonance. As a

result, modern buildings tend to be more susceptible to vibration within the frequency range of interest. Therefore, the social relevance of ground-borne vibration will further increase [9].

This dissertation has several aims. Firstly, the PiP model for piles developed by Kuo [27] needs to be validated before it can be used as an engineering tool. This validation will be carried in case of simple inertial loadings as well as for underground railway induced loadings. Furthermore, it is the purpose to contribute towards a better understanding of the dynamic behaviour of piled foundations. One of the aspects to be investigated is the shadow effect, which denotes the influence of the presence of a pile on the response of another pile in function of their relative position. Besides this, the response of piled foundations to underground railway induced loadings will be examined in detail. More specifically, aspects such as the efficiency of base isolation, the significance of pile-soil-pile interactions and the importance of horizontal and rotational motion will be investigated.

In order to achieve these aims, a model for piled foundations which accounts for the fundamental behaviour of each pile and the interaction between neighbouring piles is developed. It is a BE model, based on the work of Talbot [46], implemented in MATLAB.

1.4 Outline of the dissertation

Chapter 2 gives a detailed summary of the single pile BE model developed by Talbot [46]. It forms the basis of this dissertation.

Chapter 3 presents a variety of extensions made to the initial single pile BE model. Special attention is given to the incorporation of power flow calculations in the model.

Chapter 4 explains how the extended single pile BE model is used to validate the PiP model for piles. Validation calculations are carried out for an infinite pile in a full-space and a finite pile in a half-space.

Chapter 5 introduces a multiple pile BE model that accounts for PSPI. The results are validated in terms of dynamic interaction factors.

Chapter 6 is completely dedicated to the shadow effect. The multiple pile BE model introduced in chapter 5 is used to assess the influence of the presence of a pile on the response of another one in function of their relative position.

Chapter 7 combines the PiP model for vibrations from underground railways with the multiple pile BE model. It is assumed that the incident wavefield is not affected by the presence of the receiver, so that the coupling between source and receiver can be disregarded. This results in a two-step approach (subdomain formulation). A case study is presented to illustrate the application of the model.

Chapter 8 summarizes the conclusions of this dissertation and gives recommendations for further research.

Chapter 2

The single pile BE model

This chapter describes the single pile BE model which has been developed by Talbot [46]. The purpose is to give a clear overview of the model, as all further work in this dissertation is based on it.

The model represents a single pile embedded in a homogeneous, isotropic linear elastic half-space. This representation accounts for the essential dynamic behaviour of the soil, i.e. the three fundamental wave types (dilatational, shear and Rayleigh waves) and radiation and material damping. A uniform half-space is an idealization, as the soil density often increases with depth and different soil strata may be present. However, these complications are considered beyond the scope of this dissertation. Boundary elements with constant shape functions are used to model the soil, as summarized in Appendix B. This BE model is coupled to a pile model to obtain a three-dimensional foundation model. It is assumed that the pile is perfectly bonded to the soil, an assumption that can be justified by the small amplitudes of the vibrations under concern. The pile itself is modelled as an Euler-Bernoulli beam, and local deformation of the pile's cross-section is neglected. The model is based on a square approximation of the circular pile circumference.

The model is formulated in the frequency domain, as steady-state time-harmonic loading is considered, and complex notation is used for all field variables. For instance, the displacement vector $\mathbf{u}(\mathbf{x}, t)$ is written as follows:

$$\mathbf{u}(\mathbf{x}, t) = \Re\left(\mathbf{u}(\mathbf{x}, \omega)e^{i\omega t}\right) \quad (2.1)$$

However, for clarity, the exponential notation will be omitted throughout this dissertation, and \mathbf{u} implies a vector of complex amplitude.

Material damping is accounted for by means of the correspondence principle of linear visco-elasticity, which states that visco-elastic materials can be modelled in the frequency domain as equivalent elastic materials with complex elastic moduli. For example, the shear modulus μ becomes $\mu(1 + 2\beta_\mu i)$. More details can be found in Appendix B.1.

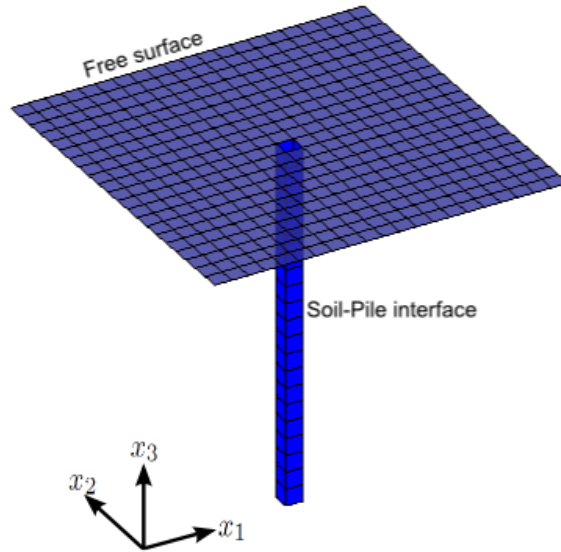


Figure 2.1: The boundary element mesh of the single pile model developed by Talbot [46], here for the case of $N_1 = N_2 = 21$, $N_{sp} = 85$.

2.1 The soil and the soil-pile interface

The BE model consists of two parts: the soil-pile interface and the free surface. Full-space Green's functions are used as the fundamental solution in the BE formulation, and therefore the free surface has to be discretized (Appendix B). An important aspect of the pile-soil interface is the number of elements around the circumference. The more elements are used, the more accurately the circular cross-section of the pile is approximated, but the longer the computation time. It also obliges non-rectangular elements on the free surface, and the numerical integration of such elements is more involved (Appendix B).

In [46], the significance of the number of circumferential boundary elements is investigated. This is carried out by means of a two-dimensional BE model under plain strain conditions to model an infinitely long cylindrical cavity in an infinite solid. The number of elements is varied from $N = 4$ up till $N = 32$, and the results are compared with the analytical solution in terms of the transverse and longitudinal dynamic stiffness (K_t and K_l). With $N = 32$, the numerical results coincide with the analytical solution, but the computation time for such a model becomes limiting. With only four elements being used, there is a significant reduction of the accuracy of the model, but the advantages are a shorter processing time and the use of only rectangular elements. Talbot [46] considered the errors caused to be acceptable and proceeded with a pile model based on four elements around the pile circumference. The errors caused by this simplification mainly manifest themselves as an underprediction of the imaginary stiffness component, which has the physical meaning of an underprediction of the level of radiation damping. Another remark is that the behaviour is almost completely dominated by radiation damping, such that the precise value of the material loss factor becomes unimportant. The errors in the BE results increase with frequency, as the wavelengths

approach the diameter of the cavity. In section 3.4, the initial model will be extended to a pile with an octagonal cross-section.

It is worth noting that during the investigation which has been described above, using a two-dimensional BE model for an infinitely long cavity, the model suffered from the presence of fictitious natural frequencies (Appendix B). These are natural frequencies associated with the equivalent internal problem (i.e. an infinitely long cylindrical bar), with the boundary Γ subject to imposed displacements. These resonances have no physical meaning for the cavity. However, in the three-dimensional pile model, full-space Green's functions are used in conjunction with a free surface discretization, and hence an internal boundary value problem is being solved. As a result, fictitious frequencies do not arise in the three-dimensional pile model [4].

Having selected four boundary elements to model the pile circumference, the three-dimensional pile model can be reconsidered. The BE model representing the soil consists of N rectangular elements, as illustrated in Figure 2.1. Constant shape functions are used, which means that displacements and tractions are assumed to be uniform over each element and equal to the value of the central node. The free surface is represented by a rectangular mesh of $N_{fs} = N_1 \times N_2 - 1$ elements, while the soil-pile interface consists of N_{sp} elements. The number of elements N_1 and N_2 is increased until convergence of the results is observed over the frequency range of interest, for each possible load case. The free surface elements have dimensions $b_1 \times b_2$, and the soil-pile interface elements $b_p \times h_p$.

The relationship between the displacements and tractions of the N nodes is given by Eq. (B.23) of Appendix B, and is repeated here:

$$\mathbf{H}\mathbf{u} = \mathbf{G}\mathbf{p} \quad (2.2)$$

\mathbf{H} and \mathbf{G} are $3N \times 3N$ matrices describing the dynamic behaviour of the soil in function of the soil parameters ρ , μ , λ , β_μ , β_λ and the frequency of interest f . \mathbf{u} is a $3N \times 1$ vector, containing the three displacement components of each node:

$$\mathbf{u} = \left\{ u_1^1 \quad u_2^1 \quad u_3^1 | \cdots | u_1^j \quad u_2^j \quad u_3^j | \cdots | u_1^N \quad u_2^N \quad u_3^N \right\}^T \quad (2.3)$$

The corresponding traction vector \mathbf{p} is composed in a similar way:

$$\mathbf{p} = \left\{ p_1^1 \quad p_2^1 \quad p_3^1 | \cdots | p_1^j \quad p_2^j \quad p_3^j | \cdots | p_1^N \quad p_2^N \quad p_3^N \right\}^T \quad (2.4)$$

Eq. (2.2) can be rearranged and partitioned as follows:

$$\begin{aligned} \mathbf{u} &= [\mathbf{H}]^{-1} \mathbf{G}\mathbf{p} \\ &= \mathbf{H}_s \mathbf{p} \end{aligned} \quad (2.5)$$

If written in full, this gives:

$$\begin{Bmatrix} \mathbf{u}_{\text{fs}} \\ \mathbf{u}_{\text{sp}} \end{Bmatrix} = \begin{bmatrix} \mathbf{H}_s^{11} & \mathbf{H}_s^{12} \\ \mathbf{H}_s^{21} & \mathbf{H}_s^{22} \end{bmatrix} \begin{Bmatrix} \mathbf{p}_{\text{fs}} \\ \mathbf{p}_{\text{sp}} \end{Bmatrix} \quad (2.6)$$

The subscripts fs and sp indicate free surface respectively soil-pile interface. The matrix \mathbf{H}_s is the soil's frequency response function (FRF) matrix, and relates the displacements and tractions of the different nodes.

2.2 The pile model

The pile model should account for the essential dynamic behaviour, i.e. the longitudinal and transverse motion of the pile due to forces and moments applied to the pile-head. It is modelled as an Euler-Bernoulli beam of length L_p , cross-sectional area A_p and second moment of inertia I_p . It is emphasized that I_p denotes the second moment of inertia of the pile, and not its polar moment. The local deformation of the pile's cross-section is neglected. ρ_p and E_p stand for the pile's density respectively Young's modulus.

The pile is defined by N_p equally spaced nodes, and two extra nodes are added at the head and the tip of the pile (Figure 2.2). At each node, three force components can be applied, while two extra bending moments can be applied at the pile-head (torsion is excluded). In order to proceed, the pile's frequency response function matrix \mathbf{H}_p has to be obtained. This matrix should embody the response of the pile due to a unit force applied at each node along the pile.

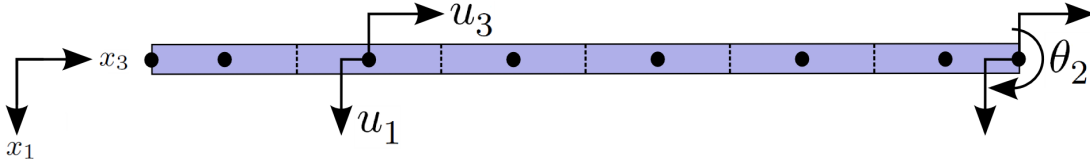


Figure 2.2: Pile model (drawn horizontally), for the case of $N_p = 6$. The dots represent the nodes, the dashed lines delimit the boundary elements of the soil-pile interface. Only the (x_1, x_3) -plane is shown.

2.2.1 Longitudinal behaviour

A unit harmonic force with angular frequency ω is applied in the longitudinal x_3 -direction at node j . In order to find the response u_3 of the pile, either side of node j has to be considered. The general solution of u_3 is given by Newland [36]:

$$u_3(x_3, \omega) = u_3^{\text{I}} = A^{\text{I}} \cos \alpha x_3 + B^{\text{I}} \sin \alpha x_3 \quad \text{for } 0 \leq x_3 \leq x_3^j \quad (2.7a)$$

$$u_3(x_3, \omega) = u_3^{\text{II}} = A^{\text{II}} \cos \alpha x_3 + B^{\text{II}} \sin \alpha x_3 \quad \text{for } x_3^j \leq x_3 \leq L_p \quad (2.7b)$$

with $\alpha = \omega \sqrt{\frac{\rho_p}{E_p}}$ and A^I, B^I, A^{II}, B^{II} coefficients to be specified.

The superscripts I and II indicate the sections above and beneath the node considered. However, u_3 needs to be continuous at node j , which implies following constraint:

$$u_3^I(x_3^j) = u_3^{II}(x_3^j) \quad (2.8)$$

Furthermore, the boundary conditions should be fulfilled. Since the pile is otherwise unloaded, the ends of the pile must be traction-free:

$$\left(\frac{\partial u_3^I}{\partial x_3} \right)_{x_3=0} = \left(\frac{\partial u_3^{II}}{\partial x_3} \right)_{x_3=L_p} = 0 \quad (2.9)$$

Finally, force equilibrium should be satisfied at node j :

$$E_p A_p \left(\frac{\partial u_3^I}{\partial x_3} \right)_{x_3=x_3^j} - E_p A_p \left(\frac{\partial u_3^{II}}{\partial x_3} \right)_{x_3=x_3^j} = 1 \quad (2.10)$$

Introducing Eqs. (2.8), (2.9) and (2.10) into the general solution Eq. (2.7) provides expressions for the coefficients A^I, B^I, A^{II} and B^{II} :

$$A^I = \frac{-\cos \alpha x_3^j - \sin \alpha x_3^j \tan \alpha L_p}{E_p A_p \alpha \tan \alpha L_p} \quad (2.11)$$

$$B^I = 0 \quad (2.12)$$

$$A^{II} = \frac{-\cos \alpha x_3^j}{E_p A_p \alpha \tan \alpha L_p} \quad (2.13)$$

$$B^{II} = \frac{-\cos \alpha x_3^j}{E_p A_p \alpha} \quad (2.14)$$

Combining Eq. (2.7) and Eqs. (2.11)–(2.14) permits to calculate the longitudinal response of each node due to a unit longitudinal force applied at x_3^j .

2.2.2 Transverse behaviour

As mentioned before, the pile is assumed to behave as an Euler-Bernoulli beam for transverse loading. When a unit harmonic force with angular frequency ω is applied in the transverse x_1 -direction at node j , the general solution for u_1 reads as follows:

$$u_1(x_3, \omega) = u_1^I = A^I e^{\beta x_3} + B^I e^{i\beta x_3} + C^I e^{-\beta x_3} + D^I e^{-i\beta x_3} \quad \text{for } 0 \leq x_3 \leq x_3^j \quad (2.15a)$$

$$u_1(x_3, \omega) = u_1^{II} = A^{II} e^{\beta x_3} + B^{II} e^{i\beta x_3} + C^{II} e^{-\beta x_3} + D^{II} e^{-i\beta x_3} \quad \text{for } x_3^j \leq x_3 \leq L_p \quad (2.15b)$$

where $\beta = \left(\frac{\rho_p A_p \omega^2}{E_p I_p}\right)^{1/4}$ and $A^I, B^I, C^I, D^I, A^{II}, B^{II}, C^{II}, D^{II}$ are coefficients to be specified.

Compatibility of displacement and rotation are required at node j :

$$u_1^I(x_3^j) = u_1^{II}(x_3^j) \quad (2.16a)$$

$$\left(\frac{\partial u_1^I}{\partial x_3}\right)_{x_3=x_3^j} = \left(\frac{\partial u_1^{II}}{\partial x_3}\right)_{x_3=x_3^j} \quad (2.16b)$$

Since the pile is otherwise unloaded, there should be no shear forces or bending moments at the ends of the pile:

$$T_{x_3=0} = 0 \Rightarrow -E_p I_p \left(\frac{\partial^3 u_1^I}{\partial x_3^3}\right)_{x_3=0} = 0 \quad (2.17a)$$

$$M_{x_3=0} = 0 \Rightarrow E_p I_p \left(\frac{\partial^2 u_1^I}{\partial x_3^2}\right)_{x_3=0} = 0 \quad (2.17b)$$

and

$$T_{x_3=L_p} = 0 \Rightarrow -E_p I_p \left(\frac{\partial^3 u_1^{II}}{\partial x_3^3}\right)_{x_3=L_p} = 0 \quad (2.18a)$$

$$M_{x_3=L_p} = 0 \Rightarrow E_p I_p \left(\frac{\partial^2 u_1^{II}}{\partial x_3^2}\right)_{x_3=L_p} = 0 \quad (2.18b)$$

Furthermore, both force and moment equilibrium should be satisfied at node j :

$$-E_p I_p \left(\frac{\partial^3 u_1^I}{\partial x_3^3}\right)_{x_3=x_3^j} + E_p I_p \left(\frac{\partial^3 u_1^{II}}{\partial x_3^3}\right)_{x_3=x_3^j} = 1 \quad (2.19a)$$

$$E_p I_p \left(\frac{\partial^2 u_1^I}{\partial x_3^2}\right)_{x_3=x_3^j} - E_p I_p \left(\frac{\partial^2 u_1^{II}}{\partial x_3^2}\right)_{x_3=x_3^j} = 0 \quad (2.19b)$$

Incorporating Eqs. (2.16)–(2.19) into the general solution Eq. (2.15) provides a system of eight equations from which the coefficients $A^I, B^I, C^I, D^I, A^{II}, B^{II}, C^{II}$ and D^{II} are obtained:

$$\begin{bmatrix} e^{\beta x_3^j} & e^{i\beta x_3^j} & e^{-\beta x_3^j} & e^{-i\beta x_3^j} & -e^{\beta x_3^j} & -e^{i\beta x_3^j} & -e^{-\beta x_3^j} & -e^{-i\beta x_3^j} \\ e^{\beta x_3^j} & ie^{i\beta x_3^j} & -e^{-\beta x_3^j} & -ie^{-i\beta x_3^j} & -e^{\beta x_3^j} & -ie^{i\beta x_3^j} & e^{-\beta x_3^j} & ie^{-i\beta x_3^j} \\ 1 & -1 & 1 & -1 & 0 & 0 & 0 & 0 \\ 1 & -i & -1 & i & 0 & 0 & 0 & 0 \\ 0 & 0 & 0 & 0 & e^{\beta L_p} & -e^{i\beta L_p} & e^{-\beta L_p} & -e^{-i\beta L_p} \\ 0 & 0 & 0 & 0 & e^{\beta L_p} & -ie^{i\beta L_p} & -e^{-\beta L_p} & ie^{-i\beta L_p} \\ e^{\beta x_3^j} & -e^{i\beta x_3^j} & e^{-\beta x_3^j} & -e^{-i\beta x_3^j} & -e^{\beta x_3^j} & e^{i\beta x_3^j} & -e^{-\beta x_3^j} & e^{-i\beta x_3^j} \\ e^{\beta x_3^j} & -ie^{i\beta x_3^j} & -e^{-\beta x_3^j} & ie^{-i\beta x_3^j} & -e^{\beta x_3^j} & ie^{i\beta x_3^j} & e^{-\beta x_3^j} & -ie^{-i\beta x_3^j} \end{bmatrix} \begin{bmatrix} A^I \\ B^I \\ C^I \\ D^I \\ A^{II} \\ B^{II} \\ C^{II} \\ D^{II} \end{bmatrix} = \begin{bmatrix} 0 \\ 0 \\ 0 \\ 0 \\ 0 \\ 0 \\ 0 \\ 1/E_p I_p \beta^3 \end{bmatrix} \quad (2.20)$$

Combining Eq. (2.15) and Eq. (2.20) permits to calculate the transverse response of each node due to a unit transverse force applied at x_3^j .

In order to complete the pile model, the response of the pile due to a unit moment applied at the pile-head has to be determined. The transverse behaviour is still described by Eq. (2.15), but only one section of the pile has to be considered (since the moment is applied at the pile-head). The four necessary coefficients A^I , B^I , C^I and D^I can be obtained by incorporating the appropriate boundary conditions. The pile-tip should be free of shear forces and bending moments:

$$T_{x_3=0} = 0 \Rightarrow -E_p I_p \left(\frac{\partial^3 u_1^I}{\partial x_3^3} \right)_{x_3=0} = 0 \quad (2.21a)$$

$$M_{x_3=0} = 0 \Rightarrow E_p I_p \left(\frac{\partial^2 u_1^I}{\partial x_3^2} \right)_{x_3=0} = 0 \quad (2.21b)$$

Force and moment equilibrium at the pile-head imply:

$$T_{x_3=L_p} = 0 \Rightarrow -E_p I_p \left(\frac{\partial^3 u_1^I}{\partial x_3^3} \right)_{x_3=L_p} = 0 \quad (2.22a)$$

$$M_{x_3=L_p} = 1 \Rightarrow E_p I_p \left(\frac{\partial^2 u_1^I}{\partial x_3^2} \right)_{x_3=L_p} = 1 \quad (2.22b)$$

Eqs. (2.21) and (2.22) provide a system of four equations from which the four necessary coefficients can be obtained:

$$\begin{bmatrix} 1 & -1 & 1 & -1 \\ e^{\beta L_p} & -e^{i\beta L_p} & e^{-\beta L_p} & -e^{-i\beta L_p} \\ 1 & -i & -1 & i \\ e^{\beta L_p} & -ie^{i\beta L_p} & -e^{-\beta L_p} & ie^{-i\beta L_p} \end{bmatrix} \begin{Bmatrix} A^I \\ B^I \\ C^I \\ D^I \end{Bmatrix} = \begin{Bmatrix} 0 \\ 1/E_p I_p \beta^2 \\ 0 \\ 0 \end{Bmatrix} \quad (2.23)$$

2.2.3 The assembled pile model

Based on the expressions given in paragraphs 2.2.1 and 2.2.2, the frequency response function (FRF) matrix \mathbf{H}_p of the pile can be assembled. In the original model developed by Talbot, only motion in the (x_1, x_3) -plane was considered (because the pile model was coupled to a planar building model). In this dissertation, this is extended to a fully three-dimensional model, with the exception of pile torsion. Thus, the pile-head has five degrees of freedom, while all the other nodes have three:

$$\mathbf{u}_{ph} = \left\{ u_1^{ph} \quad u_2^{ph} \quad u_3^{ph} \quad \theta_1^{ph} \quad \theta_2^{ph} \right\}^T \quad (2.24)$$

$$\mathbf{u}_p = \left\{ u_1^{p1} \quad u_2^{p1} \quad u_3^{p1} \mid \dots \mid u_1^{pj} \quad u_2^{pj} \quad u_3^{pj} \mid \dots \mid u_1^{N_p+1} \quad u_2^{N_p+1} \quad u_3^{N_p+1} \right\}^T \quad (2.25)$$

The corresponding force vectors \mathbf{f}_{ph} and \mathbf{f}_{p} take a similar form. The subscripts ph and p indicate pile-head respectively pile. The matrix \mathbf{H}_{p} relates the displacements and forces and is partitioned as follows:

$$\begin{Bmatrix} \mathbf{u}_{\text{ph}} \\ \mathbf{u}_{\text{p}} \end{Bmatrix} = \begin{bmatrix} \mathbf{H}_{\text{p}}^{11} & \mathbf{H}_{\text{p}}^{12} \\ \mathbf{H}_{\text{p}}^{21} & \mathbf{H}_{\text{p}}^{22} \end{bmatrix} \begin{Bmatrix} \mathbf{f}_{\text{ph}} \\ \mathbf{f}_{\text{p}} \end{Bmatrix} \quad (2.26)$$

It can be noted that the methodology followed for the pile comes down to the use of classical finite beam elements. As a consequence, the FRF matrix \mathbf{H}_{p} which is obtained in Eq. (2.26) is the inverse of the dynamic FE stiffness matrix of the pile.

2.3 Coupling the pile and soil

As mentioned before, it is assumed that the pile is perfectly bonded to the soil, an assumption which can be justified by the small amplitudes of the vibrations under concern. Furthermore, the Poisson effect of the pile is neglected. The soil-pile interface is modelled by N_{sp} constant boundary elements, each having a central node, while the pile is represented by its centroidal axis along which lie $N_{\text{p}} + 2$ nodes. All nodes on the pile are coupled to those of the soil-pile interface, with exception of the pile-head, as illustrated in Figure 2.3.

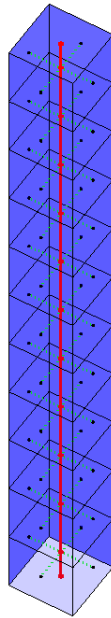


Figure 2.3: Illustration of the coupling between the soil and pile models. All pile nodes are coupled to those of the surrounding boundary elements (represented by dashed lines), except the pile-head node. The free surface discretization is not shown.

The displacement compatibility implies the following relationships:

$$\mathbf{u}_{\text{sp}}^{4j-3} = \mathbf{u}_{\text{sp}}^{4j-2} = \mathbf{u}_{\text{sp}}^{4j-1} = \mathbf{u}_{\text{sp}}^{4j} = \mathbf{u}_{\text{p}}^j \quad \text{for } j = 1 \dots N_{\text{p}} \quad (2.27\text{a})$$

and

$$\mathbf{u}_{\text{sp}}^{4N_{\text{p}}+1} = \mathbf{u}_{\text{p}}^{N_{\text{p}}+1} \quad (2.27\text{b})$$

As presented in Eq. (2.25), \mathbf{u}_{p} contains the nodal displacements of the pile except those at the pile-head. Eq. (2.27) can be written in matrix form:

$$\mathbf{u}_{\text{sp}} = \mathbf{Q}_1 \mathbf{u}_{\text{p}} \quad (2.28)$$

where \mathbf{Q}_1 is a transformation matrix with $3(4N_{\text{p}} + 1) \times 3(N_{\text{p}} + 1)$ dimensions. The matrix \mathbf{Q}_1 is specified in Appendix C.

Besides the displacement compatibility, force equilibrium should also be satisfied at any of the pile nodes:

$$\mathbf{f}_{\text{p}}^j = -b_{\text{p}}h_{\text{p}}(\mathbf{p}_{\text{sp}}^{4j-3} + \mathbf{p}_{\text{sp}}^{4j-2} + \mathbf{p}_{\text{sp}}^{4j-1} + \mathbf{p}_{\text{sp}}^{4j}) \quad \text{for } j = 1 \dots N_{\text{p}} \quad (2.29\text{a})$$

and

$$\mathbf{f}_{\text{p}}^{N_{\text{p}}+1} = -b_{\text{p}}h_{\text{p}}\mathbf{p}_{\text{sp}}^{4N_{\text{p}}+1} \quad (2.29\text{b})$$

Again, \mathbf{f}_{p} contains the nodal forces of the pile except those at the pile-head. b_{p} and h_{p} denote the width respectively the height of the boundary elements representing the soil-pile interface (an extension compared to the original model of Talbot, where only square elements were considered). Eq. (2.29) can be written in matrix form:

$$\mathbf{f}_{\text{p}} = -b_{\text{p}}h_{\text{p}}\mathbf{Q}_1^{\text{T}}\mathbf{p}_{\text{sp}} \quad (2.30)$$

Finally, Eqs. (2.6), (2.26), (2.28) and (2.30) can be combined to obtain the response of the pile to a prescribed pile-head load \mathbf{f}_{ph} , assuming a traction-free free surface ($\mathbf{p}_{\text{fs}} = \mathbf{0}$):

$$\mathbf{u}_{\text{p}} = \left(\mathbf{I} + b_{\text{p}}h_{\text{p}}\mathbf{H}_{\text{p}}^{22}\mathbf{Q}_1^{\text{T}}\left[\mathbf{H}_{\text{s}}^{22}\right]^{-1}\mathbf{Q}_1 \right)^{-1} \mathbf{H}_{\text{p}}^{21}\mathbf{f}_{\text{ph}} \quad (2.31)$$

In Eq. (2.31), \mathbf{I} represents a $(N_{\text{p}} + 1) \times (N_{\text{p}} + 1)$ identity matrix. Once \mathbf{u}_{p} is calculated, the remaining unknowns can be found.

2.4 Validation and illustration

The single pile BE model has been validated by Talbot [46]. Firstly, the static pile-head compliance has been compared to the solution obtained by Poulos and Davis [39]. Although there was some

deviation for the vertical component, the overall agreement was satisfying. Furthermore, the dynamic results have been compared in terms of flexibility coefficients to those obtained by the models of Kuhlemeyer [25, 26] and Sen [43]. These models use two independent methods, respectively the FE and BE method. The current BE model was found to be in good agreement with the two other models.

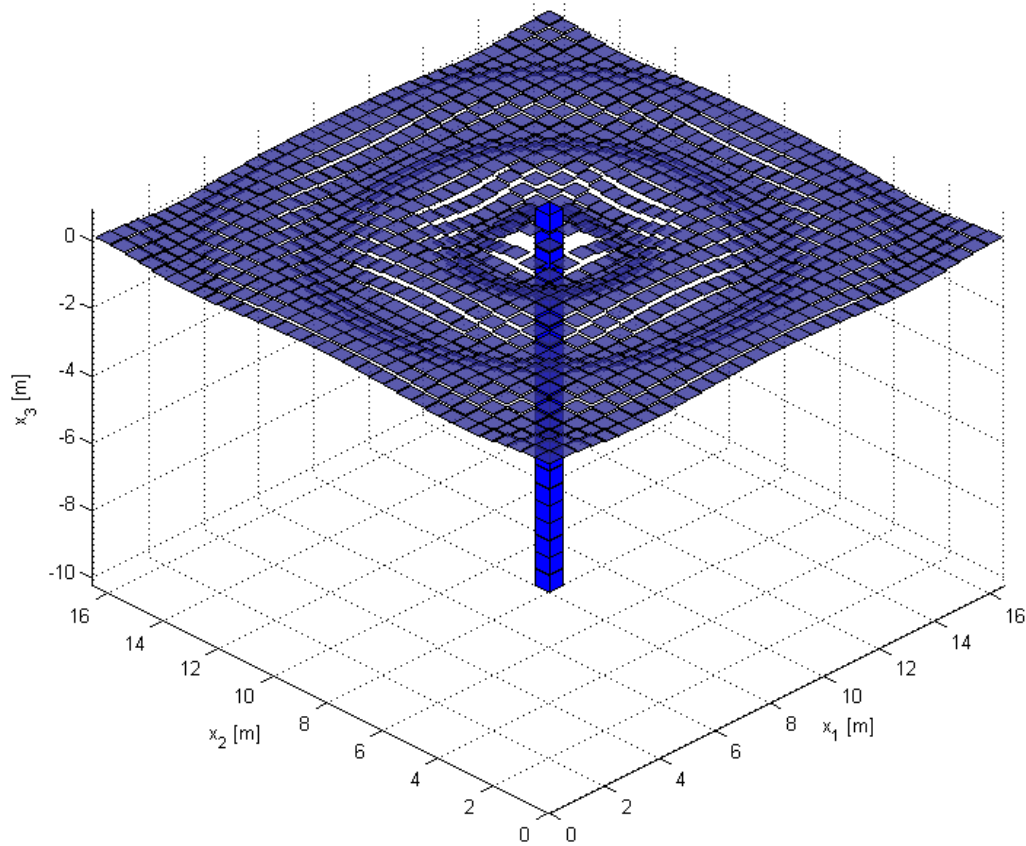
Figure 2.4 shows the response of the pile and the boundary element mesh to a harmonic unit vertical load applied at the pile-head, at 50 Hz. The BE mesh is characterized by the following parameters: $N_1 = N_2 = 33$ and $b_1 = b_2 = b_p = h_p = 0.50$ m. The latter ensures that the recommendation by Dominguez [13] that at least six constant elements per wavelength should be used, is fulfilled. The parameters of the soil and pile are summarized in Table 2.1. As expected, concentric circular wavefronts can be noticed on the free surface of the soil in Figure 2.4(a). Furthermore, based on the formula presented in [47], the expected Rayleigh wavelength equals 3.75 m, which is approximately the value predicted by the model (Figure 2.4(b)). Due to the coarseness of the mesh and the fact that the comparison should be made in the far-field, the agreement is not perfect.

Parameter	Soil	Pile
E [Pa]	252×10^6	30×10^9
ν [-]	0.40	0.25
μ [Pa]	90×10^6	12×10^9
λ [Pa]	360×10^6	12×10^9
ρ [kg/m ³]	2250	2500
β_μ [-]	0.03	0
β_λ [-]	0.03	0
c_s [m/s]	200.1	2190.9
c_p [m/s]	490.1	3794.7
L [m]	–	10.5
d [m]	–	$1/\sqrt{2}$

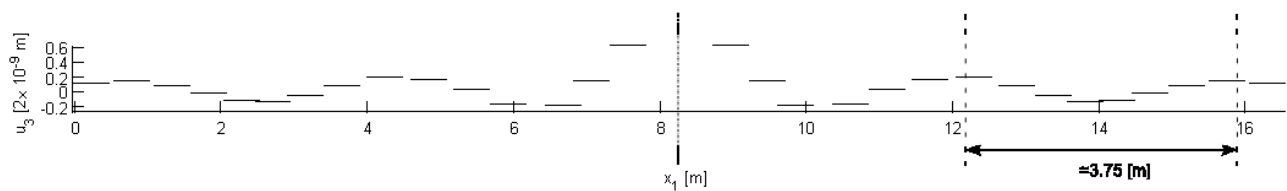
Table 2.1: Soil and pile parameters used in the illustration of the single pile BE model. Several elastic constants are given to characterize the soil and pile (E , ν , μ , λ , c_s , c_p), but only two of them are independent of each other.

2.5 Conclusion

In this chapter, the single pile BE model developed by Talbot [46] has been introduced. The model represents a single pile embedded in a homogeneous half-space. It accounts for the fundamental dynamic behaviour of a piled foundation, i.e. the horizontal, vertical and rotational motion of the pile-head due to direct pile-head loading. Despite the fact that the model does not make use of the axisymmetry of the system, it has been illustrated that it correctly predicts circular wavefronts on the free surface of the soil when the pile is loaded by a harmonic vertical load.



(a) Three-dimensional view (displacements are multiplied with a factor 2×10^9).



(b) Vertical cross-section through the free surface at the location of the pile centroid.

Figure 2.4: Displacement field predicted by the single pile BE model due to a unit vertical load applied at the pile-head, at 50 Hz. The three-dimensional view (a) clearly illustrates the concentric circular wavefronts. The vertical cross-section (b) shows that the model correctly predicts the Rayleigh wavelength of 3.75 m.

Chapter 3

Extensions of the single pile BE model

In this chapter, some extensions are made to the initial single pile model described in chapter 2.

3.1 Timoshenko beam theory

The FRF matrix \mathbf{H}_p of the pile has been assembled in section 2.2 based on the assumption that the pile behaves as an Euler-Bernoulli beam under transverse loading. The latter is an approximation, as the effects of inertial moment and shear deformation are neglected. In order to include these effects, Timoshenko beam theory is introduced into the model.

3.1.1 Equations

The lateral equilibrium equation of a Timoshenko beam is given by Eq. (3.1) [7]. Contrary to section 2.2, the subscript p is omitted in the indication of the elastic and geometrical constants associated with the pile.

$$m \frac{\partial^2 u_1}{\partial t^2} + EI \frac{\partial^4 u_1}{\partial x_3^4} - mr^2 \left(1 + \frac{E}{k\mu} \right) \frac{\partial^4 u_1}{\partial x_3^2 \partial t^2} + \frac{m^2 r^2}{k\mu A} \frac{\partial^4 u_1}{\partial t^4} = 0 \quad (3.1)$$

In Eq. (3.1), m is the mass per unit length, r the radius of gyration and k the shear coefficient, i.e. the ratio of the shear cross-section A_s and the geometrical cross-section A :

$$m = \rho A \quad (3.2)$$

$$r = \sqrt{\frac{I}{A}} \quad (3.3)$$

$$k = \frac{A_s}{A} \simeq \frac{9}{10} \quad (\text{circular cross-section}) \quad (3.4)$$

Introducing the complex notation $u_1(x, t) = \Re(u_1(x_3, \omega)e^{i\omega t})$ results in an ordinary differential equation:

$$-m\omega^2 u_1 + EI \frac{\partial^4 u_1}{\partial x_3^4} + m\omega^2 r^2 \left(1 + \frac{E}{k\mu}\right) \frac{\partial^2 u_1}{\partial x_3^2} + \frac{m^2 r^2}{k\mu A} \omega^4 = 0 \quad (3.5)$$

The general solution of Eq. (3.5) reads as follows:

$$u_1(x_3, \omega) = Ae^{\lambda_1 x_3} + Be^{\lambda_2 x_3} + Ce^{\lambda_3 x_3} + De^{\lambda_4 x_3} \quad (3.6)$$

with

$$\lambda_i = \pm \sqrt{\frac{-b \pm \sqrt{b^2 - 4ac}}{2a}} \quad (3.7)$$

$$a = EI \quad (3.8)$$

$$b = m\omega^2 r^2 \left(1 + \frac{E}{k\mu}\right) \quad (3.9)$$

$$c = -m\omega^2 + \frac{m^2 r^2}{k\mu A} \omega^4 \quad (3.10)$$

The FRF matrix \mathbf{H}_p of the pile can be obtained by following the same approach as in paragraph 2.2.2. A time harmonic unit force is applied in the transverse x_1 -direction at node j , and the response u_1 is split up in two parts, one on either side of node j :

$$u_1(x_3, \omega) = u_1^I = A^I e^{\lambda_1 x_3} + B^I e^{\lambda_2 x_3} + C^I e^{\lambda_3 x_3} + D^I e^{\lambda_4 x_3} \quad \text{for } 0 \leq x_3 \leq x_3^j \quad (3.11a)$$

$$u_1(x_3, \omega) = u_1^{II} = A^{II} e^{\lambda_1 x_3} + B^{II} e^{\lambda_2 x_3} + C^{II} e^{\lambda_3 x_3} + D^{II} e^{\lambda_4 x_3} \quad \text{for } x_3^j \leq x_3 \leq L_p \quad (3.11b)$$

The boundary conditions necessary to obtain the coefficients A^I to D^{II} remain the same as those given by Eqs. (2.16)–(2.19). They are repeated here:

$$u_1^I(x_3^j) = u_1^{II}(x_3^j) \quad \text{and} \quad \left(\frac{\partial u_1^I}{\partial x_3}\right)_{x_3=x_3^j} = \left(\frac{\partial u_1^{II}}{\partial x_3}\right)_{x_3=x_3^j} \quad (3.12)$$

$$T_{x_3=0} = 0 \quad \text{and} \quad M_{x_3=0} = 0 \quad (3.13)$$

$$T_{x_3=L_p} = 0 \quad \text{and} \quad M_{x_3=L_p} = 0 \quad (3.14)$$

$$T^I(x_3^j) - T^{II}(x_3^j) = 1 \quad \text{and} \quad M^I(x_3^j) - M^{II}(x_3^j) = 0 \quad (3.15)$$

However, the expressions for the shear force T and bending moment M are somewhat more extended. They follow from the kinematic relationships illustrated in Figure 3.1. It is assumed that the normals to the axis of the beam remain straight after deformation, and that there is no change in beam thickness. However, the normals are not required to remain perpendicular to the axis after deformation.

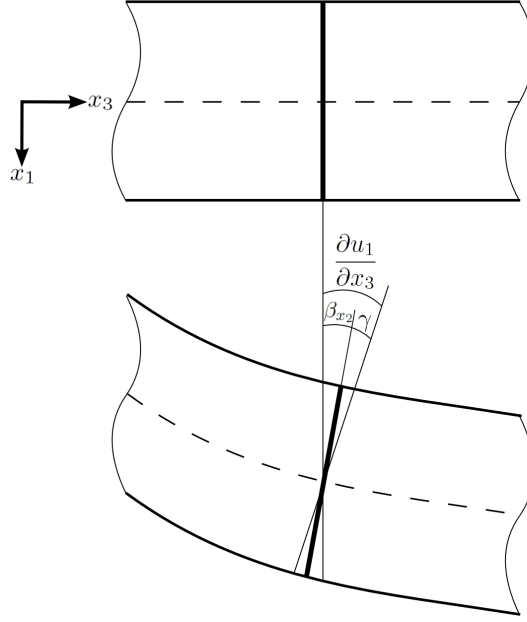


Figure 3.1: Lateral deformation of a Timoshenko beam. Note that the normal rotates by an amount β_{x_2} which is not equal to $\frac{\partial u_1}{\partial x_3}$.

These kinematics can be summarized as follows:

$$\frac{\partial u_1}{\partial x_3} = \beta_{x_2} + \gamma \quad (3.16)$$

$$\frac{\partial^2 u_1}{\partial x_3^2} = \frac{\partial \beta_{x_2}}{\partial x_3} + \frac{\partial \gamma}{\partial x_3} = \kappa_{x_2} + \frac{\partial \gamma}{\partial x_3} \quad (3.17)$$

$$\frac{\partial^3 u_1}{\partial x_3^3} = \frac{\partial \kappa_{x_2}}{\partial x_3} \quad (3.18)$$

with β_{x_2} the rotation of the section, γ the shear deformation angle and κ_{x_2} the bending curvature.

Finally, the shear force T and bending moment M can be expressed in function of derivatives of the lateral displacement u_1 :

$$T = k\mu A\gamma = -\frac{\partial M}{\partial x_3} = -EI\frac{\partial \kappa_{x_2}}{\partial x_3} = -EI\frac{\partial^3 u_1}{\partial x_3^3} \quad (3.19)$$

$$M = EI\frac{\partial \beta_{x_2}}{\partial x_3} = EI\left(\frac{\partial^2 u_1}{\partial x_3^2} - \frac{\partial \gamma}{\partial x_3}\right) = EI\left(\frac{\partial^2 u_1}{\partial x_3^2} + \frac{EI}{k\mu A}\frac{\partial^4 u_1}{\partial x_3^4}\right) \quad (3.20)$$

Introducing the boundary conditions Eqs. (3.12)–(3.15) in the general solution Eq. (3.11), and taking the expressions (3.19) and (3.20) into account, provides another system of equations from which the unknown coefficients A^I to D^{II} are determined:

$$\begin{bmatrix}
e^{\lambda_1 x_3^j} & e^{\lambda_2 x_3^j} & e^{\lambda_3 x_3^j} & e^{\lambda_4 x_3^j} & -e^{\lambda_1 x_3^j} & -e^{\lambda_2 x_3^j} & -e^{\lambda_3 x_3^j} & -e^{\lambda_4 x_3^j} \\
\lambda_1 e^{\lambda_1 x_3^j} & \lambda_2 e^{\lambda_2 x_3^j} & \lambda_3 e^{\lambda_3 x_3^j} & \lambda_4 e^{\lambda_4 x_3^j} & -\lambda_1 e^{\lambda_1 x_3^j} & -\lambda_2 e^{\lambda_2 x_3^j} & -\lambda_3 e^{\lambda_3 x_3^j} & -\lambda_4 e^{\lambda_4 x_3^j} \\
\lambda_1^3 & \lambda_2^3 & \lambda_3^3 & \lambda_4^3 & 0 & 0 & 0 & 0 \\
\zeta_1 & \zeta_2 & \zeta_3 & \zeta_4 & 0 & 0 & 0 & 0 \\
0 & 0 & 0 & 0 & \lambda_1^3 e^{\lambda_1 L_p} & \lambda_2^3 e^{\lambda_2 L_p} & \lambda_3^3 e^{\lambda_3 L_p} & \lambda_4^3 e^{\lambda_4 L_p} \\
0 & 0 & 0 & 0 & \zeta_1 e^{\lambda_1 L_p} & \zeta_2 e^{\lambda_2 L_p} & \zeta_3 e^{\lambda_3 L_p} & \zeta_4 e^{\lambda_4 L_p} \\
\zeta_1 e^{\lambda_1 x_3^j} & \zeta_2 e^{\lambda_2 x_3^j} & \zeta_3 e^{\lambda_3 x_3^j} & \zeta_4 e^{\lambda_4 x_3^j} & -\zeta_1 e^{\lambda_1 x_3^j} & -\zeta_2 e^{\lambda_2 x_3^j} & -\zeta_3 e^{\lambda_3 x_3^j} & -\zeta_4 e^{\lambda_4 x_3^j} \\
\lambda_1^3 e^{\lambda_1 x_3^j} & \lambda_2^3 e^{\lambda_2 x_3^j} & \lambda_3^3 e^{\lambda_3 x_3^j} & \lambda_4^3 e^{\lambda_4 x_3^j} & -\lambda_1^3 e^{\lambda_1 x_3^j} & -\lambda_2^3 e^{\lambda_2 x_3^j} & -\lambda_3^3 e^{\lambda_3 x_3^j} & -\lambda_4^3 e^{\lambda_4 x_3^j}
\end{bmatrix}
\begin{Bmatrix}
A^I \\
B^I \\
C^I \\
D^I \\
A^{II} \\
B^{II} \\
C^{II} \\
D^{II}
\end{Bmatrix}
=
\begin{Bmatrix}
0 \\
0 \\
0 \\
0 \\
0 \\
0 \\
0 \\
1/EI
\end{Bmatrix}
\quad (3.21)$$

with $\zeta_i = \lambda_i^2 + \frac{EI}{k\mu A} \lambda_i^4$ for $i = 1, \dots, 4$.

Furthermore, the pile's response to a unit moment load applied at the pile-head can be determined. The transverse behaviour is still described by Eq. (3.11), but only one section of the pile has to be considered (since the moment is applied at the pile-head). The four necessary coefficients A^I , B^I , C^I and D^I can be obtained by incorporating the appropriate boundary conditions. The pile-tip should be free of shear forces and bending moments:

$$T_{x_3=0} = 0 \quad \text{and} \quad M_{x_3=0} = 0 \quad (3.22)$$

$$T_{x_3=L_p} = 0 \quad \text{and} \quad M_{x_3=L_p} = 1 \quad (3.23)$$

Eqs. (3.22) and (3.23) provide a system of four equations from which the four necessary coefficients A^I to D^I are obtained:

$$\begin{bmatrix}
\zeta_1 & \zeta_2 & \zeta_3 & \zeta_4 \\
\zeta_1 e^{\lambda_1 L_p} & \zeta_2 e^{\lambda_2 L_p} & \zeta_3 e^{\lambda_3 L_p} & \zeta_4 e^{\lambda_4 L_p} \\
\lambda_1^3 & \lambda_2^3 & \lambda_3^3 & \lambda_4^3 \\
\lambda_1^3 e^{\lambda_1 L_p} & \lambda_2^3 e^{\lambda_2 L_p} & \lambda_3^3 e^{\lambda_3 L_p} & \lambda_4^3 e^{\lambda_4 L_p}
\end{bmatrix}
\begin{Bmatrix}
A^I \\
B^I \\
C^I \\
D^I
\end{Bmatrix}
=
\begin{Bmatrix}
0 \\
1/EI \\
0 \\
0
\end{Bmatrix}
\quad (3.24)$$

Once the values of the coefficients are found, the FRF matrix \mathbf{H}_p of the pile can be assembled, as illustrated in paragraph 2.2.3.

3.1.2 Results

The influence of incorporating Timoshenko beam theory is assessed by means of the driving point FRFs H_{ij} of the pile-head (i.e. \mathbf{u}_{ph}^i due to \mathbf{f}_{ph}^j). A common form to present the latter are flexibility coefficients F_{ij} , which are obtained by normalizing the FRFs with respect to their predicted static value:

$$F_{ij} = I_{ij} + iJ_{ij} = \frac{H_{ij}(\omega)}{H_{ij}(0)} \quad (3.25)$$

An analysis is carried out for a pile with $L_p = 7.50$ m and $d_p = 1/\sqrt{2}$ m. As mentioned before, the soil-pile circumference is discretized by means of square elements. The size of the elements is limited to

0.50 m, in order to satisfy the recommendation of Dominguez [13] that at least six constant elements per wavelength should be used in an elastodynamic analysis. The number of elements N_{fs} of the free surface has been increased stepwise until convergence of the results was obtained.

The effect of incorporating Timoshenko beam theory on the flexibility coefficients is illustrated in Figure 3.2. The values of F_{ij} are plotted in function of the non-dimensional frequency $a_0 = \omega r / c_s$. r is the pile's radius ($r = d_p/2$) and c_s is the shear wave velocity in the soil. Only the quantities related to motion in the (x_1, x_3) -plane are presented, as it is assumed that the local deformation of the pile can be neglected. The flexibility coefficients related to motion in the (x_2, x_3) -plane are identical to the ones presented here. Figures 3.2(a), 3.2(c) and 3.2(d) show discrepancies arising from $a_0 \simeq 0.5$ onwards. With the parameters under consideration, this corresponds with a frequency of 50 Hz. It is also obvious that there is no difference at all between the two beam theories for F_{33} , as it is assumed that the longitudinal behaviour is completely uncoupled from the transverse one (Figure 3.2(b)).

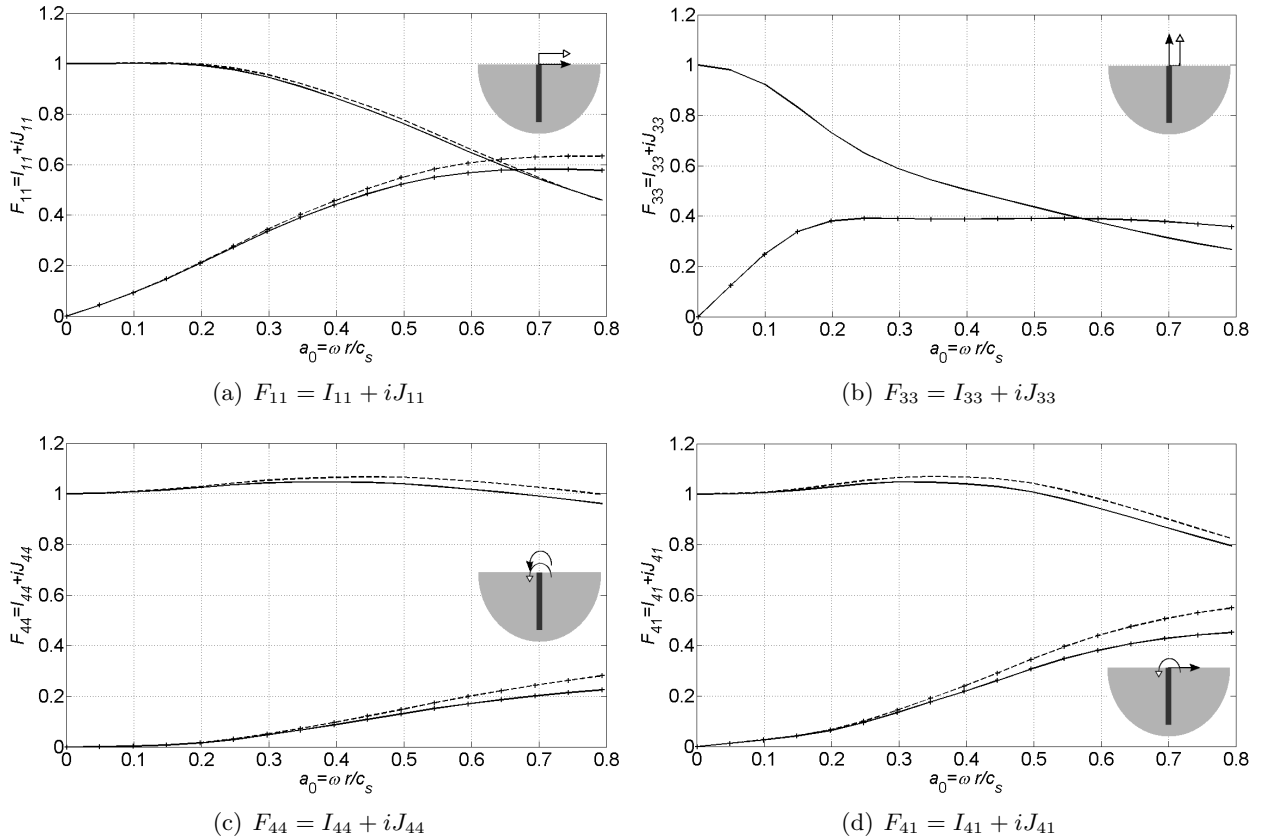


Figure 3.2: Flexibility coefficients (a) F_{11} , (b) F_{33} , (c) F_{44} and (d) F_{41} vs. dimensionless frequency a_0 , as computed using Euler beam theory (dashed line) and Timoshenko beam theory (solid line). The real parts I_{ij} are given as plain lines, while the absolute value of the imaginary parts J_{ij} are marked by crosses. Following parameters are used in the calculation: $L_p/d_p = 10.6$, $\mu_p/\mu_s = 100$, $\rho_s/\rho_p = 0.75$, $\nu_s = 0.40$ and $\nu_p = 0.25$.

The corrections introduced by Timoshenko's assumptions seem to be relatively small. Table 3.1 summarizes the maximum relative differences between Euler-Bernoulli and Timoshenko beam theory for the case of Figure 3.2. It can be concluded that there are significant differences for J_{44} and J_{41} , which are the imaginary parts of the pile-head rotation due to a unit moment respectively a unit shear force applied at the pile-head. Therefore, Timoshenko beam theory will be used throughout the remainder of this dissertation.

	I_{ij}	J_{ij}
F_{11}	2%	10%
F_{33}	0%	0%
F_{44}	4%	25%
F_{41}	4%	21%

Table 3.1: Maximum relative differences between Euler-Bernoulli and Timoshenko beam theory for the case of Figure 3.2.

3.2 Power flow analysis

In order to gain more insight into the behaviour of the system, it is considered useful to carry out a power flow analysis. This concept will also be used in chapters 6 and 7.

The instantaneous power flow P through a section is equal to the instantaneous rate at which N generalized forces f_j do work against N generalized displacements u_j . It is the sum of the different contributions P_j related to a degree of freedom j :

$$P = \sum_{j=1}^N P_j = \sum_{j=1}^N -\Re(v_j)\Re(f_j) \quad (3.26)$$

where v_j are generalized velocities. The expression for P_j can be elaborated by introducing the complex notation for v_j and f_j :

$$P_j = -\Re(v_j)\Re(f_j) \quad (3.27)$$

$$= -\Re\left(\frac{\partial u_j e^{i\omega t}}{\partial t}\right)\Re(f_j e^{i\omega t}) \quad (3.28)$$

$$= -\Re(i\omega u_j e^{i\omega t})\Re(f_j e^{i\omega t}) \quad (3.29)$$

Both u_j and f_j are complex quantities, and may be expressed as $u_j = u_{\Re} + iu_{\Im}$ respectively $f_j = f_{\Re} + if_{\Im}$. Introducing these expressions and making use of Euler's formula gives:

$$P_j = -\Re(i\omega(u_{\Re} + iu_{\Im})(\cos \omega t + i \sin \omega t))\Re((f_{\Re} + if_{\Im})(\cos \omega t + i \sin \omega t)) \quad (3.30)$$

$$= \omega(u_{\Re}f_{\Re} - u_{\Im}f_{\Im}) \sin \omega t \cos \omega t - \omega u_{\Re}f_{\Im} \sin^2 \omega t + \omega u_{\Im}f_{\Re} \cos^2 \omega t \quad (3.31)$$

The first term on the right-hand side of Eq. (3.31) is known as the reactive power. Its mean value over one period T is equal to zero. It represents the power required to balance the fluctuating total energy (potential and kinetic) of the body [46]. The two remaining terms on the right-hand side of Eq. (3.31) have a non-zero mean value and represent the power dissipated by the damping. This dissipative mean power flow can finally be written as:

$$\overline{P}_j = \frac{1}{T} \int_0^T P_j dt \quad (3.32)$$

$$= -\frac{1}{2} \omega (u_{\Re} f_{\Im} - u_{\Im} f_{\Re}) \quad (3.33)$$

$$= -\frac{1}{2} \Re(i\omega u_j f_j^*) \quad (3.34)$$

where f_j^* denotes the complex conjugate of f_j .

The concept is illustrated for a single pile with length $L_p = 10.5$ m and diameter $d_p = 1/\sqrt{2}$ m. The soil and pile parameters are summarized in Table 5.1. A unit load \mathbf{f}_{ph} is applied at the pile-head, and the response of the pile is calculated by means of Eq. (2.31). The mean power input \overline{P}_{in} can be expressed as follows:

$$\overline{P}_{in} = -\frac{1}{2} \Re(i\omega \mathbf{u}_{ph} \cdot \mathbf{f}_{ph}^*) \quad (3.35)$$

To obtain the mean output power \overline{P}_{out} , \overline{P} should be integrated over the pile-soil interface. Due to the discrete character of the boundary element mesh under consideration, the integration is approximated as:

$$\overline{P}_{out} = \int_{sp} \overline{P} dA \quad (3.36)$$

$$\simeq -\frac{b_p h_p}{2} \Re \left(\sum_{j=1}^{N_{sp}} i\omega \mathbf{u}_{sp}^j \cdot \mathbf{p}_{sp}^{*j} \right) \quad (3.37)$$

where N_{sp} denotes the number of elements at the soil-pile interface.

In case of zero pile damping ($\beta_{\mu p} = 0$, $\beta_{\lambda p} = 0$), the mean output power \overline{P}_{out} must be identical to the mean input power \overline{P}_{in} at the pile-head. This conservation of energy is illustrated in Figures 3.3(a), 3.3(c) and 3.3(e), for a unit horizontal, vertical and moment load respectively. It is clear that the approximation made by Eq. (3.37) still gives a satisfying result. Figures 3.3(b), 3.3(d) and 3.3(f) show a front view of the pile and the free surface for the different load cases, at 25 Hz. The pile body is filled with a grey shadow of which the darkness indicates the magnitude of the power flowing through the pile's section. The convention used in these figures is that positive values represent a downstream power flow, i.e. from the pile-head to the pile-tip. The arrows perpendicular to the boundary elements correspond to power flowing through the pile skin. It must be emphasized that these arrows do not represent a vector quantity (as power is something purely scalar), but they are used to indicate the difference between power flowing inwards and power flowing outwards.

From Figure 3.3(b), it can be seen that power entering the pile due to a horizontal load is mainly radiated through the upper part of the pile skin, while the power radiation due to a vertical load

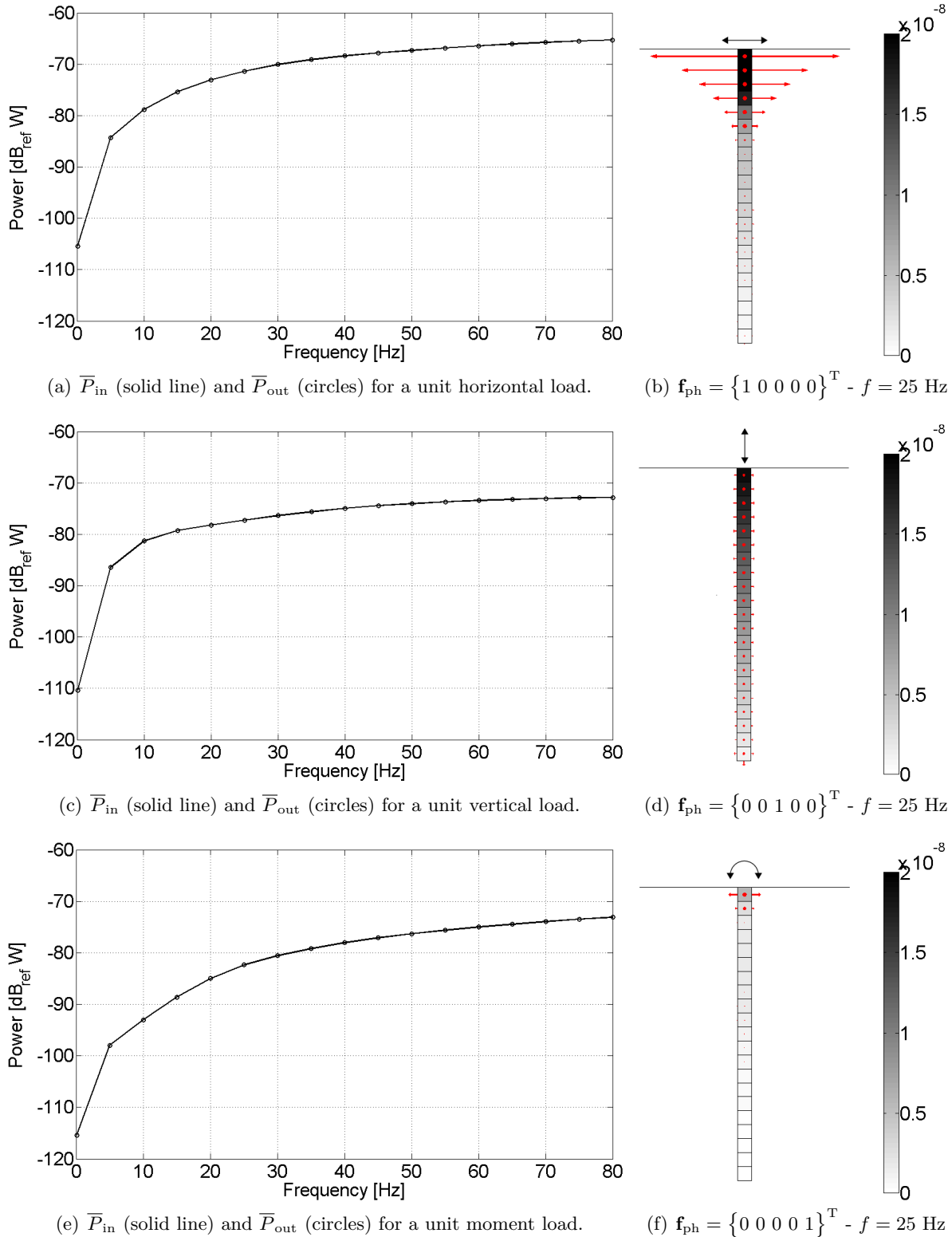


Figure 3.3: Power flow analysis for a unit (a)-(b) horizontal, (c)-(d) vertical and (e)-(f) moment load \mathbf{f}_{ph} applied at the pile-head. Figures (a), (c) and (e) clearly demonstrate the conservation of energy. The power flow distribution at 25 Hz is illustrated in (b), (d) and (f). The pile body is filled with a grey shadow of which the darkness indicates the magnitude of the power flowing through the pile's section. The arrows perpendicular to the boundary elements correspond to power flowing through the pile skin.

(Figure 3.3(d)) occurs more uniformly along the pile. The latter is a reasonable result, as one expects a quasi-uniform distribution of shear stresses along the pile skin.

The usefulness of a power flow analysis can also be illustrated by means of a case in which a load \mathbf{p}_{fs} is applied to the free surface. The same pile and soil parameters are used as in the example above. The response of the pile to a prescribed traction \mathbf{p}_{fs} can be obtained from Eqs. (2.6), (2.26), (2.28) and (2.30):

$$\mathbf{u}_p = b_p h_p \left(\mathbf{I} + b_p h_p \mathbf{H}_p^{22} \mathbf{Q}_1^T [\mathbf{H}_s^{22}]^{-1} \mathbf{Q}_1 \right)^{-1} \mathbf{H}_p^{22} \mathbf{Q}_1^T [\mathbf{H}_s^{22}]^{-1} \mathbf{H}_s^{21} \mathbf{p}_{fs} \quad (3.38)$$

Once \mathbf{u}_p is calculated, the remaining unknowns can be found.

As in the example above, zero pile damping is assumed to check the conservation of energy. As there is no power input at the pile-head, the sum of the power entering the pile has to be equal to the sum of the power leaving the pile. This is demonstrated in Figure 3.4(a) for the case of a prescribed horizontal traction on the surface of the half-space, at a distance $R = 3.50$ m from the pile-head. Figure 3.4(b) illustrates the power flow distribution at 25 Hz. It can be seen that power enters the upper left-hand side of the pile, from where it partly flows through the upper right-hand side and partly downwards along the pile's central axis. Eventually, power is radiated through both the lower left- and right-hand sides of the pile, as well as through the pile-tip. Of course, there is also power flowing through the elements of the pile skin in the (x_2, x_3) -plane, but this is an order of magnitude less than the power flow through the elements in the (x_1, x_3) -plane.

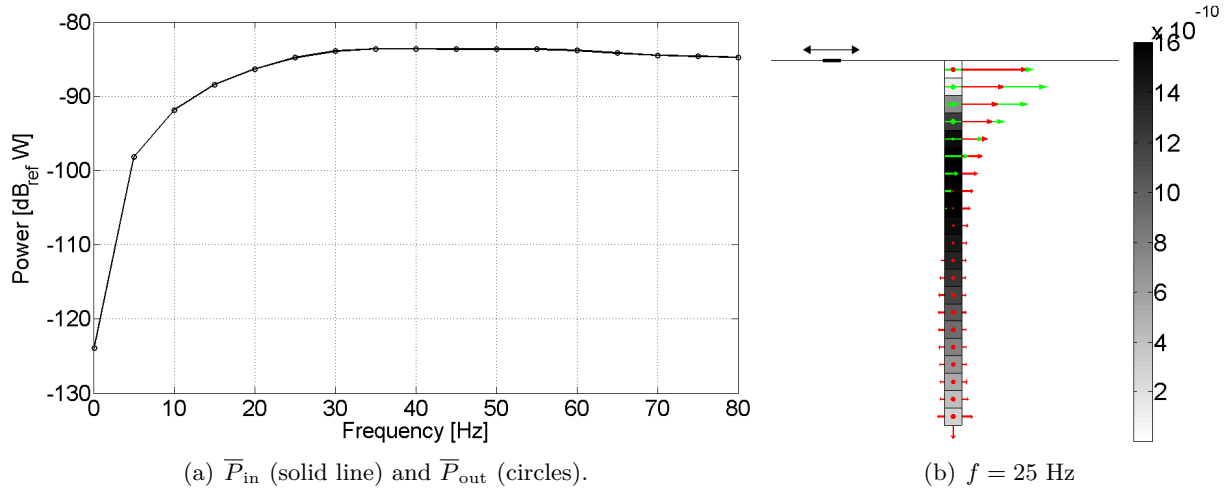


Figure 3.4: Power flow analysis for a prescribed horizontal traction \mathbf{p}_{fs} at a distance $R = 3.50$ m from the pile-head. Figure (a) clearly demonstrates the conservation of energy. The power flow distribution at 25 Hz is illustrated in (b).

3.3 Incorporation of a building model: a semi-infinite column

The model developed in the previous sections gives only a representation of a foundation, without any coupling to an above structure. Such a coupling will be considered in this section.

One possible approach, beside many others, is to represent the building as a (two-dimensional) portal frame. The finite element method or the dynamic stiffness method are widely used techniques in these models [11, 46]. However, it is rather difficult to devise a generic model which is representative for a large amount of structures. Therefore, a much more simplistic approach is chosen here. The structure situated on top of a pile is represented as a semi-infinite column, which is equivalent to a viscous damper (Figure 3.5).

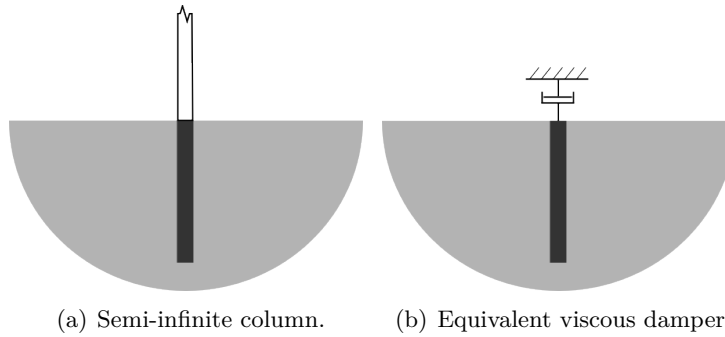


Figure 3.5: Representation of the simplistic building model.

Consider a semi-infinite bar as in Figure 3.6, excited by a longitudinal force N at its end. The mechanical driving point impedance Z_{long} is defined as:

$$Z_{\text{long}} = \frac{\hat{N}}{\hat{u}_0} \quad (3.39)$$

with \hat{u}_0 the driving point's longitudinal velocity.

The following partial differential equation describes the longitudinal motion of the bar:

$$EA \frac{\partial^2 u(x, t)}{\partial x^2} = m \frac{\partial^2 u(x, t)}{\partial t^2} \quad (3.40)$$

Introducing the complex notation $u(x, t) = \Re(\hat{u}(x, \omega)e^{i\omega t})$ results in an ODE in function of $\hat{u}(x, \omega)$:

$$EA \frac{\partial^2 \hat{u}(x, \omega)}{\partial x^2} + m\omega^2 \hat{u}(x, \omega) = 0 \quad (3.41)$$

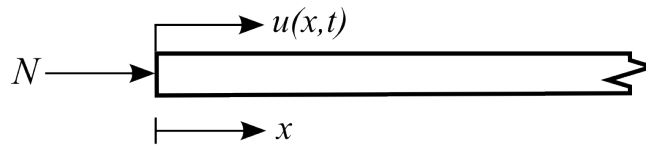


Figure 3.6: Longitudinal excitation of a semi-infinite bar.

The general solution of $u(x, t)$ can therefore be written as:

$$u(x, t) = \Re\left(\hat{C}_1 e^{i(\omega t + \alpha x)} + \hat{C}_2 e^{i(\omega t - \alpha x)}\right) \quad (3.42)$$

with $\alpha = \omega \sqrt{\frac{\rho}{E}}$. The coefficients \hat{C}_1 and \hat{C}_2 can be determined on the basis of the boundary conditions. As a semi-infinite bar is under consideration, no reflection can take place, and only waves propagating in the positive x -direction will be present. Therefore, the coefficient \hat{C}_1 has to be set to zero, as it is associated with the term that represents waves travelling in the negative x -direction. Furthermore, force equilibrium should be satisfied at $x = 0$, for every time t :

$$N + EA \left(\frac{\partial u(x, t)}{\partial x} \right)_{x=0} = 0 \quad (3.43)$$

Using Eq. (3.42) allows to solve Eq. (3.43) for the unknown coefficient \hat{C}_2 :

$$\hat{N} - EA \hat{C}_2 i \alpha = 0 \quad (3.44)$$

$$\Rightarrow \hat{C}_2 = \frac{\hat{N}}{EA \alpha i} \quad (3.45)$$

Introducing Eq. (3.45) in Eq. (3.42) gives an expression for the driving point response u_0 :

$$u_0(t) = \Re\left(\frac{\hat{N}}{EA \alpha i} e^{i\omega t}\right) \quad (3.46)$$

Finally, the mechanical driving point impedance Z_{long} , as defined by Eq. (3.39), can be obtained:

$$Z_{\text{long}} = \frac{\hat{N}}{\frac{\hat{N} i \omega}{EA \alpha i}} \quad (3.47)$$

$$= \frac{EA \alpha}{\omega} \quad (3.48)$$

This impedance can be rewritten as:

$$Z_{\text{long}} = \sqrt{mEA} \quad (3.49)$$

$$= m c_L \quad (3.50)$$

with

$$c_L = \sqrt{\frac{E}{\rho}} \quad (3.51)$$

the longitudinal wave velocity in the bar.

One could wonder whether a semi-infinite column is an acceptable representation of a structure or not. Due to the infinite nature of the model, energy will be radiated away from the excitation point, and this will prevent resonances from being established. However, Cryer [11] found that this behaviour

was more representative for real buildings, which do not exhibit the strong resonant behaviour of finite models [46].

Mechanical driving point impedances can not only be obtained for longitudinal motion, but also for bending waves. However, in order to deal with bending waves, one needs to take into account that the tip of the semi-infinite beam can be excited simultaneously by a shear force T and a bending moment M . The transverse and rotational driving point velocities \hat{v}_0 and $\hat{\theta}_0$ can be written as:

$$\hat{v}_0 = \frac{1}{Z_b} \hat{T} + \frac{1}{W'_b} \hat{M} \quad (3.52)$$

$$\hat{\theta}_0 = \frac{1}{W'_b} \hat{T} + \frac{1}{W_b} \hat{M} \quad (3.53)$$

with Z_b the shear force impedance, W_b the bending moment impedance and W'_b a coupling term between shear and bending. Expressions for these impedances can be obtained in a similar way as for the longitudinal motion [10]:

$$Z_b = \frac{1}{2} m c_B (1 + i) \quad (3.54)$$

$$W'_b = -\sqrt{EI} m \quad (3.55)$$

$$W_b = \frac{1}{2} m c_B \frac{1 - i}{\omega \sqrt{\frac{m}{EI}}} \quad (3.56)$$

with

$$c_B = \frac{\sqrt{\omega}}{\left(\frac{m}{EI}\right)^{1/4}} \quad (3.57)$$

the bending wave velocity in the bar.

In order to incorporate the semi-infinite column in the pile model, compatibility of displacements at the pile-head has to be considered: the displacements of the pile-head and the tip of the semi-infinite column are equal. Furthermore, equilibrium of forces ensures that an equal but opposite set of forces \mathbf{f}_{ph} acts on the tip of the column. Therefore, following relationship is established:

$$\mathbf{u}_{ph} = -\mathbf{H}_b \mathbf{f}_{ph} \quad (3.58)$$

or, fully elaborated:

$$\begin{Bmatrix} u_{ph1} \\ u_{ph2} \\ u_{ph3} \\ \theta_{ph1} \\ \theta_{ph2} \end{Bmatrix} = -\frac{1}{i\omega} \begin{bmatrix} \frac{1}{Z_{b1}} & 0 & 0 & 0 & \frac{1}{W'_{b1}} \\ 0 & \frac{1}{Z_{b2}} & 0 & \frac{1}{W'_{b2}} & 0 \\ 0 & 0 & \frac{1}{Z_{long}} & 0 & 0 \\ 0 & \frac{1}{W'_{b2}} & 0 & \frac{1}{W_{b2}} & 0 \\ \frac{1}{W'_{b1}} & 0 & 0 & 0 & \frac{1}{W_{b1}} \end{bmatrix} \begin{Bmatrix} f_{ph1} \\ f_{ph2} \\ f_{ph3} \\ m_{ph1} \\ m_{ph2} \end{Bmatrix} \quad (3.59)$$

where the subscripts b_1 and b_2 denote bending around the two different axes. \mathbf{H}_b is the displacement FRF matrix of the structure on top of the pile, in this case a semi-infinite column.

Introducing the extra constraint (3.58) implies that expression (3.38) is not valid anymore to calculate the response of the pile due to a load \mathbf{p}_{fs} applied to the free surface. Combining Eq. (2.26) and Eq. (3.58) results in following expression:

$$\mathbf{u}_{ph} = \left(\underbrace{\mathbf{I} + \mathbf{H}_p^{11} [\mathbf{H}_b]^{-1}}_{[\mathbf{L}]} \right)^{-1} \mathbf{H}_p^{21} \mathbf{f}_p = [\mathbf{L}]^{-1} \mathbf{H}_p^{21} \mathbf{f}_p \quad (3.60)$$

The response of the pile to a prescribed traction \mathbf{p}_{fs} can be obtained from Eqs. (2.6), (2.28), (2.30) and (3.60):

$$\mathbf{u}_p = b_p h_p \left(\mathbf{I} + b_p h_p \left(\mathbf{H}_p^{22} - \mathbf{H}_p^{21} [\mathbf{H}_b]^{-1} [\mathbf{L}]^{-1} \mathbf{H}_p^{12} \right) \mathbf{Q}_1^T [\mathbf{H}_s^{22}]^{-1} \mathbf{Q}_1 \right)^{-1} \dots \\ \left(\mathbf{H}_p^{22} - \mathbf{H}_p^{21} [\mathbf{H}_b]^{-1} [\mathbf{L}]^{-1} \mathbf{H}_p^{12} \right) \mathbf{Q}_1^T [\mathbf{H}_s^{22}]^{-1} \mathbf{H}_s^{21} \mathbf{p}_{fs} \quad (3.61)$$

Once \mathbf{u}_p is calculated, the remaining unknowns can be found.

The effect of incorporating the semi-infinite column in the BE pile model can again be illustrated by means of a power flow analysis (Figure 3.7). As in the case of Figure 3.4, a horizontal traction is applied on the surface of the half-space, at a distance $R = 3.50$ m from the pile-head. The same pile and soil parameters are used as in the example above. The parameters of the semi-infinite column are exactly the same as those of the pile. Again, zero pile damping is assumed in order to check the conservation of energy. In this case, \bar{P}_{in} is calculated as the sum of the power flow through the pile-soil interface boundary elements as in Eq. (3.34) (positive and negative contributions are summed up), while \bar{P}_{out} is equal to the power flowing into the semi-infinite column (or into the equivalent viscous damper):

$$\bar{P}_{out} = \bar{P}_{damper} = -\frac{1}{2} \Re(i\omega \mathbf{u}_{ph} \cdot \mathbf{f}_{ph}^*) \quad (3.62)$$

It is clear from Figure 3.7(a) that the conservation of energy is fulfilled. Figure 3.7(b) shows the power flow distribution at 25 Hz. Note that the scale of the pile body shading extends to a negative value. Based on the convention put forward in section 3.2, a negative value represents an upstream power flow. Hence, in contrast to Figure 3.4(b), there is also power flowing upwards through the pile-heads into the semi-infinite columns.

In order to reduce vibration levels in buildings, the use of vibration isolation bearings is often justified. These bearings are incorporated between the building and its foundation (Figure 3.8).

An isolation bearing is characterized by three stiffnesses (k_{vv} , k_{hh} and $k_{\theta\theta}$), associated with three modes of deformation, as illustrated schematically in Figure 3.9. Torsion about the vertical axis is neglected, and linear elasticity is assumed. The latter is justified in case of helical steel springs, while

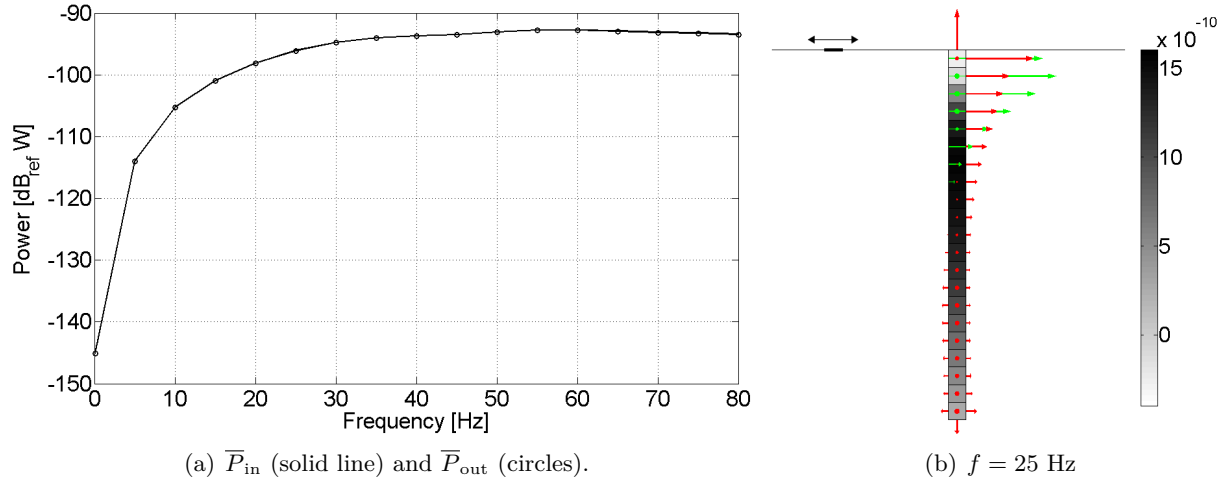


Figure 3.7: Power flow analysis for a prescribed horizontal traction \mathbf{p}_{fs} at a distance $R = 3.50$ m from the pile-head. A simplistic building model is incorporated in the model. Figure (a) clearly demonstrates the conservation of energy. The power flow distribution at 25 Hz is illustrated in (b).

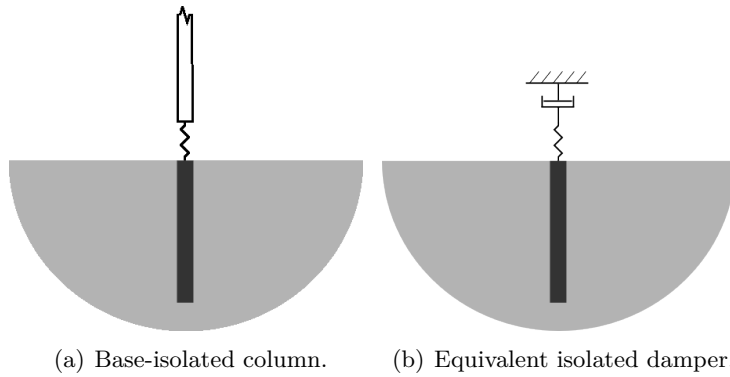


Figure 3.8: Representation of the simplistic base-isolated building model.

this is more difficult for rubber isolation bearings. However, Talbot [46] states, based on the work of Lindley [32], that it is reasonable to assume that the non-linear effects and the frequency-dependence of the elastic modulus are negligible under the conditions associated with base-isolated buildings.

The vertical stiffness k_{vv} is related to the isolation frequency f_{iso} by means of Eq. (3.63):

$$k_{vv} = 4\pi^2 f_{iso}^2 M \quad (3.63)$$

with M the mass supported per bearing. As a semi-infinite column is considered ($M = \infty$), one would obtain the non-physical result $k_{vv} = \infty$ for every value of f_{iso} . Therefore, a fixed value of M will be chosen, and f_{iso} will be varied. In this way, the relative influence of f_{iso} can be investigated (chapter 7), although judgement about absolute vibration levels is not possible. It is more difficult to obtain values for the horizontal and rotational stiffness k_{hh} and $k_{\theta\theta}$. They depend on the design

details of the particular application, but are generally less than the vertical stiffness k_{vv} . Throughout this dissertation, ratios $k_{hh}/k_{vv} = k_{\theta\theta}/k_{vv} = 0.5$ will be used, as suggested by Talbot [46].

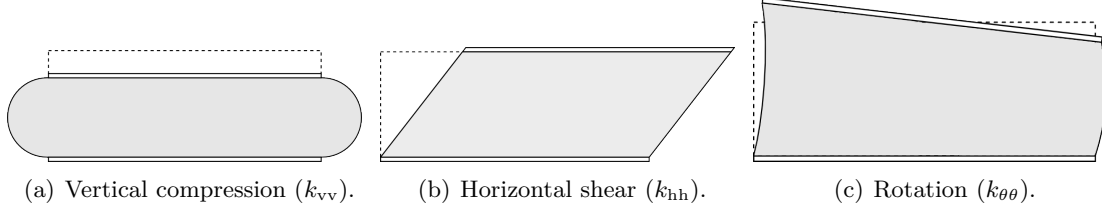


Figure 3.9: Three modes of deformation of a rubber isolation bearing.

In order to incorporate the isolation bearings in the mathematical formulation of the model, consider Figure 3.10. The goal is to find an expression for the FRF matrix \mathbf{H}_b , which relates the pile-head displacements \mathbf{u}_{ph} and forces \mathbf{f}_{ph} by means of Eq. (3.58). Force equilibrium at the tip of the semi-infinite column is written as:

$$-\mathbf{f}_{ph} = \mathbf{k}(\mathbf{u}_{ph} - \mathbf{u}_c) = [\mathbf{H}_c]^{-1}\mathbf{u}_c \quad (3.64)$$

with \mathbf{u}_c the displacement vector of the tip of the semi-infinite column and \mathbf{H}_c its FRF matrix. \mathbf{k} is a diagonal matrix and contains the stiffnesses k_{vv} , k_{hh} and $k_{\theta\theta}$. Rearranging Eq. (3.64) gives an expression for \mathbf{u}_c in function of \mathbf{u}_{ph} :

$$\mathbf{u}_c = \left([\mathbf{H}_c]^{-1} + \mathbf{k}\right)^{-1} \mathbf{k} \mathbf{u}_{ph} \quad (3.65)$$

Hence, the relation between \mathbf{f}_{ph} and \mathbf{u}_{ph} becomes:

$$-\mathbf{f}_{ph} = \mathbf{k} \left([\mathbf{H}_c]^{-1} + \mathbf{k}\right)^{-1} [\mathbf{H}_c]^{-1} \mathbf{u}_{ph} \quad (3.66)$$

The FRF matrix \mathbf{H}_b eventually yields:

$$\mathbf{H}_b = \mathbf{H}_c \left([\mathbf{H}_c]^{-1} + \mathbf{k}\right) [\mathbf{k}]^{-1} \quad (3.67)$$

$$= [\mathbf{k}]^{-1} + \mathbf{H}_c \quad (3.68)$$

or, fully elaborated:

$$\mathbf{H}_b = \begin{bmatrix} \frac{1}{k_{hh}} & 0 & 0 & 0 & 0 \\ 0 & \frac{1}{k_{hh}} & 0 & 0 & 0 \\ 0 & 0 & \frac{1}{k_{vv}} & 0 & 0 \\ 0 & 0 & 0 & \frac{1}{k_{\theta\theta}} & 0 \\ 0 & 0 & 0 & 0 & \frac{1}{k_{\theta\theta}} \end{bmatrix} + \frac{1}{i\omega} \begin{bmatrix} \frac{1}{Z_{b1}} & 0 & 0 & 0 & \frac{1}{W'_{b1}} \\ 0 & \frac{1}{Z_{b2}} & 0 & \frac{1}{W'_{b2}} & 0 \\ 0 & 0 & \frac{1}{Z_{long}} & 0 & 0 \\ 0 & \frac{1}{W'_{b2}} & 0 & \frac{1}{W_{b2}} & 0 \\ \frac{1}{W'_{b1}} & 0 & 0 & 0 & \frac{1}{W_{b1}} \end{bmatrix} \quad (3.69)$$

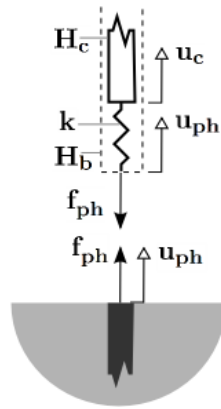
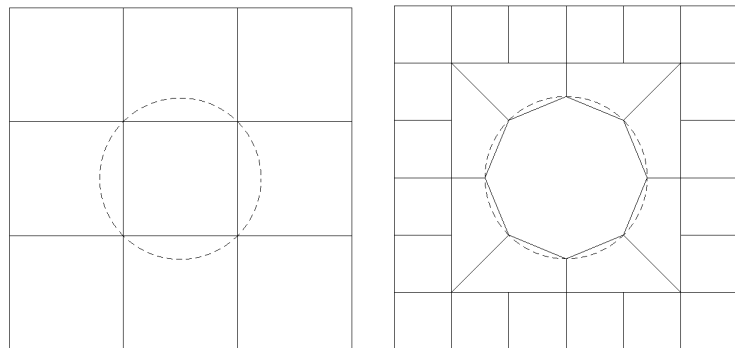


Figure 3.10: Coupling of the pile and the base-isolated semi-infinite column at the pile-head.

3.4 Geometrical extensions

A last important extension to the model has to deal with the boundary element mesh. In section 2.1, it was mentioned that the circular pile circumference used to be approximated by means of four elements (Figure 3.11(a)). In order to increase the accuracy of the pile model, an octagonal cross-section is introduced (Figure 3.11(b)). This requires non-rectangular elements on the free surface. Furthermore, a finer discretization of the free surface is used.



(a) Square cross-section and coarse mesh. (b) Octagonal cross-section and finer mesh.

Figure 3.11: Possible approximations of the circular pile soil interface (top view).

3.5 Conclusion

Several extensions to the single pile BE model have been introduced in this chapter. The incorporation of Timoshenko beam theory and the use of an octagonal cross-section to approximate the circular pile-soil interface are believed to increase the accuracy of the model. Other aspects, such as a power flow analysis and the incorporation of base isolation, have also been introduced and will be used throughout the following chapters.

Chapter 4

Validation of the PiP model for piles

As mentioned in section 1.3, one of the major aims of this dissertation is the validation of the so-called Pipe-in-Pipe model for piles, developed by Kuo [27]. The principles of this model are briefly summarized in section 4.1. Sections 4.2 and 4.3 address the validation of the model for an infinite pile in a full-space, respectively a finite pile in a half-space.

4.1 The PiP model for piles

The PiP model for piles is an efficient semi-analytical model based on the principles of the PiP model for underground railways. Firstly, an infinitely long pile is considered. The pile is modelled as a column in axial vibration and as an Euler-Bernoulli beam in lateral vibration. The soil is modelled as an elastic continuum with outer radius of infinity and inner radius equal to the pile radius. Combining the elastic continuum equations (as given by Forrest [14]), the standard equations for vibration of the pile and the appropriate boundary conditions at the pile-soil interface, gives the response of an infinite pile in a full-space.

In order to obtain an approximate response for a finite pile in a half-space, the mirror-image method is used. This method involves applying scaled forces and moments at two points equidistant from the required end-condition. By scaling the forces and moments to be equal and opposite to those forces and moments already existing in the infinite pile, a free end can be created [28]. The process of applying the mirror-image method to the infinite pile is described in [27]. This paper also contains a detailed derivation of the equations for an infinite pile.

4.2 Infinite pile

A first validation is carried out for an infinite pile in a full-space. With the BE pile model under consideration, an infinite pile is modelled as a finite pile with sufficient length. This pile is loaded by a unit harmonic force \mathbf{f}_m applied at $x_3 = L_p/2$ (i.e. the ‘middle’ of the pile, denoted as m).

4.2.1 Equations

The equations describing a pile in a full-space are in fact simplifications of those presented in chapter 2. As full-space Green's functions are already used in the BE formulation (section 2.1 and Appendix B), only the pile-soil interface has to be discretized. This means that the system of equations (2.6) reduces to:

$$\mathbf{H}\mathbf{u}_{\text{sp}} = \mathbf{G}\mathbf{p}_{\text{sp}} \quad (4.1)$$

By symmetry, rotation at the middle of an infinite pile must be zero. Therefore, the system of equations that expresses the behaviour of the pile has to be rearranged as follows:

$$\begin{Bmatrix} \mathbf{u}_m \\ \mathbf{u}_p \end{Bmatrix} = \begin{bmatrix} \mathbf{H}_p^{11} & \mathbf{H}_p^{12} \\ \mathbf{H}_p^{21} & \mathbf{H}_p^{22} \end{bmatrix} \begin{Bmatrix} \mathbf{f}_m \\ \mathbf{f}_p \end{Bmatrix} \quad (4.2)$$

where

$$\mathbf{u}_m = \{u_1^m \quad u_2^m \quad u_3^m \quad 0 \quad 0\}^T \quad (4.3)$$

collects the degrees of freedom of the node at $x_3 = L_p/2$, and

$$\mathbf{u}_p = \{u_1^{-N_p} \quad u_2^{-N_p} \quad u_3^{-N_p} | \dots | u_1^{-p1} \quad u_2^{-p1} \quad u_3^{-p1} | u_1^{p1} \quad u_2^{p1} \quad u_3^{p1} | \dots | u_1^{N_p} \quad u_2^{N_p} \quad u_3^{N_p}\}^T \quad (4.4)$$

collects the degrees of freedom of the remaining pile nodes. \mathbf{H}_p is assembled using Timoshenko beam theory, as described in section 3.1. Note that \mathbf{u}_p contains displacements of nodes above as well as beneath $x_3 = L_p/2$. Furthermore, as an infinite pile is considered, there is no pile-tip incorporated in the equations.

As described in section 2.3, the compatibility of displacements of the pile and the pile-soil interface, as well as the equilibrium of forces should be satisfied (expressed by Eq. (2.28) and Eq. (2.30)). However, since there is no pile-tip, the transformation matrix $\mathbf{Q}_{1\infty}$ is slightly different from \mathbf{Q}_1 . The matrix $\mathbf{Q}_{1\infty}$ is specified in Appendix C.

In a similar way as in section 2.3, the different equations can be combined in order to obtain the response of the pile to a prescribed load \mathbf{f}_m :

$$\mathbf{u}_p = \left(\mathbf{I} + b_p h_p \mathbf{H}_p^{22} \mathbf{Q}_{1\infty}^T [\mathbf{H}_s]^{-1} \mathbf{Q}_{1\infty} \right)^{-1} \mathbf{H}_p^{21} \mathbf{f}_m \quad (4.5)$$

Once \mathbf{u}_p is calculated, the remaining unknowns can be found.

4.2.2 Comparison

The current model for an infinite pile is compared to the PiP model for piles in terms of the driving point FRFs (i.e. \mathbf{u}_m due to \mathbf{f}_m). Before starting any comparison, one needs to determine which pile length in the BE model can be considered as sufficient in order to model the behaviour of an infinite pile. Therefore, a first calculation is performed for a length $L_p = 20$ m, and the pile displacements \mathbf{u}_p are investigated. The soil and pile parameters are summarized in Table 4.1.

Parameter	Soil	Pile
E [Pa]	252×10^6	40×10^9
ν [-]	0.40	0.30
μ [Pa]	90×10^6	15.4×10^9
λ [Pa]	360×10^6	23.1×10^9
ρ [kg/m ³]	2250	2800
β_μ [-]	0.03	0.05
β_λ [-]	0.03	0.05
c_s [m/s]	200.1	2344
c_p [m/s]	490.1	4385.3
d [m]	–	$1/\sqrt{2}$

Table 4.1: Soil and pile parameters used in the validation of the PiP model for piles.

Figure 4.1(a) shows the ratio of the transverse displacements \mathbf{u}_{p_1} of the different pile nodes to the transverse displacement u_1^m of the node at $x_3 = L_p/2$, due to a unit transverse load $\mathbf{f}_m = \{1 \ 0 \ 0 \ 0 \ 0\}^T$. It is clear that at a distance of 10 m from the excitation point, the displacement field has been considerably reduced in the frequency range under consideration. Hence, $L_p = 20$ m could already be regarded as a reasonable approximation when modelling the transverse behaviour of an infinite pile. As one can expect, the situation is worse for a longitudinal excitation $\mathbf{f}_m = \{0 \ 0 \ 1 \ 0 \ 0\}^T$, as illustrated in Figure 4.1(b). The decay of the longitudinal displacement field is much less than in the previous case; at a distance of 10 m from the excitation point, the relative magnitude of \mathbf{u}_{p_3} is still almost 60% over the whole frequency range. It is clear that a greater pile length has to be taken into account to model the longitudinal behaviour of an infinite pile correctly.

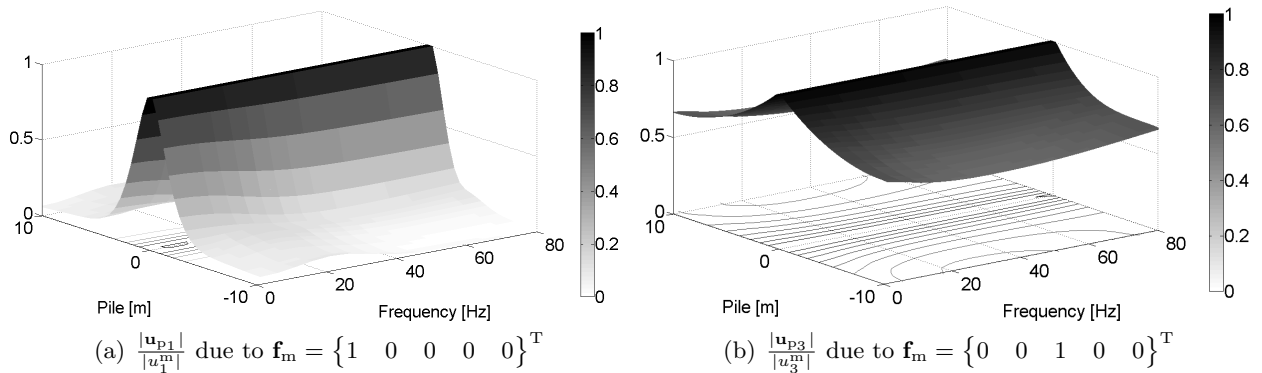


Figure 4.1: Relative magnitude of (a) transverse and (b) longitudinal pile displacements in a full-space, in function of the longitudinal coordinate and the frequency. The zero pile coordinate indicates the excitation point.

The results of the PiP model for piles are compared to the results of four different configurations of the BE pile model. The parameters of these configurations are summarized in Table 4.2.

Configuration	L_p [m]	Cross-section	b_p [m]	h_p [m]
1	20	square	0.50	0.50
2	100	square	0.50	0.50
3	20	octagonal	$\frac{\cos \frac{3\pi}{8}}{\sqrt{2}} \simeq 0.27$	0.50
4	40	octagonal	$\frac{\cos \frac{3\pi}{8}}{\sqrt{2}} \simeq 0.27$	0.50

Table 4.2: Parameters of the four BE pile model configurations used in the validation of the PiP model for piles, in case of an infinite pile in a full-space.

In Figure 4.2, the modulus and phase of the transverse driving point FRF are shown. They are plotted in function of the non-dimensional frequency $a_0 = \omega r/c_s$. As expected, one can observe that the response is not significantly influenced when the pile length is increased from $L_p = 20$ m to $L_p = 40$ m or $L_p = 100$ m. When modelling the pile-soil interface with a square cross-section, a difference of ~ 1 dB between the PiP model for piles and the BE pile model is encountered. Adapting the former to an octagonal cross-section reduces the discrepancy further to less than 0.5 dB, and it is believed that adding supplementary elements around the circumference will make the results of the two models to coincide. However, such a calculation would require considerable computation time.

The modulus and phase of the longitudinal driving point FRF are presented in Figure 4.3. It is clear that they both deviate from the result obtained with the PiP model for piles when only a length of 20 m is taken into account. Increasing the latter and considering an octagonal cross-section make the models to match more closely. It is remarkable to note in Figure 4.3(b) that for both models the phase does not drop to zero for the static solution ($a_0 = 0$). The reason for this artefact remains unclear.

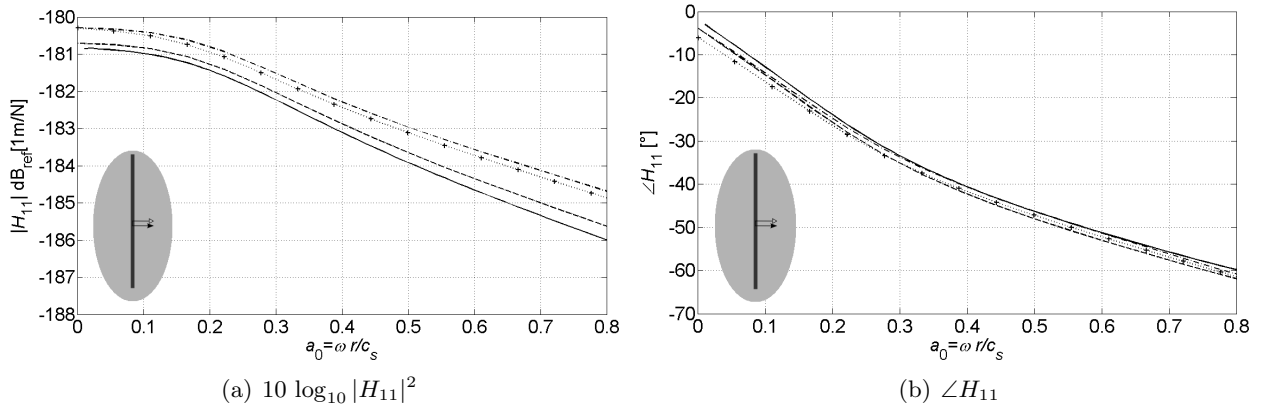


Figure 4.2: Transverse driving point FRF of an infinite pile vs. dimensionless frequency a_0 , as computed using configuration 1 (crossed line), configuration 2 (dash-dot line), configuration 3 (dotted line), configuration 4 (dashed line) and the PiP model for piles (solid line).

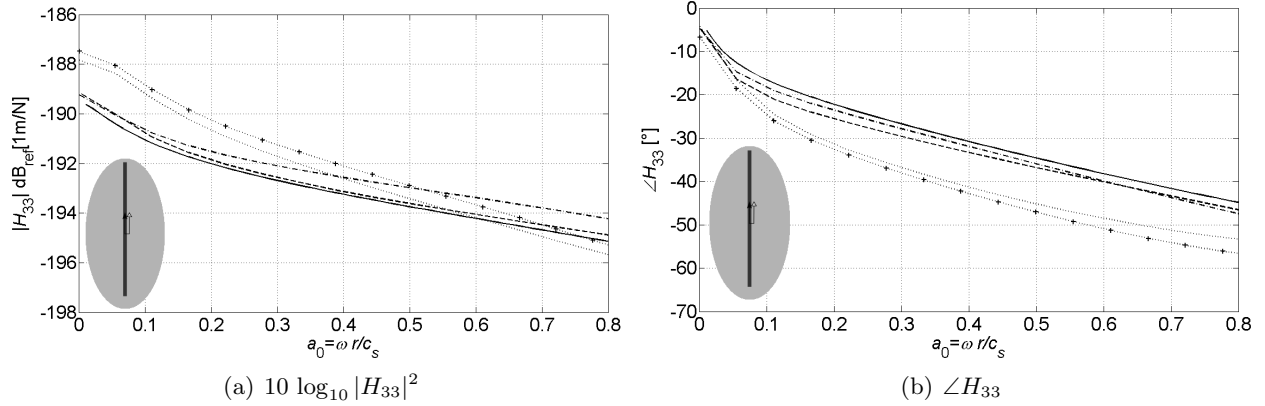


Figure 4.3: Longitudinal driving point FRF of an infinite pile vs. dimensionless frequency a_0 , as computed using configuration 1 (crossed line), configuration 2 (dash-dot line), configuration 3 (dotted line), configuration 4 (dashed line) and the PiP model for piles (solid line).

4.3 Finite pile

4.3.1 Equations

The equations for a single pile in a half-space have been elucidated extensively in chapter 2. The response of the pile to a prescribed pile-head load \mathbf{f}_{ph} can be calculated by means of Eq. (2.31), while the other unknowns can be obtained from Eqs. (2.6), (2.26), (2.28) and (2.30). It must however be emphasized that in the PiP model for piles of Kuo [27], the rotation of the pile-head is constrained. Therefore, the condition (2.18b) of zero bending moment at the pile-head has to be replaced by a condition of zero rotation:

$$\left(\frac{\partial u_1^{\text{II}}}{\partial x_3} \right)_{x_3=L_p} = 0 \quad (4.6)$$

This modified condition will have an influence on the pile's FRF matrix \mathbf{H}_p .

4.3.2 Comparison

As in the case of an infinite pile, a comparison between the current single pile BE model and the PiP model for piles is made in terms of the driving point FRFs (i.e. \mathbf{u}_{ph} due to \mathbf{f}_{ph}). This is done for a pile with $L_p = 20$ m; all the other pile and soil parameters remain the same as in Table 4.1. The results of the PiP model for piles are compared to the results of three different configurations of the BE pile model. The parameters of these configurations are summarized in Table 4.3.

Configuration	Cross-section	b_p [m]	h_p [m]	b_1 [m]	b_2 [m]
1	square	0.50	0.50	0.50	0.50
2	square	0.25	0.25	0.25	0.25
3	octagonal	$\frac{\cos \frac{3\pi}{8}}{\sqrt{2}} \simeq 0.27$	0.25	0.25	0.25

Table 4.3: Parameters of the three BE pile model configurations used in the validation of the PiP model for piles, in case of a finite pile in a half-space.

Figure 4.4 shows the modulus and phase of the transverse driving point FRF. When a square cross-section is used to model the soil-pile interface, a difference up to ~ 2 dB can be notified. Reducing the dimensions of the boundary elements has only a minimal effect. On the other hand, using an octagonal cross-section trims this difference down to less than 1 dB, and again, it is believed that adding more elements around the circumference will result in even a better match. Almost the same story is true for the longitudinal driving point FRF (Figure 4.5): reducing the dimensions of the elements in the case of a square cross-section does not influence the results significantly, but using an octagonal cross-section does.

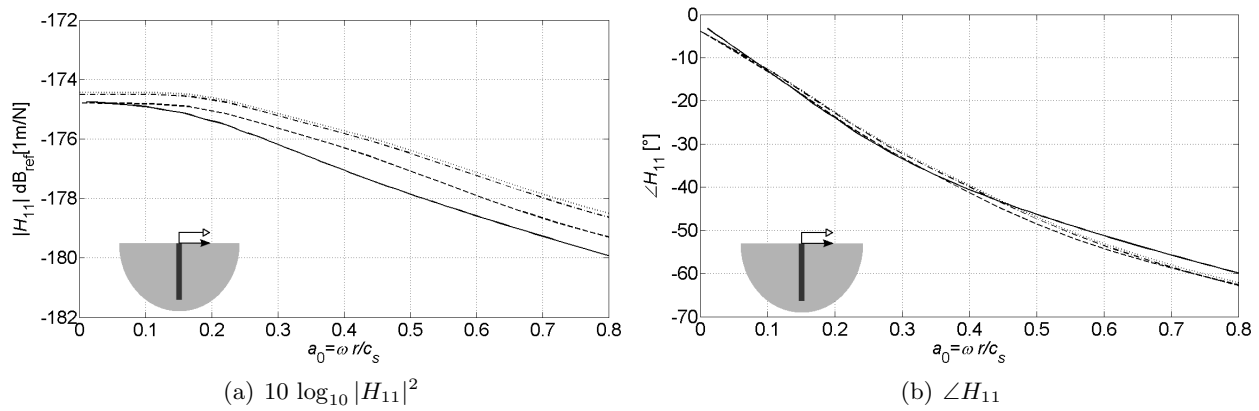


Figure 4.4: Transverse driving point FRF of a finite pile vs. dimensionless frequency a_0 , as computed using configuration 1 (dotted line), configuration 2 (dash-dot line), configuration 3 (dashed line) and the PiP model for piles (solid line).

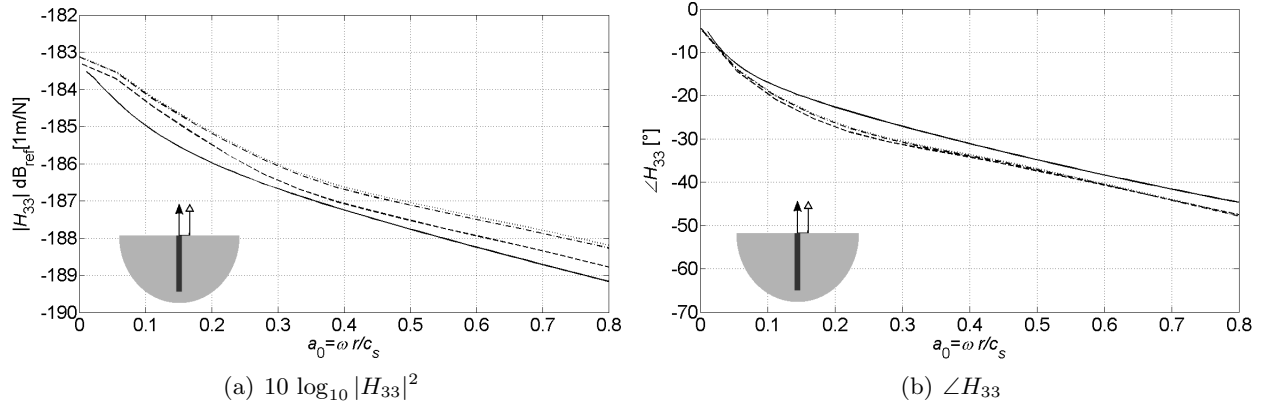


Figure 4.5: Longitudinal driving point FRF of a finite pile vs. dimensionless frequency a_0 , as computed using configuration 1 (dotted line), configuration 2 (dash-dot line), configuration 3 (dashed line) and the PiP model for piles (solid line).

4.4 Conclusion

In this chapter, the PiP model for piles is found to be in good agreement with the BE pile model, for the particular set of parameters under consideration. As well for an infinite pile in a full-space as a finite pile in a half-space, the driving point FRFs calculated with both models match very well. As the PiP model for piles is computationally very efficient, it offers great perspectives to be used as an engineering tool.

Chapter 5

The multiple pile BE model

Only a single pile has been considered in the previous chapters. In the following chapter, the model is extended to multiple piles, both for the case of unconstrained piles and the case of piles coupled to a semi-infinite column. For convenience, the model will only be extensively elaborated for the case of two piles. However, there is no theoretical restriction on the number of piles which can be taken into account, and hence a foundation design consisting of four piles will be presented in section 7.6.

5.1 Two adjacent piles with unconstrained pile-heads

5.1.1 Equations

Consider two piles A and B (Figure 5.1) with different characteristics and centre-to-centre spacing s .

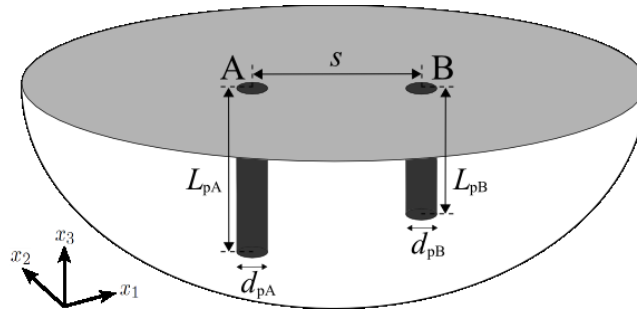


Figure 5.1: Schematic illustration of two adjacent piles.

The soil and the soil-pile interfaces are modelled using the BE method. It is reminded from section 2.1 that a constant BE formulation based on full-space Green's functions is used, with the consequence that the free surface has to be discretized. The relationship between the displacements and tractions of the N ($= N_{fs} + N_{spA} + N_{spB}$) central nodes of each element is given by Eq. (B.23) of Appendix B, and is repeated here:

$$\mathbf{Hu} = \mathbf{Gp} \tag{5.1}$$

Eq. (5.1) can be rearranged and partitioned as follows:

$$\begin{Bmatrix} \mathbf{u}_{fs} \\ \mathbf{u}_{sp}^A \\ \mathbf{u}_{sp}^B \end{Bmatrix} = \begin{bmatrix} \mathbf{H}_s^{11} & \mathbf{H}_s^{12} & \mathbf{H}_s^{13} \\ \mathbf{H}_s^{21} & \mathbf{H}_s^{22} & \mathbf{H}_s^{23} \\ \mathbf{H}_s^{31} & \mathbf{H}_s^{32} & \mathbf{H}_s^{33} \end{bmatrix} \begin{Bmatrix} \mathbf{p}_{fs} \\ \mathbf{p}_{sp}^A \\ \mathbf{p}_{sp}^B \end{Bmatrix} \quad (5.2)$$

For each of the piles, the displacements and forces are related to each other by means of the FRF matrix \mathbf{H}_p , as described in section 2.2. Timoshenko beam theory (section 3.1) is incorporated. Furthermore, compatibility of displacements and force equilibrium are assured through the matrix \mathbf{Q}_1 . The governing equations for each pile are summarized underneath.

For pile A:

$$\begin{Bmatrix} \mathbf{u}_{ph}^A \\ \mathbf{u}_p^A \end{Bmatrix} = \begin{bmatrix} \mathbf{H}_p^{A11} & \mathbf{H}_p^{A12} \\ \mathbf{H}_p^{A21} & \mathbf{H}_p^{A22} \end{bmatrix} \begin{Bmatrix} \mathbf{f}_{ph}^A \\ \mathbf{f}_p^A \end{Bmatrix} \quad (5.3)$$

$$\mathbf{u}_{sp}^A = \mathbf{Q}_1^A \mathbf{u}_p^A \quad (5.4)$$

$$\mathbf{f}_p^A = -b_p^A h_p^A \mathbf{Q}_1^{AT} \mathbf{p}_{sp}^A \quad (5.5)$$

and for pile B:

$$\begin{Bmatrix} \mathbf{u}_{ph}^B \\ \mathbf{u}_p^B \end{Bmatrix} = \begin{bmatrix} \mathbf{H}_p^{B11} & \mathbf{H}_p^{B12} \\ \mathbf{H}_p^{B21} & \mathbf{H}_p^{B22} \end{bmatrix} \begin{Bmatrix} \mathbf{f}_{ph}^B \\ \mathbf{f}_p^B \end{Bmatrix} \quad (5.6)$$

$$\mathbf{u}_{sp}^B = \mathbf{Q}_1^B \mathbf{u}_p^B \quad (5.7)$$

$$\mathbf{f}_p^B = -b_p^B h_p^B \mathbf{Q}_1^{BT} \mathbf{p}_{sp}^B \quad (5.8)$$

The second and third row of Eq. (5.2) are elaborated:

$$\mathbf{u}_{sp}^A = \mathbf{H}_s^{21} \mathbf{p}_{fs} + \mathbf{H}_s^{22} \mathbf{p}_{sp}^A + \mathbf{H}_s^{23} \mathbf{p}_{sp}^B \quad (5.9)$$

$$\mathbf{u}_{sp}^B = \mathbf{H}_s^{31} \mathbf{p}_{fs} + \mathbf{H}_s^{32} \mathbf{p}_{sp}^A + \mathbf{H}_s^{33} \mathbf{p}_{sp}^B \quad (5.10)$$

Eq. (5.10) is introduced into Eq. (5.9):

$$\mathbf{u}_{sp}^A = \mathbf{H}_s^{21} \mathbf{p}_{fs} + \mathbf{H}_s^{22} \mathbf{p}_{sp}^A + \mathbf{H}_s^{23} [\mathbf{H}_s^{33}]^{-1} (\mathbf{u}_{sp}^B - \mathbf{H}_s^{31} \mathbf{p}_{fs} - \mathbf{H}_s^{32} \mathbf{p}_{sp}^A) \quad (5.11)$$

Eq. (5.11) can be rearranged as follows:

$$\underbrace{\left(\mathbf{H}_s^{22} - \mathbf{H}_s^{23} [\mathbf{H}_s^{33}]^{-1} \mathbf{H}_s^{32} \right)}_{[\mathbf{A}]} \mathbf{p}_{sp}^A = \left(\mathbf{u}_{sp}^A - \mathbf{H}_s^{21} \mathbf{p}_{fs} - \mathbf{H}_s^{23} [\mathbf{H}_s^{33}]^{-1} (\mathbf{u}_{sp}^B - \mathbf{H}_s^{31} \mathbf{p}_{fs}) \right) \quad (5.12)$$

Finally, an expression for \mathbf{p}_{sp}^A in function of \mathbf{u}_p^A , \mathbf{u}_p^B and \mathbf{p}_{fs} is obtained:

$$\mathbf{p}_{sp}^A = [\mathbf{A}]^{-1} \left(\mathbf{Q}_1^A \mathbf{u}_p^A - \mathbf{H}_s^{23} [\mathbf{H}_s^{33}]^{-1} \mathbf{Q}_1^B \mathbf{u}_p^B - (\mathbf{H}_s^{21} - \mathbf{H}_s^{23} [\mathbf{H}_s^{33}]^{-1} \mathbf{H}_s^{31}) \mathbf{p}_{fs} \right) \quad (5.13)$$

Furthermore, the second row of Eq. (5.3) is elaborated:

$$\mathbf{u}_p^A = \mathbf{H}_p^{A21} \mathbf{f}_{ph}^A + \mathbf{H}_p^{A22} \mathbf{f}_p^A \quad (5.14)$$

Expression (5.5) for \mathbf{f}_p^A is introduced:

$$\mathbf{u}_p^A = \mathbf{H}_p^{A21} \mathbf{f}_{ph}^A - b_p^A h_p^A \mathbf{H}_p^{A22} \mathbf{Q}_1^A \mathbf{p}_{sp}^A \quad (5.15)$$

Subsequently, Eq. (5.13) is incorporated:

$$\begin{aligned} \mathbf{u}_p^A &= \mathbf{H}_p^{A21} \mathbf{f}_{ph}^A \dots \\ &\quad - b_p^A h_p^A \mathbf{H}_p^{A22} \mathbf{Q}_1^A \mathbf{T} [\mathbf{A}]^{-1} \left(\mathbf{Q}_1^A \mathbf{u}_p^A - \mathbf{H}_s^{23} [\mathbf{H}_s^{33}]^{-1} \mathbf{Q}_1^B \mathbf{u}_p^B - \left(\mathbf{H}_s^{21} - \mathbf{H}_s^{23} [\mathbf{H}_s^{33}]^{-1} \mathbf{H}_s^{31} \right) \mathbf{p}_{fs} \right) \end{aligned} \quad (5.16)$$

Eq. (5.16) can be rearranged as follows:

$$\begin{aligned} \underbrace{\left(\mathbf{I} + b_p^A h_p^A \mathbf{H}_p^{A22} \mathbf{Q}_1^A \mathbf{T} [\mathbf{A}]^{-1} \mathbf{Q}_1^A \right)}_{[\mathbf{C}]} \mathbf{u}_p^A &= \mathbf{H}_p^{A21} \mathbf{f}_{ph}^A \dots \\ &\quad + b_p^A h_p^A \mathbf{H}_p^{A22} \mathbf{Q}_1^A \mathbf{T} [\mathbf{A}]^{-1} \left(\mathbf{H}_s^{23} [\mathbf{H}_s^{33}]^{-1} \mathbf{Q}_1^B \mathbf{u}_p^B + \left(\mathbf{H}_s^{21} - \mathbf{H}_s^{23} [\mathbf{H}_s^{33}]^{-1} \mathbf{H}_s^{31} \right) \mathbf{p}_{fs} \right) \end{aligned} \quad (5.17)$$

Eventually, an expression for \mathbf{u}_p^A in function of \mathbf{f}_{ph}^A , \mathbf{u}_p^B and \mathbf{p}_{fs} is obtained:

$$\begin{aligned} \mathbf{u}_p^A &= [\mathbf{C}]^{-1} \mathbf{H}_p^{A21} \mathbf{f}_{ph}^A \dots \\ &\quad + b_p^A h_p^A [\mathbf{C}]^{-1} \mathbf{H}_p^{A22} \mathbf{Q}_1^A \mathbf{T} [\mathbf{A}]^{-1} \left(\mathbf{H}_s^{23} [\mathbf{H}_s^{33}]^{-1} \mathbf{Q}_1^B \mathbf{u}_p^B + \left(\mathbf{H}_s^{21} - \mathbf{H}_s^{23} [\mathbf{H}_s^{33}]^{-1} \mathbf{H}_s^{31} \right) \mathbf{p}_{fs} \right) \end{aligned} \quad (5.18)$$

One can find in a similar way an analogous expression for \mathbf{u}_p^B :

$$\begin{aligned} \mathbf{u}_p^B &= [\mathbf{D}]^{-1} \mathbf{H}_p^{B21} \mathbf{f}_{ph}^B \dots \\ &\quad + b_p^B h_p^B [\mathbf{D}]^{-1} \mathbf{H}_p^{B22} \mathbf{Q}_1^B \mathbf{T} [\mathbf{B}]^{-1} \left(\mathbf{H}_s^{32} [\mathbf{H}_s^{22}]^{-1} \mathbf{Q}_1^A \mathbf{u}_p^A + \left(\mathbf{H}_s^{31} - \mathbf{H}_s^{32} [\mathbf{H}_s^{22}]^{-1} \mathbf{H}_s^{21} \right) \mathbf{p}_{fs} \right) \end{aligned} \quad (5.19)$$

with $[\mathbf{B}]$ and $[\mathbf{D}]$ being analogous to the matrices $[\mathbf{A}]$ respectively $[\mathbf{C}]$.

Combining Eq. (5.18) and Eq. (5.19) results finally in expressions for the pile displacements \mathbf{u}_p^A and \mathbf{u}_p^B in function of the different possible loads \mathbf{f}_{ph}^A , \mathbf{f}_{ph}^B and \mathbf{p}_{fs} :

$$\mathbf{u}_p^A = [\mathbf{E}]^{-1} [\mathbf{F}] \mathbf{f}_{ph}^A + [\mathbf{E}]^{-1} [\mathbf{G}] \mathbf{f}_{ph}^B + [\mathbf{E}]^{-1} [\mathbf{X}] \mathbf{p}_{fs} \quad (5.20)$$

$$\mathbf{u}_p^B = [\mathbf{H}]^{-1} [\mathbf{I}] \mathbf{f}_{ph}^A + [\mathbf{H}]^{-1} [\mathbf{J}] \mathbf{f}_{ph}^B + [\mathbf{H}]^{-1} [\mathbf{Y}] \mathbf{p}_{fs} \quad (5.21)$$

The expressions for the matrices $[\mathbf{E}]$, $[\mathbf{F}]$, $[\mathbf{G}]$ and $[\mathbf{X}]$ (as well as for $[\mathbf{H}]$, $[\mathbf{I}]$, $[\mathbf{J}]$ and $[\mathbf{Y}]$) are rather lengthy, and therefore, they are summarized in Appendix E.1.

5.1.2 Validation

Before the multiple pile model can be used, it needs to be validated. A validation is carried out in terms of dynamic interaction factors α_{ij} . These are defined by Eq. (5.22):

$$\alpha_{ij} = \frac{\text{Displacement } i \text{ of pile-head B due to load } j \text{ applied to pile-head A}}{\text{Static displacement } i \text{ of pile-head A due to load } j \text{ applied to pile-head A}} \quad (5.22)$$

A comparison is made with the values of α_{ij} obtained by Kaynia [24], which is regarded as one of the main references in literature. The validation is carried out for two identical piles with a centre-to-centre spacing $s = 1.50$ m. The soil and pile parameters are summarized in Table 5.1. Nine interaction factors are calculated, and this is done for three different configurations of the BE pile model (Table 5.2).

Parameter	Soil	Piles
E [Pa]	280×10^6	280×10^9
ν [-]	0.40	0.25
μ [Pa]	100×10^6	112×10^9
λ [Pa]	600×10^6	112×10^9
ρ [kg/m ³]	2000	2857
β_μ [-]	0.025	0
β_λ [-]	0.025	0
c_s [m/s]	223.6	6261
c_p [m/s]	547.7	10844
L [m]	–	10.5
d [m]	–	$1/\sqrt{2}$

Table 5.1: Soil and pile parameters used in the validation of the multiple pile model.

Configuration	Cross-section	b_p [m]	h_p [m]	b_1 [m]	b_2 [m]
1	square	0.50	0.50	0.50	0.50
2	square	0.25	0.25	0.25	0.25
3	octagonal	$\frac{\cos \frac{3\pi}{8}}{\sqrt{2}} \simeq 0.27$	0.25	0.25	0.25

Table 5.2: Parameters of the three BE pile model configurations used in the validation of the multiple pile model.

Figure 5.2 compares the nine interaction factors of the two different models. Note that Kaynia's results are only available till $a_0 = 0.5$. Nevertheless, results of the current model are plotted up till $a_0 = 0.8$ in

order to check if any anomaly arises. It can be concluded from Figure 5.2 that the agreement between the results obtained by Kaynia and those obtained with the current BE model is satisfying. It is clear that a model with a square approximation of the pile-soil interface and a relatively coarse mesh already gives an acceptable accuracy. Furthermore, the reciprocity relationships $\alpha_{\theta_1 f_2} = \alpha_{u_2 m_1}$ and $\alpha_{\theta_2 f_1} = \alpha_{u_1 m_2}$ are fulfilled (it is believed that the small distortions are caused by numerical errors).

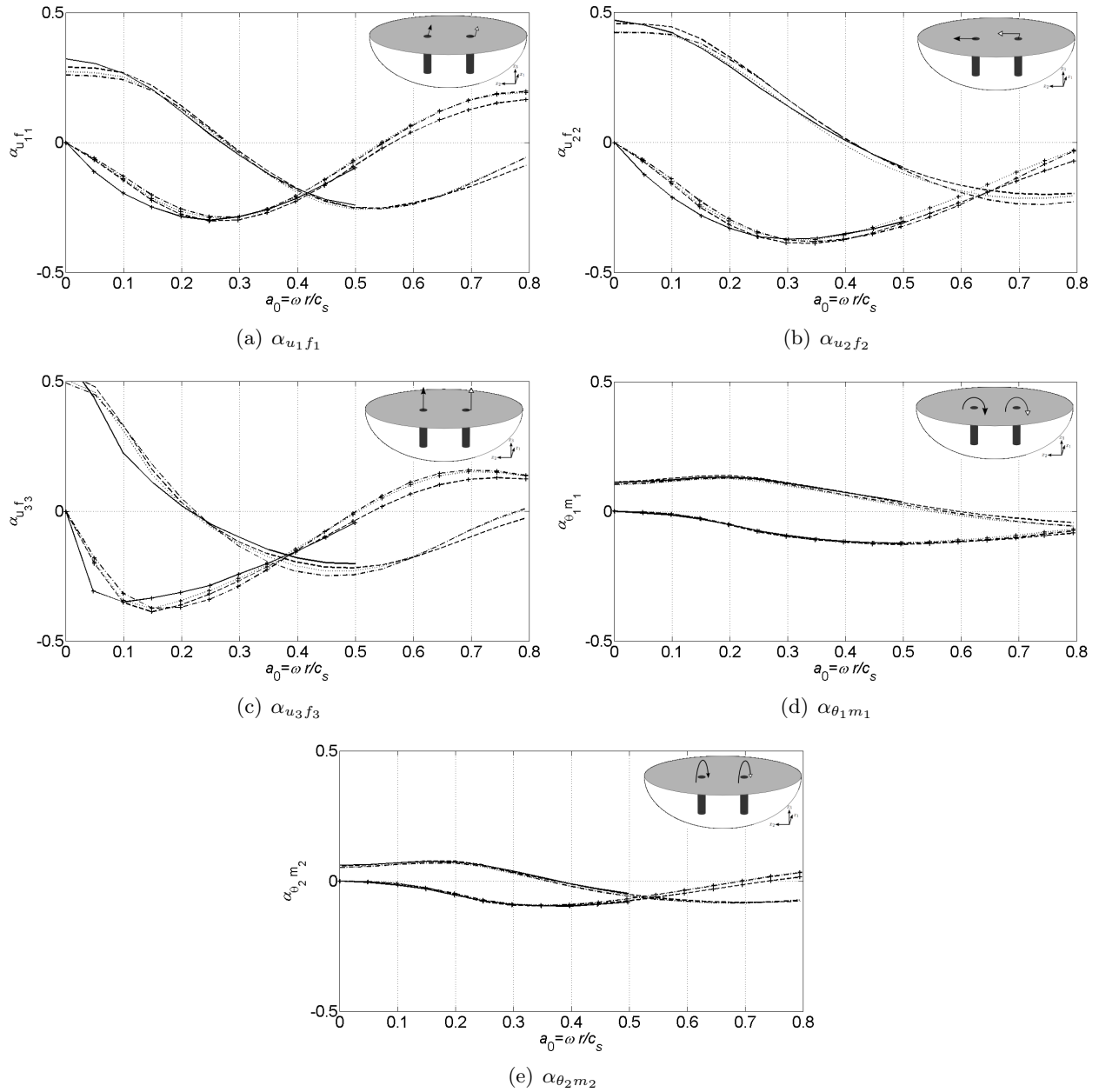


Figure 5.2 continues over page.

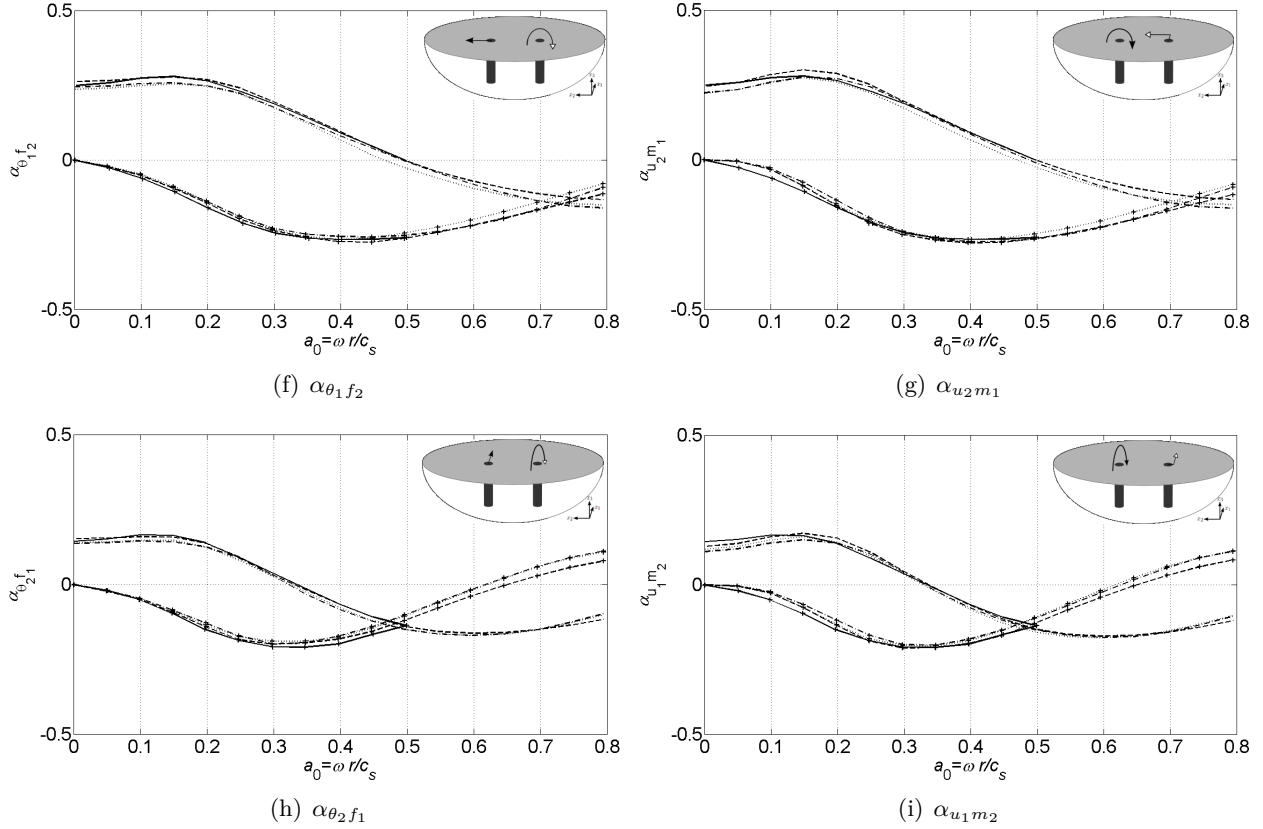


Figure 5.2: Dynamic interaction factors α_{ij} vs. dimensionless frequency a_0 , as computed using configuration 1 (dotted line), configuration 2 (dash-dot line), configuration 3 (dashed line) and Kaynia's model (solid line). The real parts $\Re(\alpha_{ij})$ are given as plain lines, while the imaginary parts $\Im(\alpha_{ij})$ are marked by crosses.

The validation results of Figure 5.2 can be extended to cases with different pile separation distances s . Meanwhile, a comparison with the PiP model for piles is made. It is important to note that in the PiP model for piles, uncoupling of source (first pile) and receiver (second pile) is assumed in order to calculate the interaction factors, while the pile-soil-pile interactions are inherently accounted for in the BE pile model. Hence, one can expect good agreement of the models when the distance separating the source and the receiver is large compared with the longest wavelength in the soil [28].

Figure 5.3 compares some results of the current BE model with those obtained by Kaynia and the PiP model for piles, for three different pile separation distances: $s = 2 d_p$, $s = 5 d_p$ and $s = 10 d_p$, with d_p the pile diameter. The soil and pile parameters remain the same as in the calculations above. Again, the agreement between the BE model and the results of Kaynia is seen to be very good. The agreement between the PiP model for piles and the results of the BE model improves with increasing pile separation distance. As expected, this indicates that the uncoupled source-receiver model of PiP for piles is an unsuitable assumption at small separation distances. Further inaccuracies in the interaction factors calculated using the PiP model for piles arise from the use of the mirror-image method (section 4.1). This is because the mirror-image method does not produce a stress field which

completely satisfies the traction-free boundary conditions at the free surface [28]. In spite of these inaccuracies, the PiP model for piles offers great improvement in computation times with an under-a-second run time compared to the BE model, which has a run-time in the order of minutes to hours.

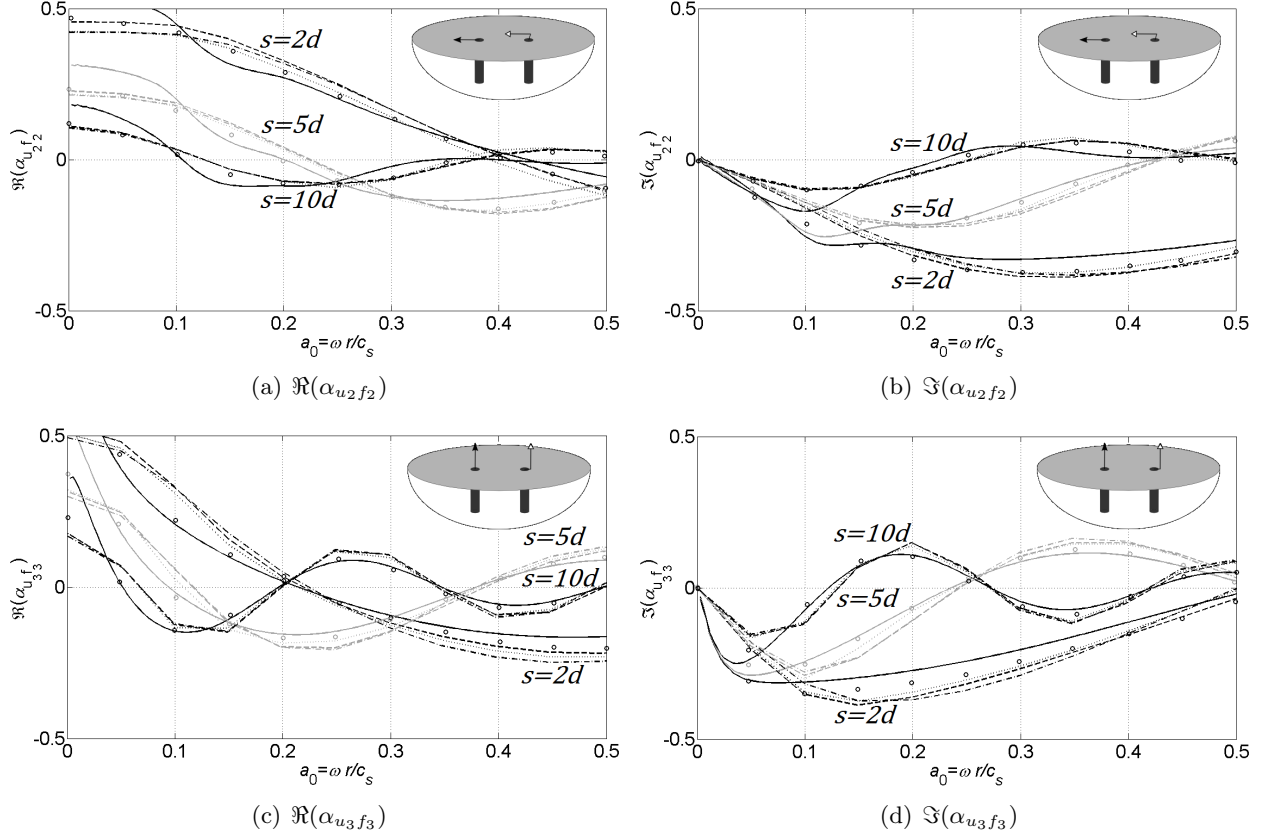
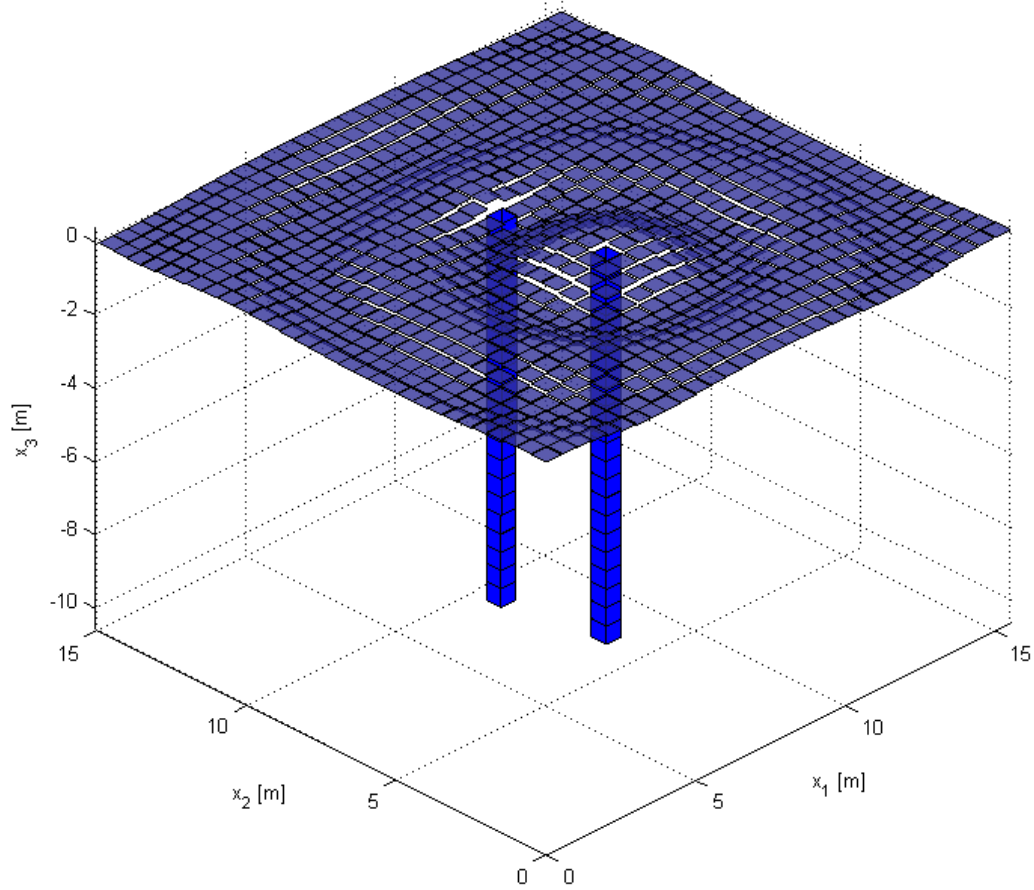


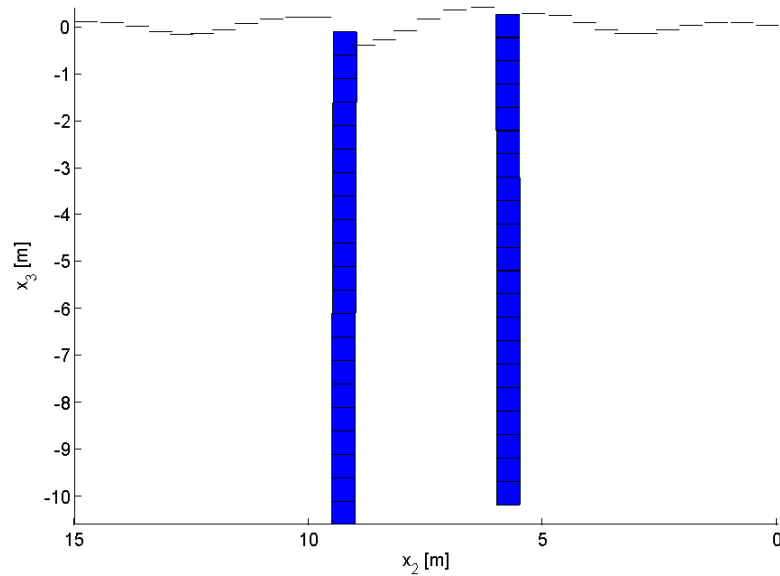
Figure 5.3: Real and imaginary parts of the dynamic interaction factors α_{ij} vs. dimensionless frequency a_0 , as computed using configuration 1 (dotted line), configuration 2 (dash-dot line), configuration 3 (dashed line), the PiP model for piles (solid line) and Kaynia's model (circles). The different pile separation distances s are marked on the figures.

5.1.3 Illustration

Figure 5.4 shows the response of two piles to a unit vertical load applied at pile-head A with coordinates $\{8, 5.75, 0\}^T$, at 50 Hz. The BE mesh is characterized by the following parameters: $N_1 = 31$, $N_2 = 30$ and $b_1 = b_2 = b_p = h_p = 0.50$ m. The latter ensures that the recommendation by Dominguez [13] that at least six constant elements per wavelength should be used is fulfilled. From Figure 5.4(a), it is clear that circular wavefronts arise concentric to the loaded pile. Furthermore, Figure 5.4(b) reveals a phase lag between the response of the loaded and the unloaded pile, caused by the inertial mass of the piles.



(a) Three-dimensional view.



(b) Vertical cross-section through the free surface and the piles at the location of the pile centroids.

Figure 5.4: Displacement field (multiplied with a factor 2×10^9) predicted by the multiple pile BE model due to a unit vertical load applied at pile-head A, at 50 Hz.

A power flow analysis can be performed to investigate the interaction between the two piles. It is based on the principles introduced in section 3.2. Figure 5.5 illustrates a case in which only a unit horizontal load \mathbf{p}_{fs} is applied to the free surface. This load is collinear with the piles and is located at a distance $R = 1.5$ m from the first pile (pile A), while the centre-to-centre spacing s between the piles equals 2 m. Zero pile damping is assumed to check the conservation of energy: as there is no power input at the pile-head, the sum of the power entering the pile has to be equal to the sum of the power leaving the pile. It is clear from Figure 5.5(a) that this holds for both piles. The power flow distribution is shown in Figure 5.5(b) at 25 Hz. It can be noticed that power enters the upper left-hand side of the first pile, from where it partly flows through the upper right-hand side and partly downwards along the pile's central axis. Power is radiated through both the lower left-and right-hand sides of the first pile, as well as through the pile-tip. It enters the second pile along the entire left-hand side (although this is not very clear from the figure). Eventually, the power follows a path through the second pile similar to the one through the first pile.

It is noticeable that the amount of power flowing through the second pile is significantly less than through the first one. The reason for this is obvious, because the former is lying behind the latter. The magnitude of this (geometric) shadow effect will be quantified in chapter 6.

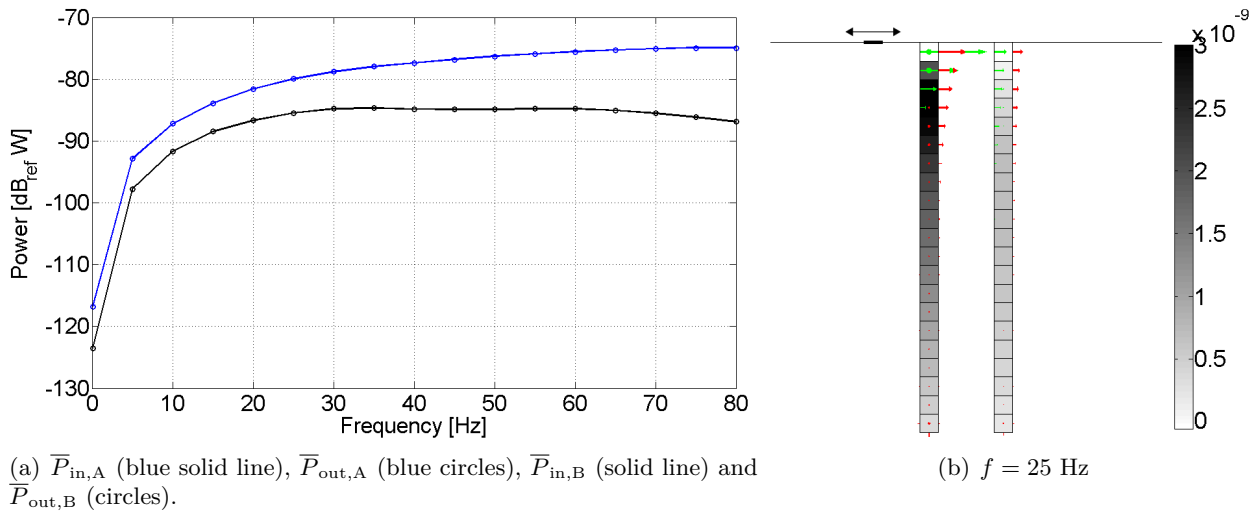


Figure 5.5: Power flow analysis for a prescribed horizontal traction \mathbf{p}_{fs} collinear with the piles. The load is located at a distance $R = 1.50$ m from pile-head A, while the centre-to-centre spacing s between the piles equals 2 m. Figure (a) clearly demonstrates the conservation of energy. The power flow distribution at 25 Hz is illustrated in (b).

5.2 Two adjacent piles with semi-infinite columns

5.2.1 Equations

Adding semi-infinite columns on top of each pile (potentially with base isolation) results in two extra equations, as mentioned in section 3.3:

$$\mathbf{u}_{\text{ph}}^{\text{A}} = -\mathbf{H}_{\text{b}}^{\text{A}} \mathbf{f}_{\text{ph}}^{\text{A}} \quad (5.23)$$

$$\mathbf{u}_{\text{ph}}^{\text{B}} = -\mathbf{H}_{\text{b}}^{\text{B}} \mathbf{f}_{\text{ph}}^{\text{B}} \quad (5.24)$$

Eq. (3.69) gives the general expression for \mathbf{H}_{b} . In a very similar way as in paragraph 5.1.1, Eqs. (5.23)–(5.24) can be combined with Eqs. (5.2)–(5.8) to obtain an expression for the pile displacements $\mathbf{u}_{\text{p}}^{\text{A}}$ and $\mathbf{u}_{\text{p}}^{\text{B}}$ in function of \mathbf{p}_{fs} :

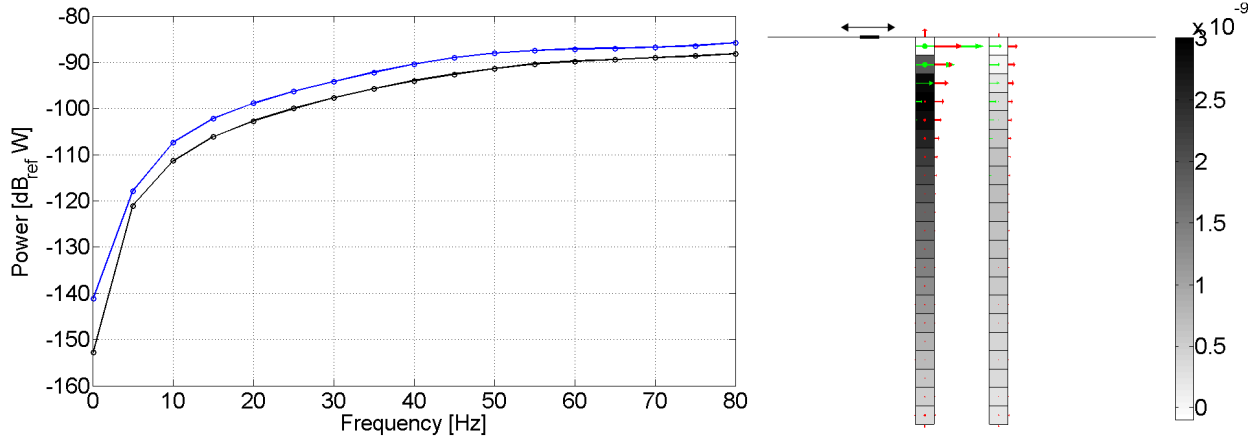
$$\mathbf{u}_{\text{p}}^{\text{A}} = [\mathbf{T}_{\text{A}}]^{-1} \mathbf{U}_{\text{A}} \mathbf{p}_{\text{fs}} \quad (5.25)$$

$$\mathbf{u}_{\text{p}}^{\text{B}} = [\mathbf{T}_{\text{B}}]^{-1} \mathbf{U}_{\text{B}} \mathbf{p}_{\text{fs}} \quad (5.26)$$

Expressions for the matrices \mathbf{T}_{A} , \mathbf{U}_{A} , \mathbf{T}_{B} and \mathbf{U}_{B} are given in Appendix E.2.

5.2.2 Illustration

The effect of incorporating the semi-infinite columns can again be illustrated by means of a power flow analysis (Figure 5.6). The same conditions as in paragraph 5.1.3 are valid. Figure 5.6(a) illustrates the conservation of energy for each pile. The power flow distribution at 25 Hz is shown in Figure 5.6(b). Again, it is important to note that the scale of the pile body shading extends to a negative value. Based on the convention put forward in section 3.2, a negative value represents an upstream power flow. In contrast to Figure 5.5(b), there is also power flowing upwards through the pile-heads into the semi-infinite columns.



(a) $\bar{P}_{in,A}$ (blue solid line), $\bar{P}_{out,A}$ (blue circles), $\bar{P}_{in,B}$ (solid line) and $\bar{P}_{out,B}$ (circles).

(b) $f = 25$ Hz

Figure 5.6: Power flow analysis for a prescribed horizontal traction \mathbf{p}_{fs} collinear with the piles. The load is located at a distance $R = 1.50$ m from pile-head A, while the centre-to-centre spacing s between the piles equals 2 m. A simplistic building model is incorporated in the model. Figure (a) clearly demonstrates the conservation of energy. The power flow distribution at 25 Hz is illustrated in (b).

5.3 Conclusion

In this chapter, a multiple pile BE model has been introduced. The pile-soil-pile interactions are inherently accounted for by means of the BE equations. The model has been validated in terms of dynamic interaction factors; good agreement between the BE model and the results of Kaynia is found. The validated multiple pile BE model will be used throughout the following chapters.

Chapter 6

The shadow effect

6.1 Introduction

The multiple pile BE model developed in chapter 5 can now be used to assess the influence of the presence of a pile on the dynamic response of an adjacent pile. One can expect this effect to be strongly dependent on the relative positions of the piles compared to the position of the load applied. Therefore, the situation of Figure 6.1 is compared to the one of Figure 6.2. In both cases, a load \mathbf{p}_{fs} is applied on the free surface of the half-space. In case of Figure 6.2, it could be stated that the original pile stands in the shadow of the second pile. It is expected that the magnitude of this so-called shadow effect depends on the angle β between the original pile and the load applied. The quantitative effect will be investigated in the following sections.

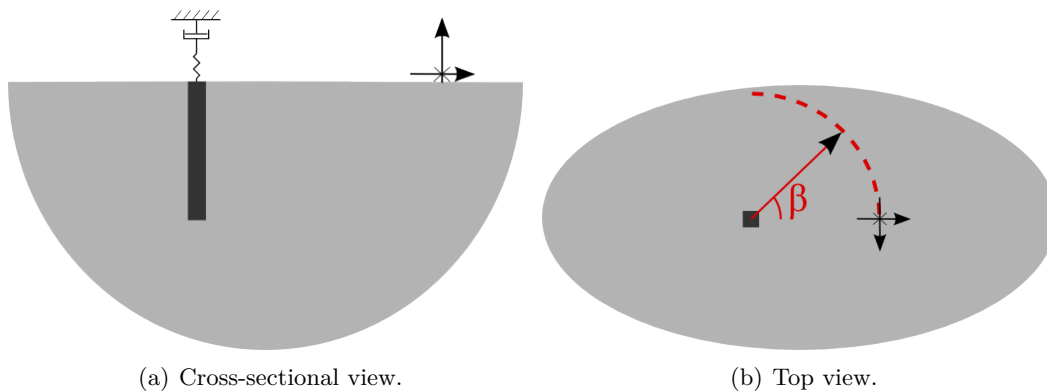


Figure 6.1: Single pile.

6.2 Models

The shadow effect will be assessed in terms of power flowing into the semi-infinite column (or equivalent viscous damper) on top of the original pile. In case of Figure 6.1, the response of the pile is calculated

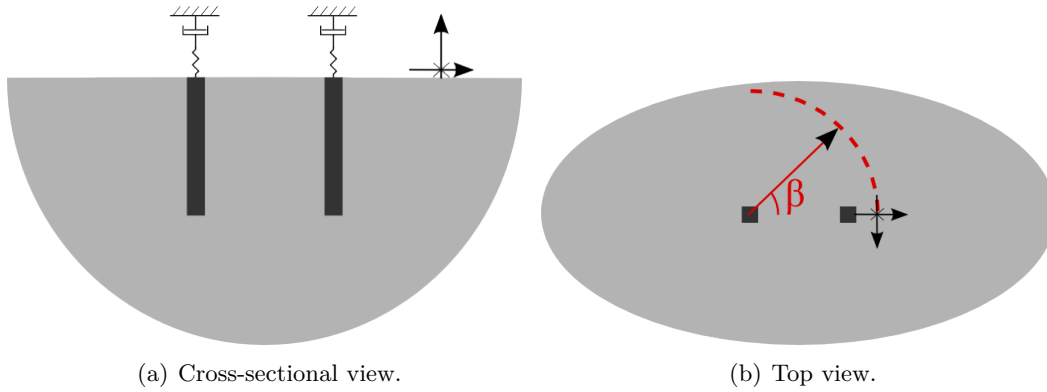


Figure 6.2: Pile in the shadow of another one.

by means of Eq. (3.61), and the power flow subsequently through Eq. (3.62). Eqs. (5.25) and (3.62) are used to obtain the power flow in case of Figure 6.2.

In order to limit the computation time, the pile-soil circumference is approximated by means of a square cross-section, and a coarse BE mesh is used (i.e. configuration 1 of Table 5.2). The centre-to-centre spacing s between the piles equals 2 m, and the mean distance between the load \mathbf{p}_{fs} applied to the free surface and the original pile is 3.50 m. The soil and pile parameters summarized in Table 5.1 are also used throughout this chapter.

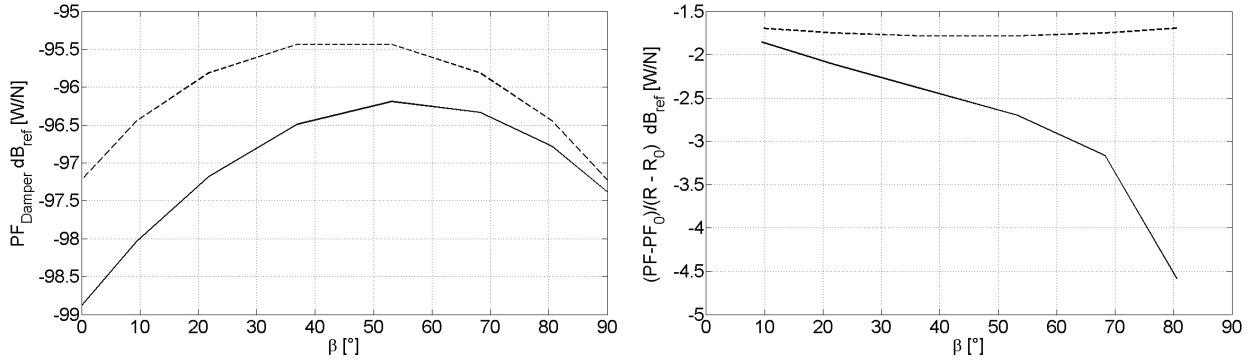
6.3 Results

The results will be presented for a unit vertical load applied to the free surface; similar results have been obtained in case of horizontal loads.

6.3.1 Vertical point load at 25 Hz

Consider a vertical point load at 25 Hz applied to the free surface. The position of the load is described by the angle β , which is varied from 0° to 90° . The power flowing into the damper of the original pile is shown in Figure 6.3(a), and this for both cases. The shadow effect is clearly visible.

The fact that the PF varies in function of β in case of a single pile can be attributed to the non-constant distance between pile and load. As a specific element of the free surface has to be chosen to apply the load, it is impossible to describe exactly an arc of a circle (unlike the conceptual representation in Figure 6.1). This statement is supported by Figure 6.3(b), which gives the ratio of the difference in power flow ΔPF to the difference in pile-load distance ΔR , as a function of the angle β . The differences ΔPF and ΔR are made to the PF_0 and R_0 , i.e. the power flow and the pile-load distance where $\beta = 0^\circ$. For the original pile, it is clear that this ratio is almost constant for all values of β . It is believed that the small deviation from a constant value is caused by the coarseness of the BE model. Furthermore, this figure illustrates once more the variation of power flow in the shadowed pile as a function of β .



(a) Power flow in a single pile (dashed line) and a shadowed pile (solid line) vs. angle β . (b) Relative variation of power flow in a single pile (dashed line) and a shadowed pile (solid line) vs. angle β .

Figure 6.3: Shadow effect for a unit vertical load at 25 Hz.

The power flow insertion gain (PFIG) due to the presence of an extra pile is defined by Eq. (6.1) and is plotted in Figure 6.4:

$$\text{PFIG} = 10 \log_{10} \left(\frac{\overline{P}_{\text{damper},2p}}{\overline{P}_{\text{damper},1p}} \right) \quad (6.1)$$

A quasi linear relationship between the PFIG and the angle β can be observed, varying from -1.5 dB when the load is placed in a line with the two piles, i.e. $\beta = 0^\circ$, to almost 0 dB when the load is located perpendicular to the connection line of the two piles, i.e. $\beta = 90^\circ$.

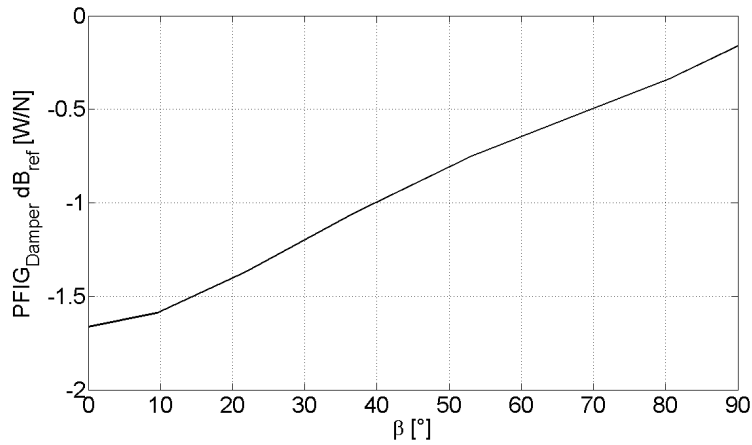


Figure 6.4: Power flow insertion gain vs. angle β , for a unit vertical load at 25 Hz.

6.3.2 Vertical point load at frequencies up to 80 Hz

The calculations presented in paragraph 6.3.1 can be generalized to a broad range of frequencies. The results of such an analysis are presented in Figure 6.5 as a contourplot. For frequencies up to 50 Hz, the same pattern as in Figure 6.4 can be observed: the PFIG varies almost linearly from -1.5 dB where $\beta = 0^\circ$ to 0 dB where $\beta = 90^\circ$. However, from ~ 50 Hz onwards, a positive PFIG can be noticed: adding an extra pile causes more power to flow into the viscous damper on top of the original pile.

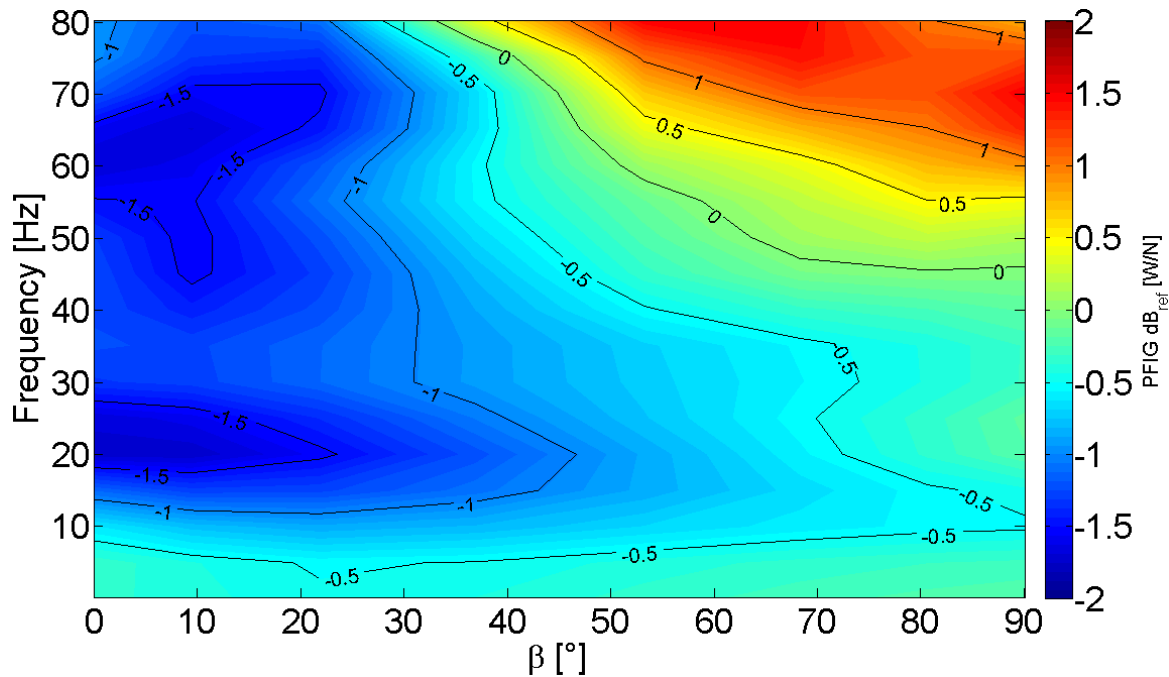


Figure 6.5: Power flow insertion gain as a function of angle β and frequency f , for a unit vertical load.

In an attempt to find a plausible explanation for this phenomenon, consider the situation where $\beta = 90^\circ$ (Figure 6.6). Figures 6.7(a) and 6.7(b)¹ illustrate the power flow distribution around the pile-heads in case of a single pile respectively a shadowed pile, at $f = 25$ Hz. In this case, adding an extra pile has negligible influence on the PF distribution around the original pile. However, when the PF distribution is investigated at $f = 75$ Hz (Figure 6.8), one can clearly see that there is an increase in PF into the damper of the original pile, and this mainly originates from power flowing through the face of the pile skin orientated to the extra pile. Therefore, it is clear that this increase in PF is caused by some kind of wave scattering: from a certain frequency onwards, the wavelength becomes equal or less than the distance between the excitation point and the extra pile, and the waves start to diffract. This causes extra power to flow through the skin of the original pile, and hence into its damper.

¹Again, it is emphasized that the arrows do not represent a vector quantity, but they indicate the difference between power flowing inwards and power flowing outwards.

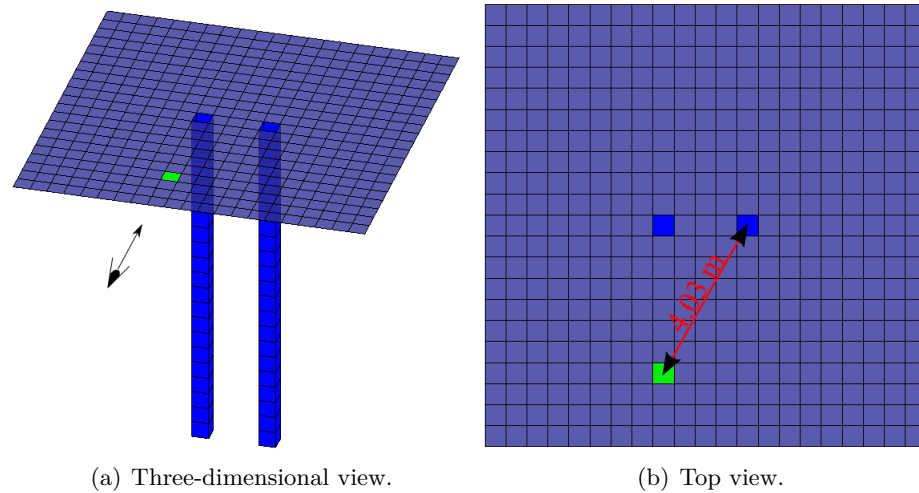


Figure 6.6: Two adjacent piles with centre-to-centre spacing $s = 2$ m. A unit vertical load is applied at a location characterized by $R = 3.50$ m and $\beta = 90^\circ$.

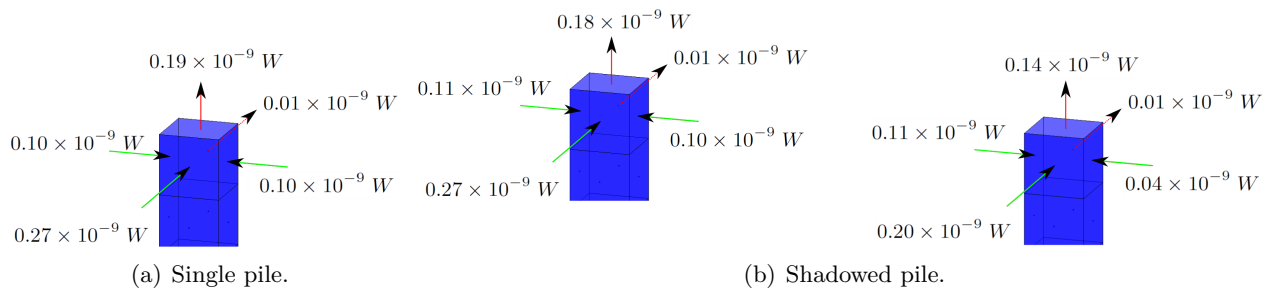


Figure 6.7: Power flow distribution around the pile-heads of (a) the original single pile and (b) the shadowed pile, due to a unit vertical load at 25 Hz, applied at a location characterized by $R = 3.50$ m and $\beta = 90^\circ$.

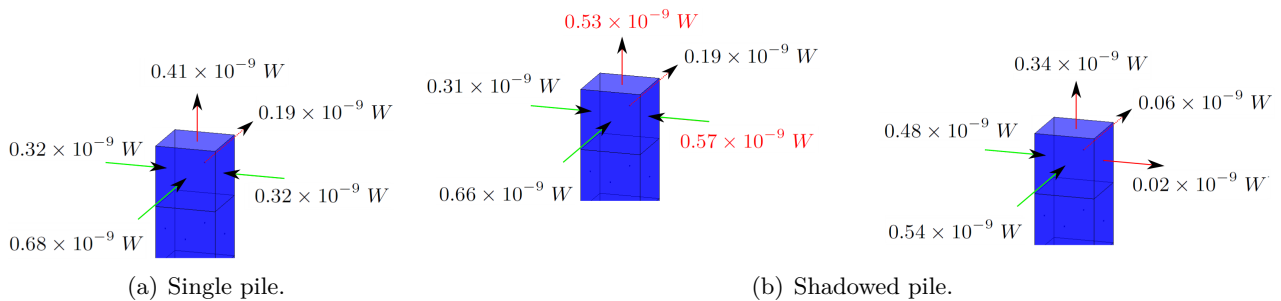


Figure 6.8: Power flow distribution around the pile-heads of (a) the original single pile and (b) the shadowed pile, due to a unit vertical load at 75 Hz, applied at a location characterized by $R = 3.50$ m and $\beta = 90^\circ$.

The frequency at which one expects this phenomenon to start can be estimated based on the distance ΔL between the excitation point and the extra pile, and the Rayleigh wave speed. ΔL can be obtained from Figure 6.6(b), for the particular case under consideration: $\Delta L = \sqrt{s^2 + R^2} \simeq 4.03$ m. Based on the values in Table 5.1 and the formula presented in [47], the Rayleigh wave speed c_R equals 211.6 m/s. The frequency at which the wavelength λ equals ΔL can easily be obtained from the dispersion relation:

$$c_R = \lambda f \quad (6.2)$$

$$\Rightarrow f = \frac{c_R}{\Delta L} \quad (6.3)$$

Hence, introducing the values for ΔL and c_R gives:

$$f = \frac{211.6 \text{ m/s}}{4.03 \text{ m}} \quad (6.4)$$

$$= 52.5 \text{ Hz} \quad (6.5)$$

The value obtained in Eq. (6.5) matches well with the frequency observed in Figure 6.5 at which the PFIG starts to become positive (for $\beta = 90^\circ$). For other values of β , similar calculations can be done to obtain the frequency at which one expects wave scattering to start.

6.4 Conclusion

Investigation of the shadow effect has revealed a quasi linear relationship between the PFIG and the relative position of the load, at relatively low frequencies. However, when the wavelengths approach the distance between piles and load, there is a tendency to wave scattering. One needs to bear these results in mind when using the superposition of interaction factors to model the pile-soil-pile interactions. If an uncoupled source-receiver approach is used to account for PSPI, such as in the PiP model for piles, this tendency to wave scattering might not be modelled correctly. Hence, it could be necessary to include some extra factor to take this phenomenon into account.

Chapter 7

The response of piled foundations to underground railway induced loadings

In the previous chapters, only inertial loadings have been considered. It is the aim to investigate in this chapter the response of piled foundations to a realistic source of vibrations, i.e. an underground railway.

Throughout this chapter, the coupling between source (underground railway) and receiver (piled foundations) will be disregarded. This assumption results in a two-step approach, which can be regarded as a subdomain formulation. In the first step, the Pipe-in-Pipe model for underground railways [38] is utilized to calculate displacements and tractions in the soil due to the movement of a train in a tunnel. Throughout this step, the presence of the piles in the soil is ignored. Once the displacements and tractions are known, they are used as input variables (generalized loadings) for the second step, which consists of the BE pile model. Similar to the first step, the presence of the tunnel is neglected in the second step. The approach is illustrated in Figure 7.1.

It is important to note that the assumed uncoupling of source and receiver is an approximation of the real situation. It can only be justified if the distance between source and receiver is sufficiently large compared to the wavelength of the waves in the soil. However, in case of an urban environment, the minimum tunnel-pile distance is of the same order of magnitude as the smallest soil wavelength, in the frequency range of interest for vibration nuisance to people. Therefore, a coupled source and receiver model needs to be developed, but this is the subject of further research (chapter 8).

Section 7.1 demonstrates that the two-step approach gives acceptable results for a simple test case. The source and receiver models necessary to obtain the vibration response of piled foundations to underground railway induced loadings are summarized in section 7.2 respectively 7.3. Sections 7.4 and 7.5 present results of calculations for a single pile and a four-pile group. A comparison is made with the PiP model for piles. Eventually, the model is applied to investigate several aspects of the dynamic response of piled foundations (section 7.6).

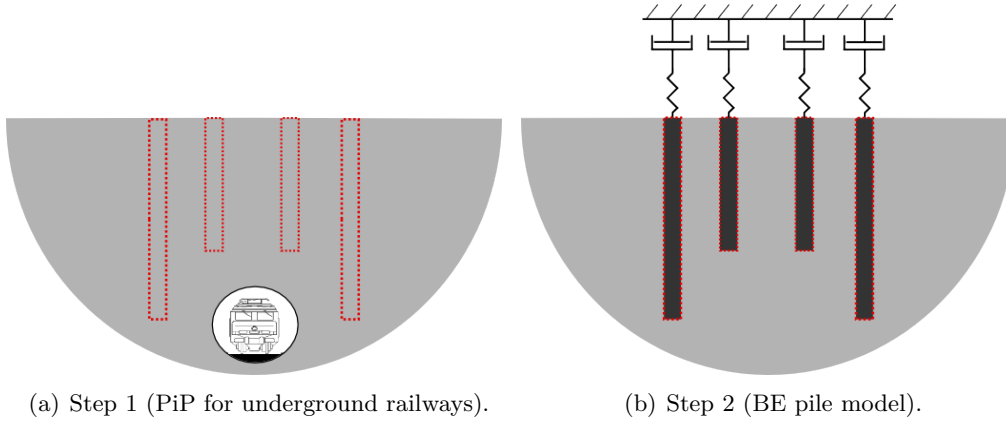


Figure 7.1: Illustration of the two-step approach used to calculate the response of piled foundations to underground railway induced vibrations. (a) The PiP model for underground railways is utilized to calculate displacements and tractions in the soil, and (b) these are applied as generalized loadings to the BE pile model.

7.1 Validation of the two-step approach (subdomain formulation)

Before proceeding with modelling the response of piled foundations to underground railway induced loadings, the proposed two-step approach should be validated in some way. Therefore, the response of a single pile to an inertial load case is calculated in two different ways. Firstly, the response is calculated straightforwardly by means of the BE model, and secondly, the two-step approach is applied.

Consider a single pile and a unit load \mathbf{p}_{fs} applied to the free surface at a distance $R = 3.50$ m from the pile-head. The soil and pile parameters are summarized in Table 5.1. The response \mathbf{u}_p of the pile can be calculated straightforwardly by means of Eq. (3.38).

In the two-step approach, displacements \mathbf{u}^{inc} and tractions \mathbf{p}^{inc} in the soil due to the unit load applied to the free surface are first determined, neglecting the presence of the pile. The superscript *inc* refers to the incident wavefield. For this purpose, the ElastoDynamics Toolbox (EDT) [41, 42] is used. This toolbox is based on the direct stiffness formulation. Displacements and tractions are computed with the function `disk3d_rec`, i.e. the solution due to a disk load. The diameter of the disk is set equal to the width of a boundary element. Finally, \mathbf{u}^{inc} and \mathbf{p}^{inc} are used as input variables in the BE model as follows:

$$\mathbf{H}(\mathbf{u} - \mathbf{u}^{inc}) = \mathbf{G}(\mathbf{p} - \mathbf{p}^{inc}) \quad (7.1)$$

Based on this equation and all other equations of the BE model, the pile response \mathbf{u}_p can be computed. More information about the subdomain formulation and the origin of Eq. (7.1) can be found in [1].

The straightforward computation and the two-step approach are compared in terms of the pile-head response \mathbf{u}_{ph} , and this for three different configurations of the loading \mathbf{p}_{fs} . The comparison is illustrated in Figure 7.2. Despite the fact that the loading is quite close to the pile ($R = 3.50$ m), it is clear that the two-step approach gives acceptable results in the frequency range considered (i.e. 0 – 80 Hz). Therefore, it can be expected that the two-step model will give satisfying results when the response

of piled foundations to underground railway induced loadings is calculated. This is the subject of following sections.

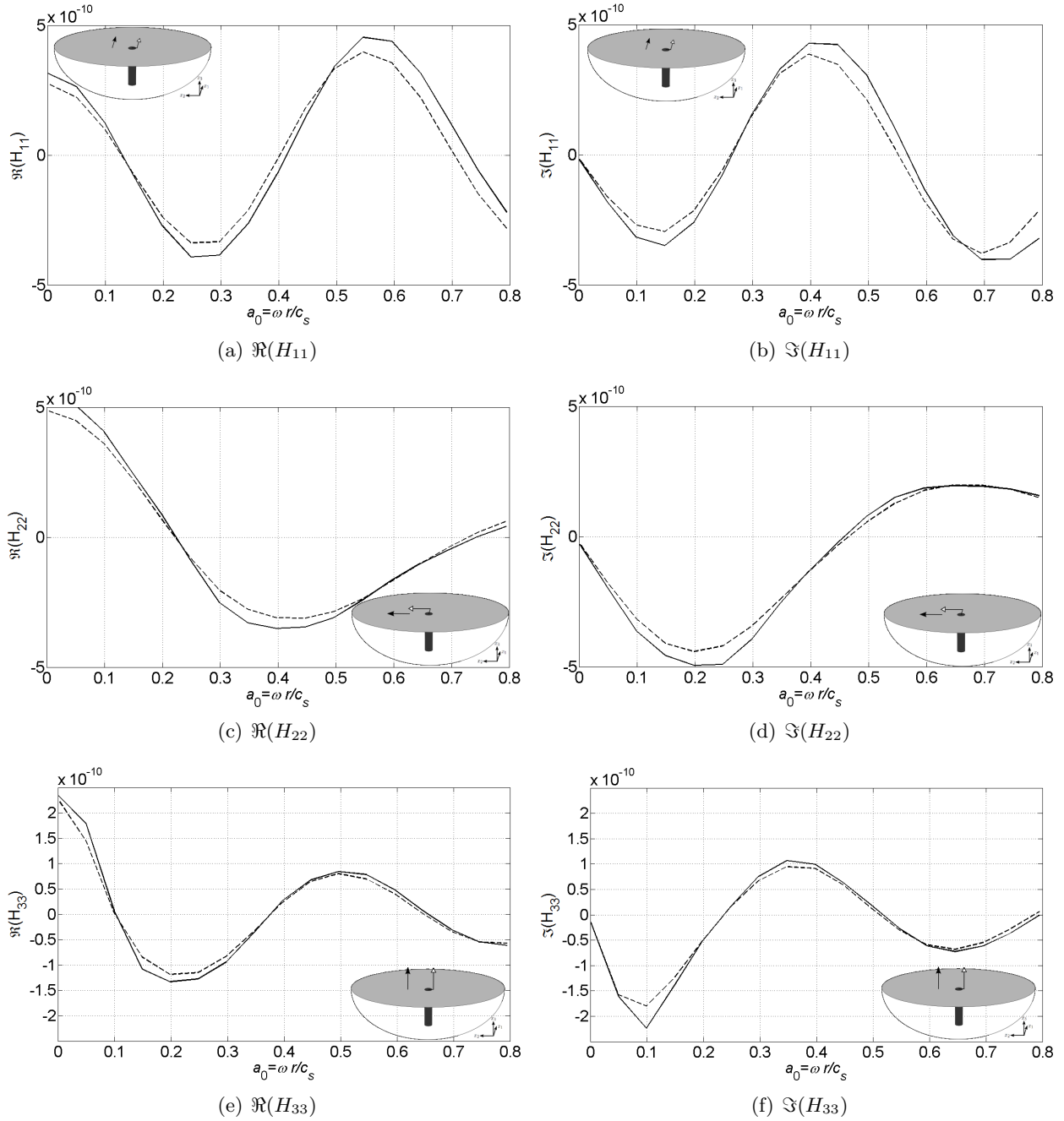


Figure 7.2: Real and imaginary parts of the pile-head responses H_{ii} vs. dimensionless frequency a_0 , as computed straightforwardly (solid line) and using the subdomain formulation (dashed line).

7.2 The Pipe-in-Pipe model for underground railways

As mentioned before, the first step in the proposed two-step approach is the calculation of displacements $\mathbf{u}_{\text{sp}}^{\text{inc}}$ and tractions $\mathbf{p}_{\text{sp}}^{\text{inc}}$ in the soil due to the passage of a train in a tunnel. The modified Pipe-in-Pipe model, which includes the presence of a free surface, is used to achieve this goal. It is based on the original PiP model for a tunnel in a full-space. Appendix D gives a summary of the principles, assumptions and mathematical equations of both models.

For convenience, the main principles are repeated here. In the original PiP model, the tunnel is modelled as an infinitely long pipe with inner radius r_{ti} and outer radius r_{to} . Similarly, the soil is assumed to behave as an infinitely long pipe with inner radius r_{si} equal to the outer radius r_{to} of the tunnel, and with an infinite outer radius. Both tunnel and soil are modelled by means of the elastic continuum equations in cylindrical coordinates (thin shell theory can also be used as an approximation for the tunnel). In the modified PiP model, the key assumption is that the near-field displacements are not influenced by the presence of the free surface. It consists of three main steps:

1. Calculation of the displacements at the tunnel-soil interface by means of the original PiP model for a tunnel embedded in a full-space.
2. The use of Green's functions for a two-and-a-half-dimensional full-space to calculate an equivalent internal source in a full-space that produces the same displacements at the tunnel-soil interface as those obtained in 1.
3. Calculation of the far-field displacements induced by the equivalent internal source in a half-space by means of Tadeu's Green's functions for a two-and-a-half-dimensional halfspace [45].

More details can be found in Appendix D.

The modified PiP model in its current formulation can only be used to calculate the displacements $\mathbf{u}_{\text{sp}}^{\text{inc}}$ in the soil. As the tractions $\mathbf{p}_{\text{sp}}^{\text{inc}}$ are also of interest, the PiP model needed to be slightly extended. Using Green's functions for stresses for a two-and-a-half-dimensional halfspace, the far-field stresses can be obtained in the third step of the modified PiP model, in a similar way as the displacements. The Green's functions for stresses can easily be found by means of the well-known equations relating displacements, strains and stresses:

$$\varepsilon_{ij} = \frac{1}{2} \left(\frac{\partial u_i}{\partial x_j} + \frac{\partial u_j}{\partial x_i} \right) \quad (7.2)$$

$$\sigma_{ij} = \lambda \varepsilon_{\text{vol}} \delta_{ij} + 2\mu \varepsilon_{ij} \quad (7.3)$$

where $\varepsilon_{\text{vol}} = \varepsilon_{xx} + \varepsilon_{yy} + \varepsilon_{zz}$ and δ_{ij} is the Kronecker delta. λ and μ are the Lamé constants of the soil. As an illustration, the expression for $G_{\sigma_{xx},x}$ is given in Eq. (7.4), using the left-handed coordinate system of Tadeu:

$$\begin{aligned}
G_{\sigma_{xx,x}}(k_n, k_z) &= (\lambda + 2\mu) \frac{-k_n}{2\rho\omega^2} \left(\frac{k_n^2}{\nu_n} (E_b + A_n^x E_{b0}) + \gamma_n (E_c + C_n^x E_{c0}) + \frac{k_z^2}{\gamma_n} (E_c + B_n^x E_{c0}) \right) \\
&+ \lambda \frac{k_n}{2\rho\omega^2} \left(-\nu_n (E_b + A_n^x E_{b0}) + \gamma_n (E_c + C_n^x E_{c0}) \right) \\
&+ \lambda \frac{k_n k_z^2}{2\rho\omega^2} \left(-\frac{1}{\nu_n} (E_b + A_n^x E_{b0}) + \frac{1}{\gamma_n} (E_c + B_n^x E_{c0}) \right)
\end{aligned} \tag{7.4}$$

Caution had to be paid to the implementation in MATLAB, as Tadeu uses a different coordinate system and a different definition of the Fourier transform with respect to the spatial coordinate than the PiP model. The meaning of the variables k_n , k_z , ν_n , γ_n , E_b , E_{b0} , E_c , E_{c0} , A_n^x , B_n^x and C_n^x is given in Appendix D.2.3. Expressions for all other Green's functions $G_{\sigma_{ij,k}}$ can also be found in Appendix D.2.3. Finally, the tractions $\mathbf{p}_{\text{sp}}^{\text{inc},j}$ in a point j acting on a plane with unit outward-pointing normal \mathbf{n}_j can be determined using Cauchy's formula:

$$\begin{Bmatrix} p_{\text{sp}}^{\text{inc},jx} \\ p_{\text{sp}}^{\text{inc},jy} \\ p_{\text{sp}}^{\text{inc},jz} \end{Bmatrix} = \begin{bmatrix} \sigma_{xx} & \sigma_{xy} & \sigma_{xz} \\ \sigma_{yx} & \sigma_{yy} & \sigma_{yz} \\ \sigma_{zx} & \sigma_{zy} & \sigma_{zz} \end{bmatrix} \begin{Bmatrix} n_{jx} \\ n_{jy} \\ n_{jz} \end{Bmatrix} \tag{7.5}$$

7.3 The BE pile model

The displacements $\mathbf{u}_{\text{sp}}^{\text{inc}}$ and the tractions $\mathbf{p}_{\text{sp}}^{\text{inc}}$ obtained with the PiP model for underground railways are used as input variables (generalized loadings) for the BE pile model. Hence, the relationship between displacements and tractions of the N nodes of the boundary elements has to be adapted as follows:

$$\mathbf{H}(\mathbf{u} - \mathbf{u}_{\text{sp}}^{\text{inc}}) = \mathbf{G}(\mathbf{p} - \mathbf{p}_{\text{sp}}^{\text{inc}}) \tag{7.6}$$

All the other equations of the pile model remain valid. They can be rearranged to get expressions for the pile displacements \mathbf{u}_{p} in function of $\mathbf{u}_{\text{sp}}^{\text{inc}}$ and $\mathbf{p}_{\text{sp}}^{\text{inc}}$. For the special case of two piles, this becomes:

$$\mathbf{u}_{\text{p}}^{\text{A}} = [\boldsymbol{\eta}_{\text{A}}]^{-1} [\boldsymbol{\Delta} \mathbf{A} \mathbf{A}_u] \mathbf{u}_{\text{sp}}^{\text{Ainc}} + [\boldsymbol{\eta}_{\text{A}}]^{-1} [\boldsymbol{\Delta} \mathbf{A} \mathbf{A}_\sigma] \mathbf{p}_{\text{sp}}^{\text{Ainc}} + [\boldsymbol{\eta}_{\text{A}}]^{-1} [\boldsymbol{\Delta} \mathbf{A} \mathbf{B}_u] \mathbf{u}_{\text{sp}}^{\text{Binc}} + [\boldsymbol{\eta}_{\text{A}}]^{-1} [\boldsymbol{\Delta} \mathbf{A} \mathbf{B}_\sigma] \mathbf{p}_{\text{sp}}^{\text{Binc}} \tag{7.7}$$

$$\mathbf{u}_{\text{p}}^{\text{B}} = [\boldsymbol{\eta}_{\text{B}}]^{-1} [\boldsymbol{\Delta} \mathbf{B} \mathbf{A}_u] \mathbf{u}_{\text{sp}}^{\text{Ainc}} + [\boldsymbol{\eta}_{\text{B}}]^{-1} [\boldsymbol{\Delta} \mathbf{B} \mathbf{A}_\sigma] \mathbf{p}_{\text{sp}}^{\text{Ainc}} + [\boldsymbol{\eta}_{\text{B}}]^{-1} [\boldsymbol{\Delta} \mathbf{B} \mathbf{B}_u] \mathbf{u}_{\text{sp}}^{\text{Binc}} + [\boldsymbol{\eta}_{\text{B}}]^{-1} [\boldsymbol{\Delta} \mathbf{B} \mathbf{B}_\sigma] \mathbf{p}_{\text{sp}}^{\text{Binc}} \tag{7.8}$$

Similar formulae are obtained in case of three, four or even more piles. As the mathematical expressions for the matrices are rather lengthy, they are given in Appendix E, for the cases of two (section E.3.1) and four piles (section E.3.2).

7.4 Results for a single pile

The BE pile model is used to calculate the response of a single pile with an unconstrained pile-head to underground railway induced loadings. The tunnel is located at a depth of 25 m beneath the free surface. The pile has a length $L_p = 20$ m and an offset of 10 m with respect to the tunnel axis, as depicted in Figure 7.3. The various soil, tunnel and pile parameters are given in Table 7.1.

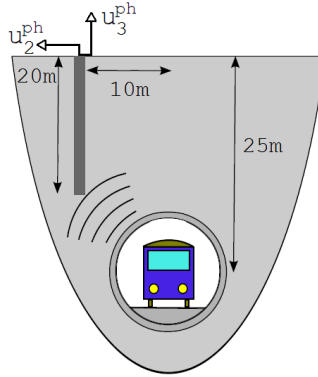


Figure 7.3: Location of a single pile with length $L_p = 20$ m. The tunnel is located at a depth of 25 m beneath the free surface, and the pile has an offset of 10 m with respect to the tunnel axis. The horizontal (u_2^{ph}) and vertical (u_3^{ph}) pile-head response are investigated.

Parameter	Soil	Tunnel	Piles
E [Pa]	550×10^6	50×10^9	30×10^9
ν [-]	0.44	0.30	0.25
μ [Pa]	191×10^6	19.2×10^9	12×10^9
λ [Pa]	1400×10^6	28.8×10^9	12×10^9
ρ [kg/m ³]	2000	2500	2500
β_μ [-]	0.03	0	0
β_λ [-]	0.03	0	0
c_s [m/s]	309.0	2773.5	2190.9
c_p [m/s]	944.1	5188.7	3794.7
d [m]	–	–	$1/\sqrt{2}$

Table 7.1: Soil, tunnel and pile parameters used to calculate the response of piled foundations to underground railway induced vibrations.

Figure 7.4 shows the horizontal and vertical pile-head response obtained with three different models. The first of these models is Novak's model [37], a relatively old analytical model in which plain strain conditions are assumed. The two other models are the PiP model for piles and the current BE pile

model. It is clear that as well for the horizontal (Figures 7.4(a) and (b)) as the vertical (Figures 7.4(c) and (d)) response, the agreement between the two novel models is very good. For the vertical response, it can be seen that there is a significant difference with Novak's model. In the lower frequency range, the difference is limited to ~ 5 dB, but at higher frequencies, differences up to 15 dB can be noticed. As Novak's model is quite approximate, it is believed that the results of the novel models are more accurate.

Figure 7.4 shows also the greenfield vibration levels, i.e. the surface vibration predictions at the corresponding location if no foundation is present. It is clearly illustrated that piled foundations can affect surface vibration levels. The effect is most obvious for the vertical displacement, and the addition of the pile is generally seen to attenuate the surface vibration levels, particularly at higher frequencies [28].

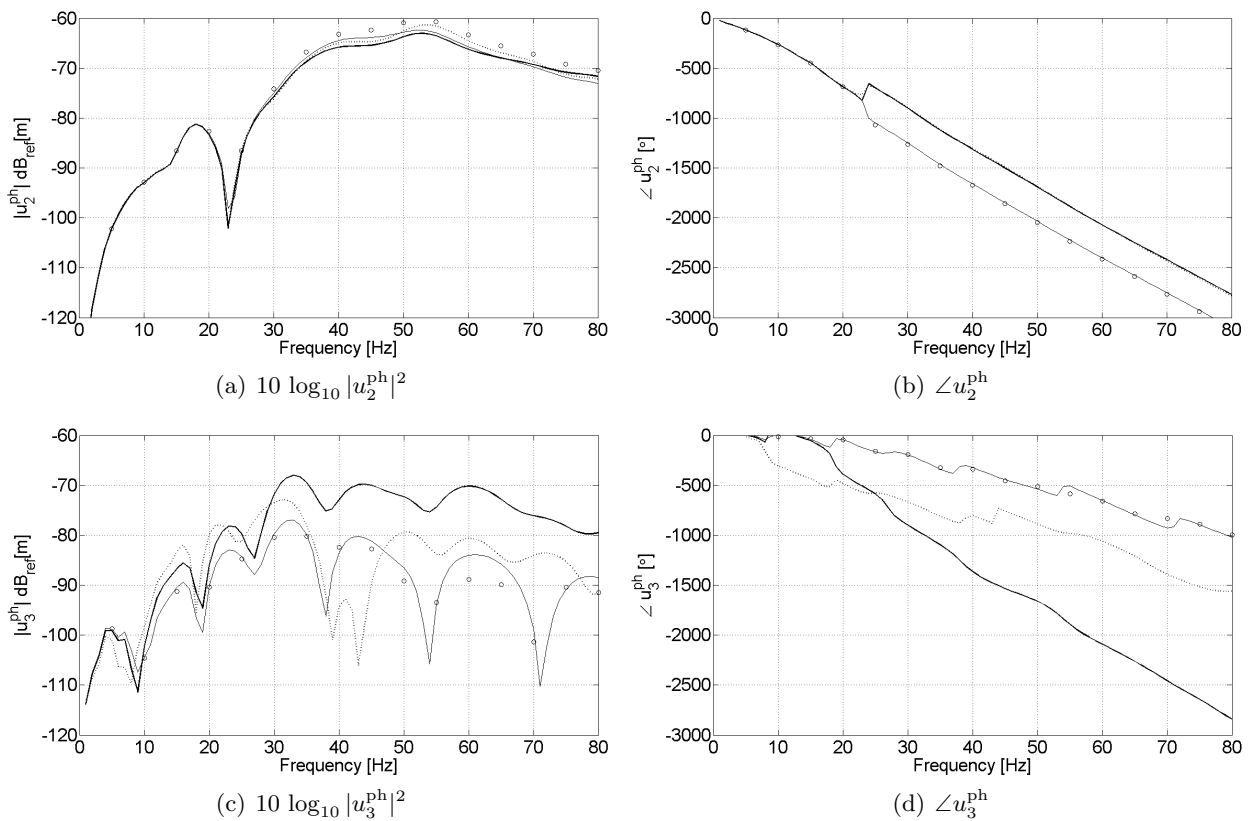


Figure 7.4: (a)-(b) Horizontal and (c)-(d) vertical pile-head response due to underground railway induced loadings, with comparison to the greenfield vibration levels (bold line). The results are calculated using Novak's model (dotted line), the PiP model for piles (solid line) and the BE pile model (circles).

7.5 Results for a four-pile group

The calculations of section 7.4 are extended to a four-pile group foundation. Again, the tunnel is located at a depth of 25 m beneath the free surface. Four piles, each with a length $L_p = 5$ m, are placed symmetrically with respect to the tunnel axis. The separation distance between all piles is $s = 1.50$ m. The various soil, tunnel and pile parameters can once more be found in Table 7.1.

Figure 7.5 shows the vertical pile-head response of the outer and the inner piles, computed using the PiP model for piles and the BE pile model. The greenfield vibration levels are also indicated. Little variation is observed in the pile-head response of the outer and inner piles, and again, the addition of the piles is generally seen to attenuate the surface vibration levels, particularly at higher frequencies. Whilst some localized variation (< 10 dB) between the two models is observed, the general agreement between the two models is good. It is expected that the agreement will improve as the pile separation distance increases, as it was seen from the interaction factors (paragraph 5.1.2) that the assumption of an uncoupled source-receiver model used in the PiP model for piles is more appropriate at larger pile separation distances. It can be seen that in this specific case, the inaccuracy inherent in a prediction that ignores the presence of piled foundations is highly dependent on frequency, and can range from -15 dB to $+12$ dB. This represents a significant margin for a prediction model of vibration from underground railways. For this reason, it is recommended that future models predicting vibration from underground railways in an urban environment consider the influence of any nearby piled foundations [28].

Although the BE pile model has a greater overall accuracy than the PiP model for piles, the latter provides a great improvement in computational efficiency. For example, obtaining the results presented in Figure 7.5 from the incident wavefield requires less than a minute for the PiP model for piles, whereas the BE model has a runtime of the order of hours [28].

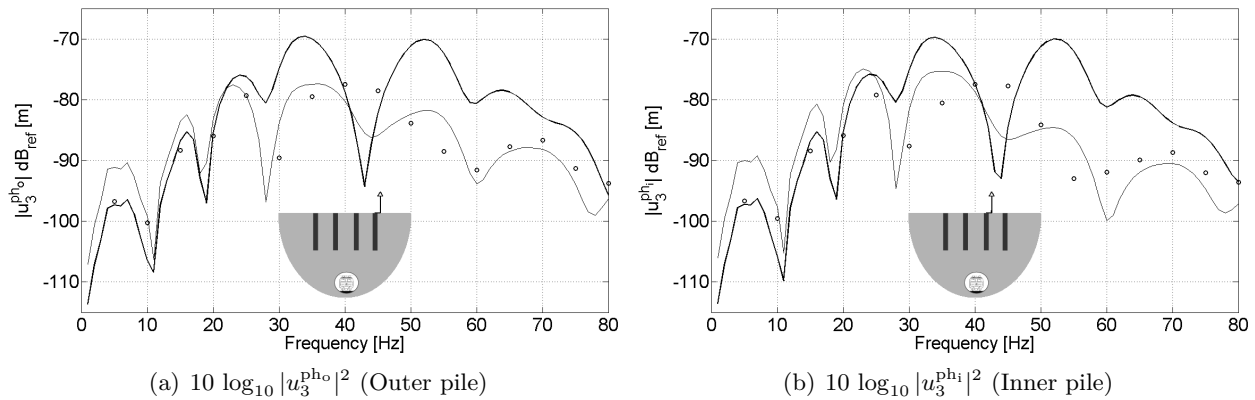


Figure 7.5: Vertical pile-head response of (a) the outer and (b) the inner piles due to underground railway induced loadings, with comparison to the greenfield vibration levels (bold line). The results are calculated using the PiP model for piles (solid line) and the BE pile model (circles).

7.6 Case study

In this section, a virtual case study is presented to illustrate the application of the BE pile model. It will also be used to investigate the effect of the foundation design, the contribution of horizontal and rotational motion, the importance of pile-soil-pile interactions and the isolation performance of base isolation.

Consider an underground railway at a depth of 25 m beneath the free surface. Two different pile designs are presented in Figure 7.6. Both designs have the same static bearing capacity, but it is expected that their dynamic response will differ. The comparison is made in terms of the total power flowing through the pile-heads into the semi-infinite columns (or equivalent viscous damper). The values of the various soil, tunnel and pile parameters are given in Table 7.1 and 7.2.

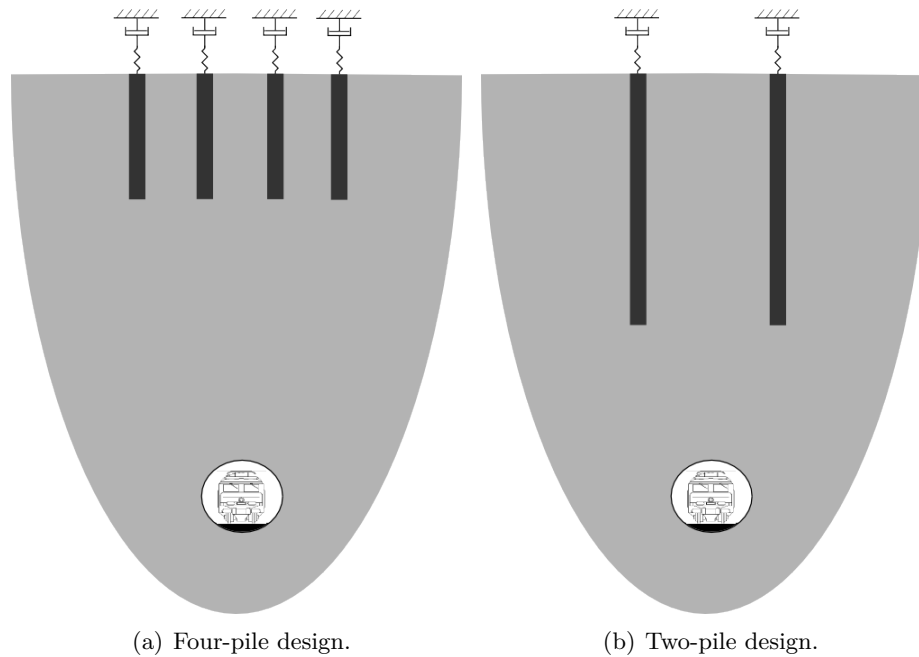


Figure 7.6: Two different pile designs analysed in the case study.

Case	L_p [m]	s [m]
Two piles	10	3.0
Four piles	5	1.5

Table 7.2: Parameters of the two different pile designs.

7.6.1 Comparison of the pile designs

Figure 7.7 shows the total mean power flow for the two different pile designs, in case of unisolated semi-infinite columns. As the damping loss factors of the piles equal zero, \bar{P}_{in} should equal \bar{P}_{out} , and this conservation of energy is confirmed in Figure 7.7. It can be seen that almost over the whole frequency range considered, the pile design with four short piles results in more total power flowing upwards compared to the two-pile pile design. However, the power flow insertion gain (PFIG) of the second pile design varies a lot: in some regions, there is a difference up to -10 dB, while in other regions the difference is negligible. Around 30 Hz, there is even a positive PFIG.

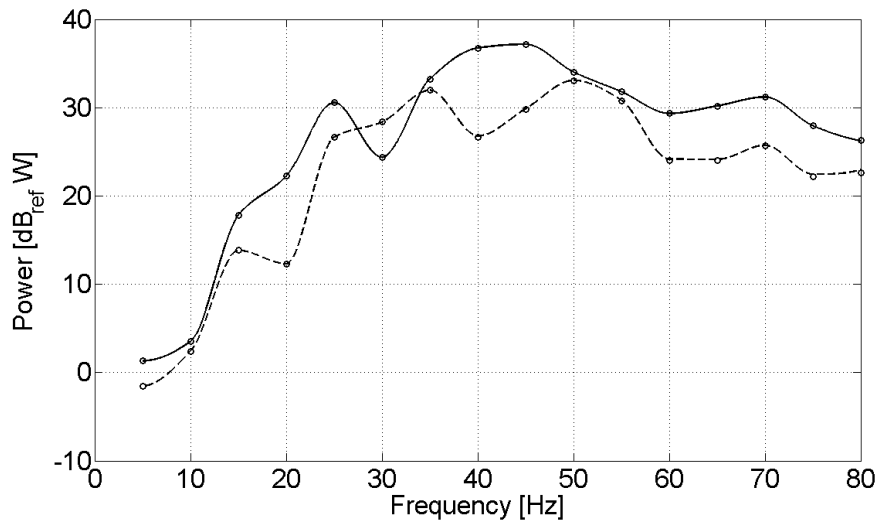


Figure 7.7: Power flow analysis for the two-pile (dashed line) and four-pile (solid line) design. The plain lines represent \bar{P}_{in} , while the circles represent \bar{P}_{out} .

It is rather difficult to explain intuitively the differences between the pile designs, as revealed in Figure 7.7. Therefore, investigation of the power flow distribution can be helpful. The power flow distribution at 25 Hz is illustrated in Figure 7.8 for both pile designs. Figure 7.8(b) reveals that there is indeed more power entering the pile-tip regions in the two-pile design, but the piles have the ability to spread out a significant fraction of the power through the upper part of the pile skins. The resulting power flowing upwards through the pile-heads into the semi-infinite columns is consequently relatively small. In contrary, Figure 7.8(a) illustrates that there is more power flowing through the pile-heads in the four-pile design, despite the fact that there is less power entering the lower parts of the piles. It seems that the piles are not able to redistribute the power to the soil, possibly because of the smaller pile separation distance s (cfr. Table 7.2).

It is emphasized that these results are obtained for a specific set of parameters. A lot of factors play a role in these kind of problems, and therefore it is difficult to draw general conclusions based on this example. However, the current BE pile model has the ability to calculate the response and the PF distribution for every specific case.

In the following paragraphs, the four-pile design will be used to investigate several aspects in more detail.

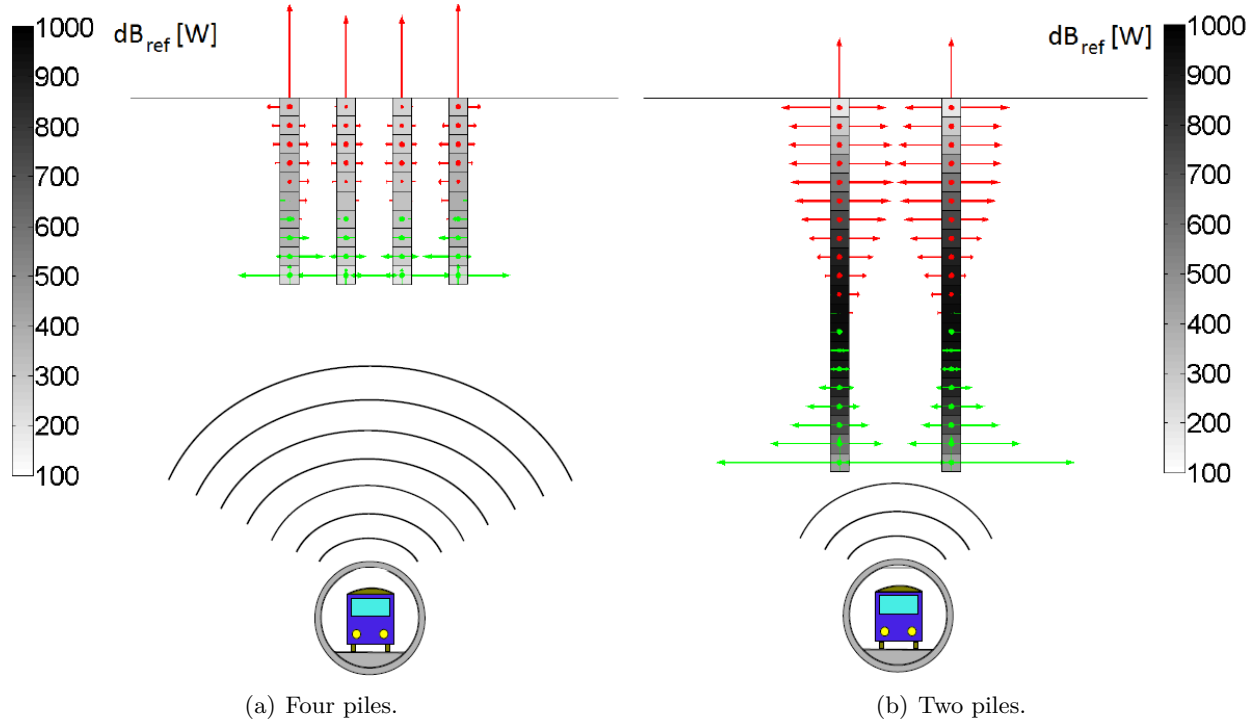


Figure 7.8: Power flow distribution for (a) the four-pile and (b) the two-pile design at 25 Hz.

7.6.2 The significance of horizontal and rotational motion

As a simplification, existing models rarely consider the horizontal component of ground-borne vibration. One of the main advantages of using power flow is that it accounts for multidirectional vibration, which enables to investigate the validity of this assumption.

Figure 7.9 shows the relative contributions of the horizontal, vertical and rotational motion to the total mean power flow, and this for the inner as well as for the outer piles. It is clear that the horizontal and to a lesser extent the rotational motion can contribute significantly to the total mean power flow, and they are non-negligible. At some frequencies the contribution of the rotational power component is negative, although the total mean power flow into the columns is positive (as must be as no internal source exist). This corresponds to power flowing from the building to be dissipated in the foundation. The absolute values of the different power contributions are presented in Figure 7.10. It turns out that the peaks in the relative contribution of \bar{P}_{hor} (Figure 7.9) correspond to drops of \bar{P}_{ver} .

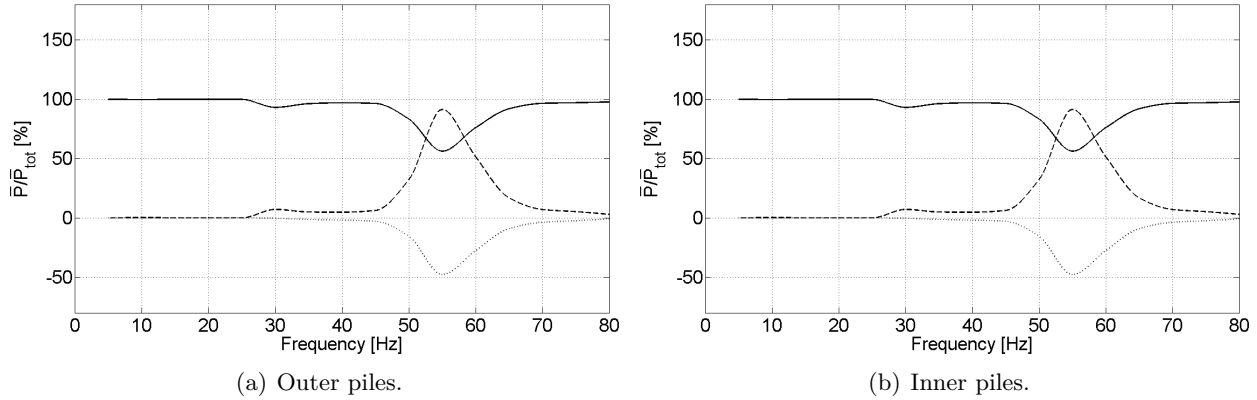


Figure 7.9: Relative contribution of the horizontal $\bar{P}_{hor}/\bar{P}_{tot}$ (dashed line), vertical $\bar{P}_{ver}/\bar{P}_{tot}$ (solid line) and rotational $\bar{P}_{\theta}/\bar{P}_{tot}$ (dotted line) components to the total mean power flow into the semi-infinite columns of (a) the outer and (b) the inner piles.

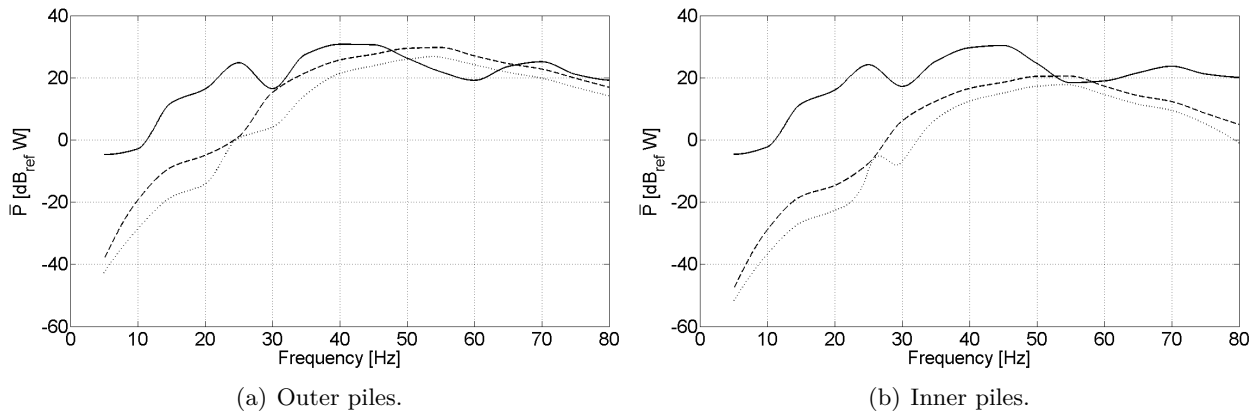


Figure 7.10: Horizontal \bar{P}_{hor} (dashed line), vertical \bar{P}_{ver} (solid line) and rotational \bar{P}_{θ} (dotted line) components of the total mean power flow into the semi-infinite columns of (a) the outer and (b) the inner piles.

7.6.3 The significance of pile-soil-pile interactions (PSPI)

The results obtained in paragraph 7.6.1 are compared to those of a model that disregards PSPI. The latter is identical to the BE model presented before, except that the soil’s FRF matrix \mathbf{H}_s is reduced to a diagonal matrix, i.e. all off-diagonal submatrices \mathbf{H}_s^{ij} ($i \neq j$) are set equal to $\mathbf{0}$.

Figure 7.11 shows the effect of PSPI. Up to 50 Hz, PSPI leads to a reduction of total power flow into the semi-infinite columns, while at higher frequencies the overall effect is less univocal. For instance, disregarding PSPI at 60 Hz may lead to an underestimation of the total power flow of 1.5 dB, while at 70 Hz the effect is negligible.

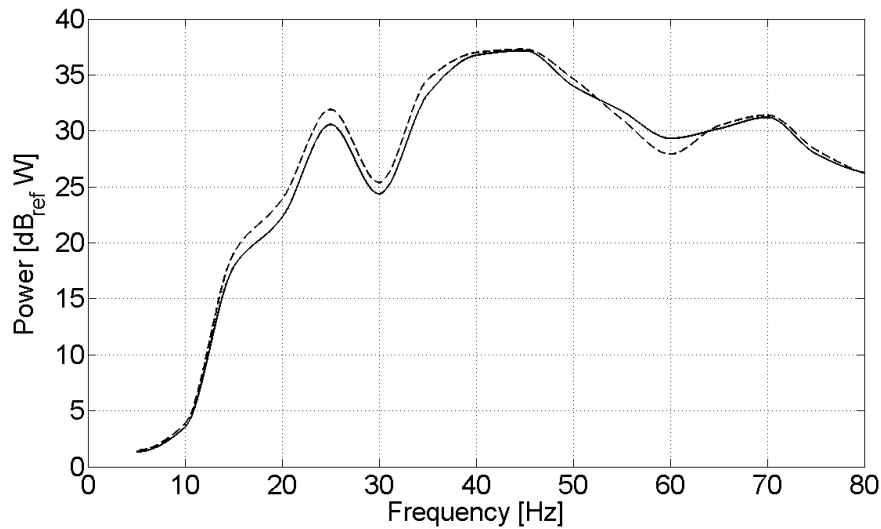


Figure 7.11: Total mean power flow into the semi-infinite columns vs. frequency f , as computed using the current BE pile model (solid line) and a model that disregards PSPI (dashed line).

7.6.4 Efficiency of base isolation

As mentioned in section 1.1, the use of base isolation is a widely used measure in buildings to reduce the effects of ground-borne vibrations. Isolation bearings have been described in section 3.3, and Eq. (3.69) points out how they can be incorporated in the mathematical formulation of the model.

Figure 7.12 shows the effect of base isolation on the total power flow entering the semi-infinite columns, and this for isolation frequencies of 5, 10 and 15 Hz (section 3.3). This range of frequencies is typically found in practice: a 15 Hz isolation is representative of high-hysteresis rubber bearings, while a 5 Hz isolation is representative of undamped steel springs. Due to the semi-infinite character of the column, no ‘mass on spring’-resonance can be established. It is clear that the choice of isolation frequency plays a dominant role in the efficiency of the isolation. The lower the isolation frequency, the more efficient the measure is. This result suggests that steel springs are preferred to rubber bearings, as the isolation frequency can be lowered more significantly. However, the reduction in power flowing into the column is limited to approximately 10 to 15 dB, which is much less than the values of 25 up to 30 dB sometimes predicted by simplified models.

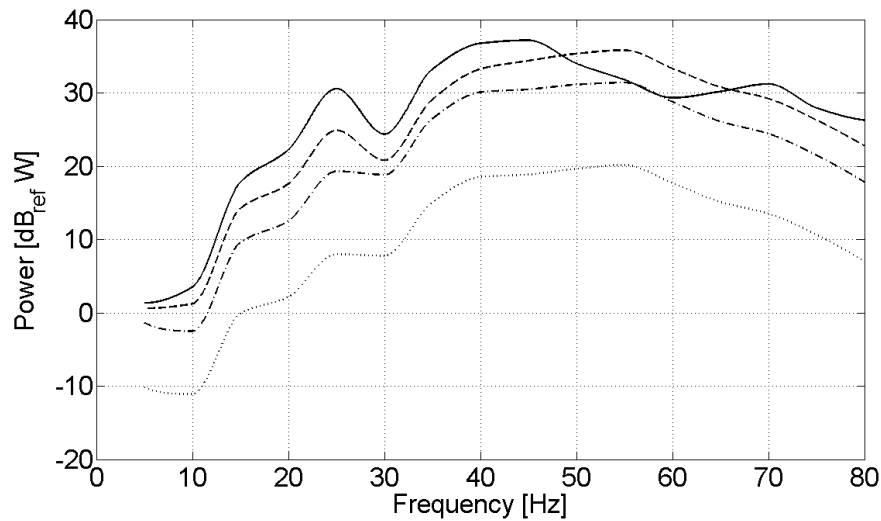


Figure 7.12: Total mean power flow into the semi-infinite columns vs. frequency f , in case of an unisolated building model (solid line) and in case of base isolation with isolation frequencies of 15 Hz (dashed line), 10 Hz (dash-dot line) and 5 Hz (dotted line).

7.7 Conclusion

In this chapter, the PiP model for underground railways has been combined with the BE pile model, assuming uncoupling of source and receiver. The response of a single pile and a four-pile group have been calculated and compared to results of other models, and good agreement is found. The results indicate that the presence of piled foundations can have a significant influence on the surface vibration levels. Furthermore, a virtual case study, comparing two different pile designs, has revealed that it is not always clear which factor has the largest impact on the behaviour of the system, and a lot of uncertainty remains. Nevertheless, the efficiency of base isolation has been illustrated, and the results suggest that steel springs are preferred to rubber bearings.

Chapter 8

Conclusions and recommendations for further work

8.1 Conclusions

In this MSc thesis, several aspects of the vibration response of piled foundations have been investigated. An existing single pile BE model has been extended. This includes the incorporation of Timoshenko beam theory and a simplistic building model (semi-infinite column). Furthermore, the concept of power flow analysis has been introduced, and it has proven throughout this dissertation to be very useful to gain more insight into the behaviour of the system.

The extended BE pile model has been used to perform validation calculations for the PiP model for piles. For an infinite pile in a full-space as well as for a finite pile in a half-space, the two models are found to be in good agreement. In addition to its accuracy, the PiP model for piles is computational efficient, which offers great perspectives to use it as an engineering tool.

The BE model has been extended to a multiple pile BE model which accounts for the interaction between neighbouring piles through wave propagation in the soil. It has been validated in terms of dynamic interaction factors; good agreement with other available models has been observed. Afterwards, the model has been used to investigate the shadow effect. An almost linear relationship between the power flow insertion gain and the position of the load is observed, as long as the wavelength is larger than the distance between the piles and the load. As the wavelength approaches this distance, there is an increased tendency to wave scattering which results in a reversal of the results. This should be borne in mind when the superposition of interaction factors is used to approximate the pile-soil-pile interactions.

The extended multiple pile BE model has eventually been used to calculate the response of piled foundations to railway induced loadings. It is assumed that the incident wavefield is not affected by the presence of the receiver, which results in an uncoupling of source and receiver, and hence a two-step approach (subdomain formulation). This procedure can be justified if the distance between the source and the receiver is sufficiently large compared to the wavelengths, which is unfortunately not always the case. The response of a single pile and a four-pile group have been calculated and compared to

results of the PiP model for piles. The two models are once more found to be in good agreement, and it is believed that they produce more accurate results than existing models. The results indicate that the presence of piled foundations can have a significant influence on the surface vibration levels, and therefore, it is recommended that future models predicting vibration from underground railways in an urban environment consider the influence of any nearby piled foundations.

A virtual case study has been carried out to investigate the dynamic behaviour of two different pile designs. It is clear that the pile design can have a major influence on the total mean power flowing into the building, although it is very difficult to draw general conclusions. Nevertheless, it has been demonstrated that the choice of isolation frequency plays a dominant role in the effectiveness of base isolation, and this suggests that steel springs are preferred to rubber bearings, as the isolation frequency can be lowered more significantly. Furthermore, the significance of PSPI has been revealed, as well as the contribution of horizontal and rotational motion. Although these results are very dependent on a variety of factors, it is important to note that the current BE pile model has the ability to calculate the response and the PF distribution for every specific case.

8.2 Recommendations for further work

Although the BE pile model in its current form has proven to be useful and reliable, the model has the potential for significant further development.

The upper frequency limit till which the model can produce results with a reliable accuracy is ~ 80 Hz. In order to raise this limit to 250 Hz, the BE mesh with constant elements has to be refined, but this is currently limited by the computing power (as it is desirable that the model can be solved on a personal computer). Therefore, the use of higher-order boundary elements is recommended in order to use less elements for the same accuracy. In addition to this, the use of a more efficient BE implementation instead of the currently used MATLAB-code may lead to an improved performance. A possibility could be to use the toolbox BEMFUN, which is implemented in C++. Improved performance can also be achieved by using half-space Green's functions as the fundamental solution in the BE formulation. Although calculation of these Green's functions requires some more computational effort, the required amount of degrees of freedom would significantly be lowered, as it would not be necessary any more to discretize the free-surface. The ElastoDynamics Toolbox (EDT) [41, 42] could be used for this purpose.

Another aspect is the incorporation of a pile cap in the numerical model. Again, power flow analysis could help to gain a clear understanding of the effects related to this adjustment, e.g. the redistribution of power from one pile to another one through the pile cap.

More generally spoken, it is necessary to develop models which account for the coupling between source and receiver. This is especially needed for predictions in urban environments, where the distance between source and receiver is often small compared to the wavelength of the waves in the soil. The author hopes to contribute to the development of such models.

Bibliography

- [1] D. Aubry and D. Clouteau: A subdomain approach to dynamic soil-structure interaction. In V. Davidovici and R.W. Clough, editors, *Recent advances in Earthquake Engineering and Structural Dynamics*, pp. 251–272. Nantes: Ouest Editions/AFPS, 1992.
- [2] P.K. Banerjee and S.M. Mamoon: A fundamental solution due to a periodic point force in the interior of an elastic half-space. *Earthquake Engineering and Structural Dynamics*, 19, pp. 91–105, 1990.
- [3] A.A. Becker: *The Boundary Element Method in Engineering: A Complete Course*. Berkshire: McGraw-Hill, 1992.
- [4] D.E. Beskos: Wave propagation through ground. In G.D. Manolis and T.G. Davies, editors, *Boundary Element Techniques in Geomechanics*. Computational Mechanics Publications & Elsevier Applied Science, 1993.
- [5] P. Bettess: *Infinite elements*. Penshaw Press, 1992.
- [6] C.A. Brebbia and J. Dominguez: *Boundary elements: An Introductory Course*. McGraw-Hill, 1992.
- [7] A.K. Chopra: *Dynamics of structures: Theory and applications to earthquake engineering*. Third edition, New Jersey: Pearson Prentice Hall, 2007.
- [8] D. Clouteau, M. Arnst, T.M. Al-Hussaini and G. Degrande: Freefield vibrations due to dynamic loading on a tunnel embedded in a stratified medium. *Journal of Sound and Vibration*, 283, pp. 173–199, 2005.
- [9] P. Coulier and M. Beckers: Vibrational discomfort in buildings. *Young European Arena of Research*, Brussels, 2010.
- [10] L. Cremer and M. Heckl: *Structure-Borne Sound: Structural Vibrations and Sound Radiation at Audio Frequencies*. Berlin: Springer-Verlag, 1973.
- [11] D.P. Cryer: *Modelling of Vibration in Buildings with application to Base Isolation*. PhD thesis, University of Cambridge, 1994.
- [12] G. Degrande, D. Clouteau, R. Othman, M. Arnst, H. Chebli, R. Klein, P. Chatterjee and B. Janssens: A numerical model for ground-borne vibrations from underground railway traffic

- based on a periodic finite element - boundary element formulation. *Journal of Sound and Vibration*, 293, pp. 645–666, 2006.
- [13] J. Dominguez: Boundary Elements in Dynamics. *Computational Mechanics Publications & Elsevier Applied Science*, Southampton & Essex, 1993.
- [14] J.A. Forrest: *Modelling of ground vibration from underground railways*. PhD thesis, University of Cambridge, 1999.
- [15] J.A. Forrest and H.E.M. Hunt: Ground vibration generated by trains in underground tunnels. *Journal of Sound and Vibration*, 294, pp. 706–736, 2006.
- [16] F. Frederich: Die Gleislage – aus fahrzeugtechnischer Sicht [Effect of track geometry on vehicle performance]. *Zeitschrift für Eisenbahnwesen und Verkehrstechnik – Glasers Annalen*, 108(12), pp. 355–362, 1984.
- [17] C.G. Gordon: Generic vibration criteria for vibration-sensitive equipment. *Proc. SPIE*, 3786, pp. 22–39, 1999.
- [18] K.F. Graff: *Wave motion in elastic solids*, Oxford: Clarendon Press, 1975.
- [19] P. Grootenhuis: Noise generated by intermittent structure borne vibrations. *Building Research and Information*, 20(3), pp. 157–161, 1992.
- [20] R. Hildebrand: *Countermeasures against railway ground and track vibrations*. PhD thesis, KTH Royal Institute of Technology, Stockholm, 2001.
- [21] M.F.M. Hussein: *Vibration from underground railways*. PhD thesis, University of Cambridge, 2004.
- [22] M.F.M. Hussein: *Personal communication*, 2009.
- [23] M.F.M. Hussein, S. Gupta, H.E.M. Hunt, G. Degrande and J.P. Talbot: An efficient model for calculating vibration from a railway buried in a half-space. *The Thirteenth International Congress on Sound and Vibration*, Vienna, 2006.
- [24] A.M. Kaynia: *Dynamic stiffness and seismic response of pile groups*. PhD thesis, Massachusetts Institute of Technology, 1982.
- [25] R.L. Kuhlemeyer: Vertical vibration of piles. *Journal of Geotechnical Engineering*, American Society of Civil Engineers, 105(2), pp. 273–287, 1979.
- [26] R.L. Kuhlemeyer: Static and dynamic laterally loaded floating piles. *Journal of Geotechnical Engineering*, American Society of Civil Engineers, 105(2), pp. 289–304, 1979.
- [27] K.A. Kuo and H.E.M. Hunt: An efficient formulation for calculating the vibration response of piled foundations due to excitation from an underground railway. *Proceedings of the International Conference on Computing in Civil and Building Engineering*, Nottingham, 2010.

- [28] K.A. Kuo, P. Coulier, H.E.M. Hunt and G. Degrande: A comparison of two models for the vibration response of piled foundations to inertial and underground railway induced loadings. *The 17th International Congress on Sound and Vibration*, Cairo, 2010. Accepted for publication.
- [29] J.C. Lachat: *A Further Development of the Boundary Integral Technique for Elastostatics*. PhD thesis, University of Southampton, 1975.
- [30] H. Lamb: On the Propagation of Tremors over the Surface of an Elastic Solid. *Philosophical transactions of the Royal Society of London*, London: Harrison and sons, p. 42, 1904.
- [31] R.S. Langley: Analysis of power flow in beams and frameworks using the direct-dynamic stiffness method. *Journal of Sound and Vibration*, 136(3), pp. 439–452, 1990.
- [32] P.B. Lindley: Engineering Design with Natural Rubber. *The Malaysian Rubber Producer's Research Association*, fifth edition, 1984.
- [33] G.D. Manolis and D.E. Beskos: *Boundary Element Methods in Elastodynamics*. London: Unwin Hyman, 1988.
- [34] Matlab.
<http://www.mathworks.com>
- [35] F.A. Mohammad and V.V. Krylov: Finite element calculation of elasto-dynamic fields generated by a point source in the layered ground. *Proceedings of the Institute of Acoustics*, 22(2), pp. 271–278, 2000.
- [36] D.E. Newland: *Mechanical Vibration Analysis and Computation*. Longman, 1989.
- [37] M. Novak: Dynamic stiffness and damping of piles. *Canadian Geotechnical Journal*, 11(4), pp. 574–598, 1974.
- [38] PiP.
<http://www.pipmodel.com>
- [39] H.G. Poulos and E.H. Davis: *Pile Foundation Analysis and Design*. John Wiley & Sons, 1980.
- [40] L. Rikse: *Modelling of subway induced vibrations using the Pipe-in-Pipe model*. MSc thesis, Katholieke Universiteit Leuven & University of Cambridge, 2007.
- [41] M. Schevenels, G. Degrande and S. François: EDT: An ElastoDynamics Toolbox for MATLAB. *Computers & Geosciences*. In press. <http://dx.doi.org/10.1016/j.cageo.2008.10.012>
- [42] M. Schevenels, G. Degrande and S. François: EDT: An ElastoDynamics Toolbox for MATLAB. *Proceedings of the Inaugural International Conference of the Engineering Mechanics Institute (EM08)*, Minneapolis, Minnesota, U.S.A., May 2008.
- [43] R. Sen *et al.*: Dynamic analysis of piles and pile groups embedded in homogeneous soils. *Earthquake Engineering and Structural Dynamics*, 13, pp. 53–65, 1985.
- [44] A.J.B. Tadeu and E. Kausel: Green's functions for two-and-a-half-dimensional elastodynamic problems. *Journal of Engineering Mechanics*, 126(10), pp. 1093–1097, 2000.

- [45] A.J.B. Tadeu, J. António and L. Godinho: Green's functions for two-and-a-half-dimensional elastodynamic problems in a half-space. *Computational Mechanics*, 27, pp. 484–491, 2001.
- [46] J.P. Talbot: *On the Performance of Base-Isolated Buildings: A Generic Model*. PhD thesis, University of Cambridge, 2001.
- [47] P.C. Vinh and R.W. Ogden: On formulas for the Rayleigh wave speed. *Wave Motion*, 39, pp. 191–197, 2004.
- [48] A.M. Wahl: *Mechanical springs*. Second edition, McGraw-Hill, 1963.
- [49] L.T. Wheeler and E. Sternberg: Some theorems in classical elastodynamics. *Arch. Rational Mech. Anal.*, 31, pp. 51–90, 1968.

Appendix A

Integral transformations

A.1 Fourier transform with respect to time

The time domain representation $f(t)$ can be transformed by means of a Fourier transformation to the frequency domain representation $F(\omega)$:

$$F(\omega) = \int_{-\infty}^{+\infty} f(t)e^{-i\omega t} dt \quad (\text{A.1})$$

$$f(t) = \frac{1}{2\pi} \int_{-\infty}^{+\infty} F(\omega)e^{i\omega t} d\omega \quad (\text{A.2})$$

A.2 Fourier transform with respect to a spatial coordinate

The spatial domain representation $f(x)$ can be transformed by means of a Fourier transformation to the wavenumber domain representation $F(\xi)$:

$$F(\xi) = \int_{-\infty}^{+\infty} f(x)e^{-i\xi x} dx \quad (\text{A.3})$$

$$f(x) = \frac{1}{2\pi} \int_{-\infty}^{+\infty} F(\xi)e^{i\xi x} d\xi \quad (\text{A.4})$$

Appendix B

The Boundary Element Method

In this dissertation, the boundary element (BE) method is used to model the vibration response of piled foundations. The goal of this appendix is to summarize the numerical formulation of the BE method as it is used throughout this thesis. Many books on the subject give a much more detailed introduction, for instance the works by Becker [3], Dominguez [13] or Manolis [33].

B.1 The elastodynamic problem

The equation describing motion in a three-dimensional homogeneous isotropic body Ω with boundary Γ , assuming linear elasticity, is given by Eq. (B.1) [13].

$$\mu \nabla^2 \mathbf{u} + (\lambda + \mu) \nabla \nabla \cdot \mathbf{u} + \rho \mathbf{b} = \rho \ddot{\mathbf{u}} \quad (\text{B.1})$$

\mathbf{u} is the displacement vector at a point \mathbf{x} , \mathbf{b} is the vector of body forces, and ρ is the density of the solid. λ and μ are Lamé constants and can be related to the more common material parameters E , G and ν as follows: $\lambda = 2\nu G / (1 - 2\nu)$ and $\mu = G = E / (2(1 + \nu))$. The system of displacement equations (B.1), also called the Navier equations, must be satisfied at every interior point of Ω . As mentioned in chapter 2, time-harmonic steady-states are considered, and complex notation is used for all field variables, e.g. $\mathbf{u}(\mathbf{x}, t) = \Re(\mathbf{u}(\mathbf{x}, \omega) e^{i\omega t})$.

When considering visco-elastic solids, the stress and strain are still linearly related, but they also depend on the previous strain or stress history, respectively. Visco-elasticity includes phenomena as relaxation and creep. It can be proven (e.g. Dominguez [13]) that one can use the same formulation for time-harmonic visco-elastic problems as for linear elastic ones; only the fact that the Lamé constants become complex has to be taken into account. This is known as the correspondence principle. The complex Lamé constants can be written as:

$$\mu = \Re(\mu)(1 + 2\beta_\mu i) \quad (\text{B.2})$$

$$\lambda = \Re(\lambda)(1 + 2\beta_\lambda i) \quad (\text{B.3})$$

β_μ and β_λ represent the frequency independent material damping ratios. Frequency independent damping is also known as hysteretic damping [46]. The imaginary part of λ and μ give rise to exponentially decaying amplitudes of propagating waves.

B.2 The dynamic (Betti-Rayleigh) reciprocity theorem

The reciprocal theorem in elastodynamics is an extension of Betti's theorem in elastostatics. It relates two arbitrary states of the body Ω . The theorem can be proven using a weighted residual statement and integration by parts (see for example Wheeler [49]).

Let \mathbf{u} , \mathbf{p} and \mathbf{b} be the displacements, tractions and body forces (per unit mass) associated with a first state of Ω . A second state can be defined by \mathbf{u}^* , \mathbf{p}^* and \mathbf{b}^* . In the case of time-harmonic steady-states with angular frequency ω , the reciprocal theorem can be written as follows:

$$\int_{\Gamma} \mathbf{p} \cdot \mathbf{u}^* d\Gamma + \int_{\Omega} \rho \mathbf{b} \cdot \mathbf{u}^* d\Omega = \int_{\Gamma} \mathbf{p}^* \cdot \mathbf{u} d\Gamma + \int_{\Omega} \rho \mathbf{b}^* \cdot \mathbf{u} d\Omega \quad (\text{B.4})$$

B.3 The fundamental solution

The fundamental solution is an elastodynamic state which is obtained when a unit time-harmonic point load in the direction k is applied at a source point \mathbf{i} in an infinite elastic domain (Figure B.1(b)). The resulting displacements and tractions in the direction l at a receiver point \mathbf{x} are denoted as u_{lk}^* respectively p_{lk}^* . The load applied corresponds to a body force ρb_k^* :

$$\rho b_k^* = \delta(r) \delta_{lk} \quad (\text{B.5})$$

where $\delta(r) = \delta(\mathbf{x} - \mathbf{i})$ is the Dirac delta function, r is the distance between source and receiver, and δ_{lk} is the Kronecker delta. u_{lk}^* and p_{lk}^* are often called the Green's functions of the formulation.

In this dissertation, the fundamental solution due to a unit point load in a full-space is used. In this case, explicit analytical expressions exist [13]:

$$u_{lk}^* = \frac{1}{4\pi\rho c_s^2} (\psi \delta_{lk} - \chi r_{,l} r_{,k}) \quad (\text{B.6})$$

$$p_{lk}^* = \frac{1}{4\pi} \left[\left(\frac{d\psi}{dr} - \frac{1}{r} \chi \right) \left(\delta_{lk} \frac{\partial r}{\partial n} + r_{,k} n_l \right) - \frac{2}{r} \chi \left(n_k r_{,l} - 2r_{,l} r_{,k} \frac{\partial r}{\partial n} \right) - 2 \frac{d\chi}{dr} r_{,l} r_{,k} \frac{\partial r}{\partial n} \dots \right. \\ \left. + \left(\frac{c_p^2}{c_s^2} - 2 \right) \left(\frac{d\psi}{dr} - \frac{d\chi}{dr} - \frac{2}{r} \chi \right) r_{,l} n_k \right] \quad (\text{B.7})$$

with

$$\psi = \left(1 + \frac{1}{k_s^2 r^2} + \frac{1}{k_s r} \right) \frac{e^{-k_s r}}{r} - \frac{c_s^2}{c_p^2} \left(\frac{1}{k_p^2 r^2} + \frac{1}{k_p r} \right) \frac{e^{-k_p r}}{r} \quad (\text{B.8})$$

$$\chi = \left(1 + \frac{3}{k_s^2 r^2} + \frac{3}{k_s r}\right) \frac{e^{-k_s r}}{r} - \frac{c_s^2}{c_p^2} \left(1 + \frac{3}{k_p^2 r^2} + \frac{3}{k_p r}\right) \frac{e^{-k_p r}}{r} \quad (\text{B.9})$$

and

$$k_p = i \frac{\omega}{c_p} \quad (\text{B.10})$$

$$k_s = i \frac{\omega}{c_s} \quad (\text{B.11})$$

$$c_p = \sqrt{\frac{\lambda + 2\mu}{\rho}} \quad (\text{B.12})$$

$$c_s = \sqrt{\frac{\mu}{\rho}} \quad (\text{B.13})$$

where c_p and c_s are the pressure respectively shear wave velocity in the soil.

However, it is important to mention that also different Green's functions could be used, for instance those for the case of a point load in an elastic half-space [2]. The advantage is that, e.g. for the case of a structural foundation, only the interface between the soil and the foundation has to be discretized. When full-space Green's functions are used, discretization of the free surface is also required. The major drawback of the former is that the calculation of these half-space Green's functions requires complex numerical integrations and are difficult to evaluate accurately [46]. Therefore, a BE formulation based on full-space Green's functions is used throughout this dissertation.

B.4 The boundary integral equations

Reconsider the reciprocal theorem (B.4). The first state is chosen to be problem of interest, and $\mathbf{b} = \mathbf{0}$ is assumed (Figure B.1(a)). The body forces can be ignored because only vibration about an equilibrium position is of interest. The second state is assumed to be the fundamental solution corresponding to a body force defined by Eq. (B.5). In order to apply the reciprocal theorem, both states must be defined for the same body, and therefore it is assumed that Ω is part of the infinite domain [46]. Using the well-known property of the Dirac function, Eq. (B.4) becomes:

$$\mathbf{u}^i + \int_{\Gamma} \mathbf{p}^* \mathbf{u} d\Gamma = \int_{\Gamma} \mathbf{u}^* \mathbf{p} d\Gamma \quad (\text{B.14})$$

Eq. (B.14) is the integral representation of the displacement \mathbf{u}^i at any point of the body Ω , in terms of the boundary values \mathbf{u} and \mathbf{p} and the known fundamental solution \mathbf{u}^* and \mathbf{p}^* . \mathbf{u} and \mathbf{p} are 3×1 vectors, while \mathbf{u}^* and \mathbf{p}^* are 3×3 matrices.

Because Eq. (B.14) is valid for all points of Ω , including those on Γ , the governing equations of the problem may be represented as a system of boundary integral equations (BIE). However, when the source point \mathbf{i} is located on the boundary, the integrals have a singularity (as the fundamental solution becomes singular for $r = 0$). In order to obtain the BIE, one need to extend the boundary with Γ_ε , formed by a hemisphere with center at \mathbf{i} and a small radius ε . Afterwards, this radius has to be taken to the limit, i.e. $\varepsilon \rightarrow 0$, and the behaviour of the boundary integrals in Eq. (B.14) can be investigated.

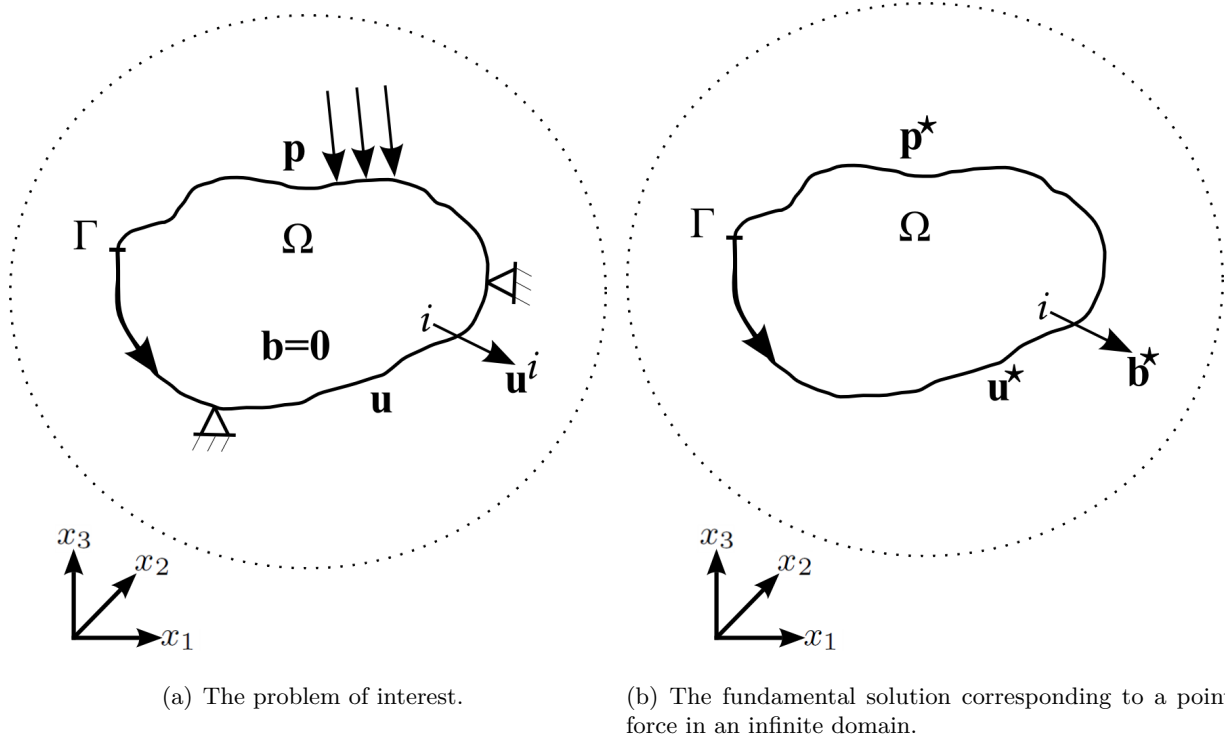


Figure B.1: Two elastodynamic states of the body Ω . The infinite domain is represented by the dashed circle [46].

More details of this limiting process may be found in [6] and [13]. As a result, when the boundary Γ is smooth, Eq. (B.14) can be written as:

$$\frac{1}{2}\mathbf{u}^i + \int_{\Gamma} \mathbf{p}^* \mathbf{u} d\Gamma = \int_{\Gamma} \mathbf{u}^* \mathbf{p} d\Gamma \tag{B.15}$$

B.5 Numerical solution

Solving the boundary integral equation (B.15) would solve the boundary value problem. In general, an analytical solution is not possible. It can only be approximated by a numerical method. The boundary Γ is divided into N elements, and each element is defined by some nodal points. The field variables over the element are written in terms of their nodal values:

$$\mathbf{u} \simeq \Phi \mathbf{u}^j \tag{B.16}$$

$$\mathbf{p} \simeq \Phi \mathbf{p}^j \tag{B.17}$$

with Φ the shape functions considered and \mathbf{u}^j and \mathbf{p}^j the nodal values. Throughout this dissertation, elements with constant shape functions are used. This means that there is only one node per element, i.e. at the center of each element. Hence, Φ reduces to \mathbf{I} .

Introducing Eqs. (B.16) and (B.17) into Eq. (B.15), and taking \mathbf{u} and \mathbf{p} outside of the integrals, results in following expression:

$$\frac{1}{2}\mathbf{u}^i + \sum_{j=1}^N \left(\int_{\Gamma_j} \mathbf{p}^* d\Gamma \right) \mathbf{u}^j = \sum_{j=1}^N \left(\int_{\Gamma_j} \mathbf{u}^* d\Gamma \right) \mathbf{p}^j \quad (\text{B.18})$$

The point force of the fundamental solution may be applied at each of the N nodes, which produces a system of N linearly independent algebraic equations:

$$\sum_{j=1}^N \mathbf{H}^{ij} \mathbf{u}^j = \sum_{j=1}^N \mathbf{G}^{ij} \mathbf{p}^j \quad \text{for } i = 1 \dots N \quad (\text{B.19})$$

with

$$\mathbf{H}^{ij} = \int_{\Gamma_j} \mathbf{p}^* d\Gamma \quad \text{if } i \neq j \quad (\text{B.20})$$

$$= \int_{\Gamma_j} \mathbf{p}^* d\Gamma + \frac{1}{2}\mathbf{I} \quad \text{if } i = j \quad (\text{B.21})$$

$$\mathbf{G}^{ij} = \int_{\Gamma_j} \mathbf{u}^* d\Gamma \quad (\text{B.22})$$

The system of equations (B.19) can be written in matrix form as:

$$\mathbf{H}\mathbf{U} = \mathbf{G}\mathbf{P} \quad (\text{B.23})$$

\mathbf{H} and \mathbf{G} are $3N \times 3N$ matrices, while \mathbf{U} and \mathbf{P} are $3N \times 1$ vectors. The computation of the so-called influence coefficients \mathbf{H}^{ij} and \mathbf{G}^{ij} requires integration of the fundamental solution over each element j . In some cases, these calculations can be performed analytically, but most of the times, numerical integration is the only possible approach.

When $i \neq j$ (i.e. when the point force is lying outside the integration element), the standard Gauss-Legendre quadrature is used. In order to use the standard formula, a transformation to the intrinsic coordinates ξ_1 and ξ_2 is required (Figure B.2). This transformation implies the use of the determinant $|J|$ of the Jacobian matrix J , which is defined by Eq. (B.24):

$$[J] = \begin{bmatrix} \frac{\partial \xi_1}{\partial x_1} & \frac{\partial \xi_1}{\partial x_2} & \frac{\partial \xi_1}{\partial x_3} \\ \frac{\partial \xi_2}{\partial x_1} & \frac{\partial \xi_2}{\partial x_2} & \frac{\partial \xi_2}{\partial x_3} \\ \frac{\partial \xi_3}{\partial x_1} & \frac{\partial \xi_3}{\partial x_2} & \frac{\partial \xi_3}{\partial x_3} \end{bmatrix} \quad (\text{B.24})$$

For example, \mathbf{G}^{ij} can be computed as follows:

$$\mathbf{G}^{ij} = \int_{\Gamma_j} \mathbf{u}^* d\Gamma = \int_{-1}^1 \int_{-1}^1 \mathbf{u}^* |J| d\xi_1 d\xi_2 \simeq \sum_{n=1}^{n_G} \sum_{m=1}^{n_G} \mathbf{u}^*(\xi_n, \xi_m) |J| w_n w_m \quad (\text{B.25})$$

where n_G is the number of Gauss points taken into account, ξ_n and ξ_m are the abscissae and w_n and w_m the corresponding weighting factors. All calculations in this dissertation have been done using six Gauss points.

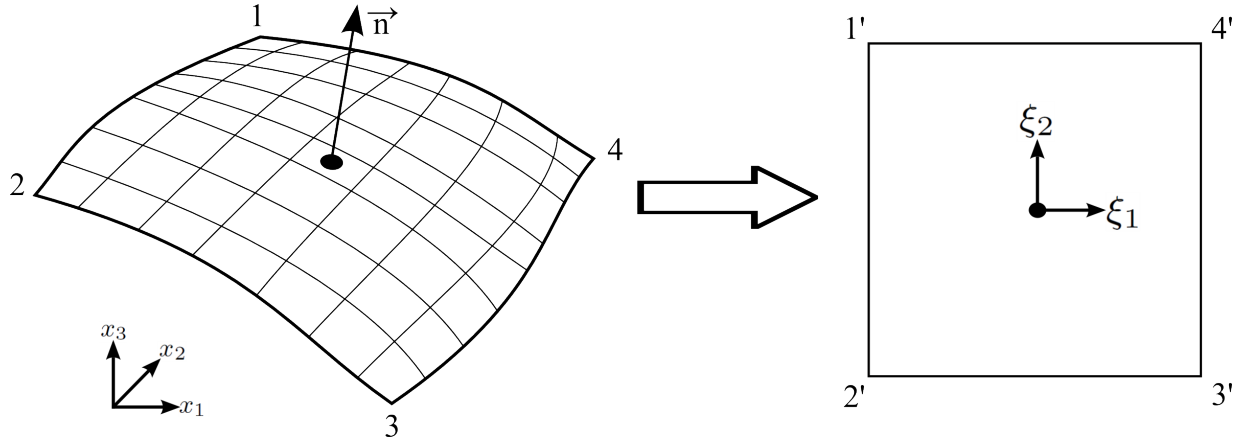


Figure B.2: Transformation from the global coordinate system (x_1, x_2, x_3) to the intrinsic coordinates (ξ_1, ξ_2) .

When $i = j$ (i.e. when the point force is lying inside the integration element), the integration element contains the singularity of the fundamental solution. As rectangular elements are used, the computation of \mathbf{H}^{ii} is simple [13]: $\mathbf{H}^{ii} = \frac{1}{2}\mathbf{I}$. If non-rectangular elements are used, the static rigid body displacement has to be considered.

The computation of \mathbf{G}^{ii} is undertaken using the element subdivision proposed by Lachat [29]. The element is divided into four triangular sub-elements, and each sub-element is treated as a quadrilateral domain for which two corners coincide at the central node of the element. Using this approach, the singularity in \mathbf{u}^* (which is of the type $1/r$ for $r \rightarrow 0$) is cancelled out by the Jacobian determinant $|J|$ that has a zero of type r at the collocation point. Therefore, integration over each sub-element may be undertaken using the standard Gauss-Legendre quadrature.

In order to finally solve the problem, the boundary conditions have to be taken into account. In general, at some nodes the displacements are unknown, and at other nodes, the tractions are unknown. The system of equations (B.23) is rearranged in the following form:

$$\mathbf{A}\mathbf{X} = \mathbf{F} \tag{B.26}$$

This system of equations can be solved using a standard equation solving technique; however, the matrices are fully-populated and non-symmetric, and therefore the solution techniques used in the FE method cannot be used.

Once the unknowns on the boundary Γ are calculated, Eq. (B.14) can be used to obtain the values of \mathbf{u} at any internal point of the domain Ω (strains and stresses can be obtained by means of the well-known strain-displacement and stress-strain relationships). An advantage of the BE method is that one only needs to calculate the field variables at the internal points of interest.

Appendix D

The Pipe-in-Pipe model for underground railways

In chapter 7, the Pipe-in-Pipe model (PiP) [38] is used to calculate the response of piled foundations to ground-borne, underground railway induced vibrations. In fact, a modified version of PiP that accounts for a free surface is utilized, as the original PiP model only models a tunnel in a full-space. The aim of this appendix is to summarize the principles and assumptions of the modified PiP model, which have been introduced by Forrest [14], Hussein [21] and Rikse [40].

The theory of the original PiP model is discussed in section D.1. The incorporation of a free surface is explained in section D.2. The model is slightly extended in order to obtain the stresses in the soil.

D.1 The original PiP model for a tunnel in a full-space

The original PiP model is a computationally efficient semi-analytical insertion gain model. It accounts for the three-dimensional dynamic interaction between the track, the tunnel and the soil. The system is assumed to be invariant in the longitudinal direction of the tunnel, and therefore the analysis can be carried out in the wavenumber-frequency domain. This results in a two-and-a-half-dimensional model.

The model consists of four main components:

a. **Tunnel**

The tunnel is modelled as an infinitely long pipe. The elastic continuum equations in cylindrical coordinates are used to model the behaviour of the tunnel. Thin shell theory can also be used if the tunnel wall thickness is small compared to the mean radius of the tunnel, but the reduction in computation time is negligible.

b. **Soil**

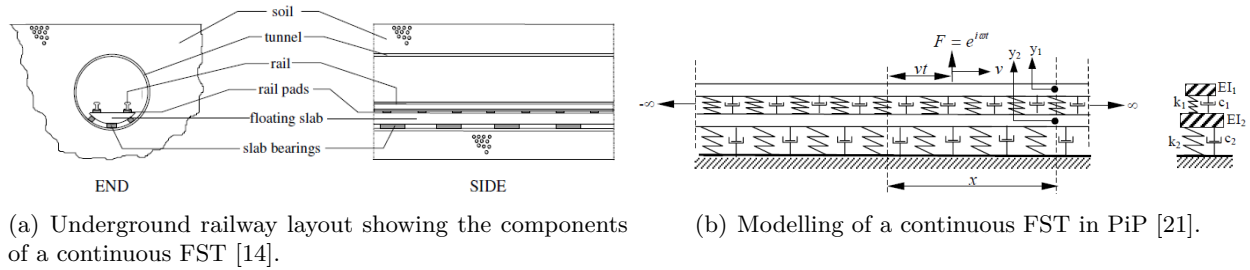
The soil is also modelled as an infinitely long pipe, with an infinite outer radius and an inner radius equal to the radius of the tunnel. Again, elastic continuum equations in cylindrical coordinates are used.

c. Track

The two rails of the track are mounted via rail pads on a floating slab track (FST), which rests on slab bearings supported by the tunnel invert. The slab may be continuous (Figure D.1) or may be constructed of a number of discrete pre-cast sections.

d. Train

As the vibrations are generated by dynamic interaction between the wheels and the rails due to wheel and rail unevenness, the model should take this interaction into account. The train is represented by axle masses located at regular intervals. Only the unsprung mass of the train is considered.



(a) Underground railway layout showing the components of a continuous FST [14].

(b) Modelling of a continuous FST in PiP [21].

Figure D.1: Continuous floating slab track (FST).

D.1.1 Modelling the track and train

The rails as well as the slab are modelled as Euler-Bernoulli beams on an elastic foundation. The upper beam accounts for both of the rails, which implies that a perfect unevenness correlation between the two rails is assumed (Figure D.1(b)). For long wavelengths (i.e. low frequencies), this assumption can be justified, e.g. due to the variation of the bed stiffness along the track. A perfect correlation is however not observed for short wavelengths.

The rail unevenness is modelled as a displacement input δ . The inertia of the axle masses m_a gives rise to dynamic forces working on the rail. The slab and rail beams and the train are assumed to be infinitely long. If the response at a point in the soil has to be determined, the contributions of all the axles has to be taken into account. Due to the infinite character of the model and the regular spacing between the axles, the shifting principle can be used (Figure D.2): the response in the soil at $x = 0$ due to a set of loads at various positions on the rail is identical to the sum of the responses at those various positions in the soil due to a single load at $x = 0$ [14]. In practice, only a finite number of axles should be included, until convergence has been reached.

Throughout this dissertation, a white noise unevenness input spectrum is used ($S_0(f) = 1 \text{ mm}^2/\text{Hz}$), which results in an equal weighting of all frequencies. This is of course unrealistic, but if insertion gain (IG) is of concern, the input spectrum has no importance. If ultimately the vibration levels induced by actual rail unevenness are desired, a more realistic input spectrum can be used, see e.g. Frederick [16].

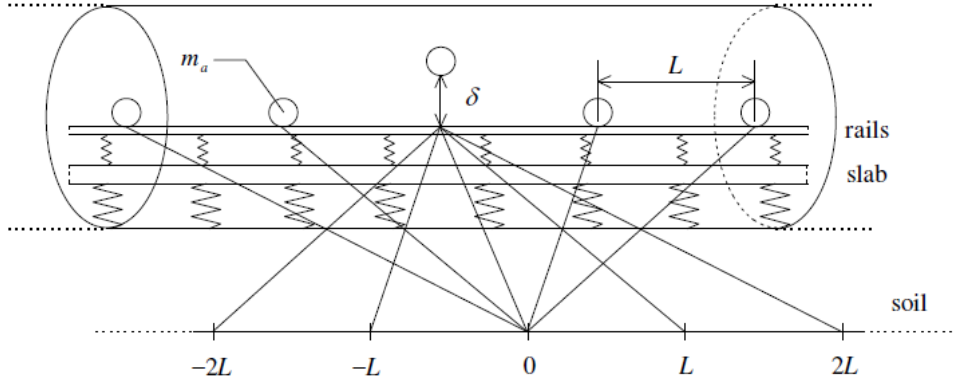


Figure D.2: Illustration of the shifting principle [14].

D.1.2 Elastic continuum equations

Both tunnel and soil are assumed to behave as a three-dimensional, homogeneous, isotropic elastic continuum. The wave equation describing motion within this continuum is given by Eq. (D.1) [18]:

$$\mu \nabla^2 \mathbf{u} + (\lambda + \mu) \nabla \nabla \cdot \mathbf{u} + \rho \mathbf{b} = \rho \ddot{\mathbf{u}} \quad (\text{D.1})$$

As already mentioned in section B.1, \mathbf{u} is the displacement vector at a point \mathbf{x} , \mathbf{b} is the vector of body forces, and ρ is the density of the solid. λ and μ are Lamé constants and can be related to the more common material parameters E , G and ν as follows: $\lambda = 2\nu G / (1 - 2\nu)$ and $\mu = G = E / (2(1 + \nu))$. The body forces $\rho \mathbf{b}$ will be ignored, as the only body forces acting are due to gravity and only vibration about an equilibrium position is of interest. Since the problem has a cylindrical geometry, it will be formulated in a cylindrical coordinate system, as illustrated in Figure D.3.

A solution of Eq. (D.1) can be obtained by making use of the Helmholtz decomposition of the displacement vector \mathbf{u} :

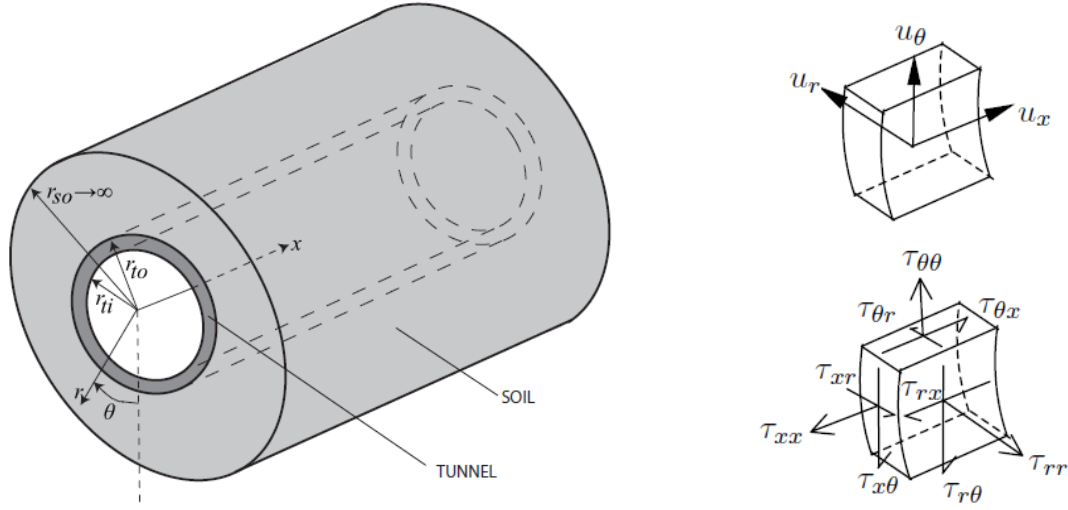
$$\mathbf{u} = \nabla \phi + \nabla \times \mathbf{H} \quad (\text{D.2})$$

with ϕ and \mathbf{H} scalar respectively vector Lamé potentials. It can be proven that the displacement equations (D.1) are fulfilled if the Lamé potentials satisfy following equations:

$$\nabla^2 \phi = \frac{1}{c_p^2} \frac{\partial^2 \phi}{\partial t^2} \quad (\text{D.3})$$

$$\nabla^2 \mathbf{H} = \frac{1}{c_s^2} \frac{\partial^2 \mathbf{H}}{\partial t^2} \quad (\text{D.4})$$

where $c_p = \sqrt{(\lambda + 2\mu)/\rho}$ is the speed of the pressure waves and $c_s = \sqrt{\mu/\rho}$ is the speed of shear waves.



(a) Components of the PiP model (the track and train are not shown)[40]. (b) Cylindrical coordinate system and displacement and stress vectors [21].

Figure D.3: (a) Components of the PiP model, and (b) the displacement and stress vectors.

An expression of the potentials, based on the separation of variables, is proposed:

$$\phi = f(r) \cos(n\theta) e^{i(\omega t + \xi x)} \quad (\text{D.5})$$

$$H_r = g_r(r) \sin(n\theta) e^{i(\omega t + \xi x)} \quad (\text{D.6})$$

$$H_\theta = g_\theta(r) \cos(n\theta) e^{i(\omega t + \xi x)} \quad (\text{D.7})$$

$$H_x = g_x(r) \sin(n\theta) e^{i(\omega t + \xi x)} \quad (\text{D.8})$$

Substituting Eqs. (D.5)–(D.8) into Eqs. (D.3)–(D.4) and making use of the definitions of the Laplacians $\nabla^2 \phi$ and $\nabla^2 \mathbf{H}$ for cylindrical coordinates results in a set of four differential equations. Solutions for the functions f , g_r , g_θ and g_x can be deduced from this set of equations (see Forrest [14] for more details):

$$f(r) = AI_n(\alpha r) + BK_n(\alpha r) \quad (\text{D.9})$$

$$g_r(r) = -g_\theta(r) = A_r I_{n+1}(\beta r) + B_r K_{n+1}(\beta r) \quad (\text{D.10})$$

$$g_x(r) = A_x I_n(\beta r) + B_x K_n(\beta r) \quad (\text{D.11})$$

where $\alpha^2 = \xi^2 - \omega^2/c_p^2$, $\beta^2 = \xi^2 - \omega^2/c_s^2$ and I_n and K_n are modified Bessel functions of the first respectively the second kind of order n . The coefficients A , B , A_r , B_r , A_x and B_x are arbitrary constants, to be determined from the appropriate boundary conditions.

Expressions for the displacement field \mathbf{u} can finally be obtained by introducing the Lamé potentials (D.5)–(D.8) into the Helmholtz decomposition (D.2), taking the solutions (D.9)–(D.11) into account. From the displacement field, the elastic strains in cylindrical coordinates can be derived, and hence

the stresses by means of the general stress-strain relationship (Hooke's law). The solutions can then be written in following matrix form:

$$\mathbf{u} = \begin{Bmatrix} u_r \\ u_\theta \\ u_x \end{Bmatrix} = [\mathbf{S}][\mathbf{U}]\mathbf{C}e^{i(\omega t + \xi x)} \quad (\text{D.12})$$

$$\boldsymbol{\tau} = \begin{Bmatrix} \tau_{rr} \\ \tau_{r\theta} \\ \tau_{rx} \\ \tau_{\theta\theta} \\ \tau_{\theta x} \\ \tau_{xx} \end{Bmatrix} = \begin{bmatrix} \mathbf{S} & 0 \\ 0 & \mathbf{S} \end{bmatrix} [\mathbf{T}]\mathbf{C}e^{i(\omega t + \xi x)} \quad (\text{D.13})$$

$$\text{with } \mathbf{S} = \begin{bmatrix} \cos n\theta & 0 & 0 \\ 0 & \sin n\theta & 0 \\ 0 & 0 & \cos n\theta \end{bmatrix} \quad (\text{D.14})$$

The trigonometric terms in $[\mathbf{S}]$ physically represent circumferential ring modes of the cylindrical tunnel. They consist of in-plane flexural modes associated with u_r , in-plane extensional modes associated with u_θ and out-of-plane flexural modes associated with u_x . The vector $\mathbf{C} = \{A \ B \ A_r \ B_r \ A_x \ B_x\}^T$ contains the unknown coefficients, to be determined from the appropriate boundary conditions. The elements of the matrix $[\mathbf{U}]$, defining displacements, and the matrix $[\mathbf{T}]$, defining stresses, are given by Forrest [14]. They are all function of the wavenumber ξ , the angular frequency ω , the circumferential mode number n , the radius r and the material properties.

Finally, the modal displacements and surface stresses can be written as follows:

$$\tilde{\mathbf{u}} = \begin{Bmatrix} \tilde{u}_r \\ \tilde{u}_\theta \\ \tilde{u}_x \end{Bmatrix} = [\mathbf{U}]\mathbf{C} \quad (\text{D.15})$$

$$\tilde{\boldsymbol{\tau}} = \begin{Bmatrix} \tilde{\tau}_{rr} \\ \tilde{\tau}_{r\theta} \\ \tilde{\tau}_{rx} \end{Bmatrix} = [\mathbf{T}_r]\mathbf{C} \quad (\text{D.16})$$

Only surface stresses are retained, as only these stresses are important for the boundary conditions. The 3×6 matrix $[\mathbf{T}_r]$ is the top half of the 6×6 matrix $[\mathbf{T}]$.

D.1.3 Modelling the tunnel

The tunnel is modelled as a thick cylindrical shell by means of the elastic continuum equations presented above. The inner and outer radius of the tunnel are denoted as r_{ti} and r_{to} respectively. Stresses $\tilde{\mathbf{q}}$ are applied at the inner surface of the tunnel, while stresses $\tilde{\boldsymbol{\tau}}_{to}$ are induced at the outer surface of the tunnel. They cause the displacements $\tilde{\mathbf{u}}_{ti}$ and $\tilde{\mathbf{u}}_{to}$ at inner and outer surfaces of the

tunnel wall. Based on Eq. (D.15) and Eq. (D.16), following relations hold:

$$\tilde{\mathbf{q}} = [\mathbf{T}_{\mathbf{r}}]_{r=r_{ti}} \mathbf{C} \quad (\text{D.17})$$

$$\tilde{\mathbf{u}}_{ti} = [\mathbf{U}]_{r=r_{ti}} \mathbf{C} \quad (\text{D.18})$$

$$\tilde{\boldsymbol{\tau}}_{to} = [\mathbf{T}_{\mathbf{r}}]_{r=r_{to}} \mathbf{C} \quad (\text{D.19})$$

$$\tilde{\mathbf{u}}_{to} = [\mathbf{U}]_{r=r_{to}} \mathbf{C} \quad (\text{D.20})$$

D.1.4 Modelling the soil

As mentioned before, the soil is modelled as a thick shell with an inner radius r_{si} equal to the outer radius r_{to} of the tunnel, and an outer radius $r_{so} = \infty$. The radiation condition has to be fulfilled, and this gives the opportunity to reduce the dimensions of the set of equations (D.15)–(D.16). The matrices $[\mathbf{U}]$ and $[\mathbf{T}_{\mathbf{r}}]$ contain modified Bessel functions of the first as well as the second kind. Only those of the second kind K_n decay for all arguments as r goes to infinity. Hence, the coefficients associated with the modified Bessel functions of the first kind I_n must be set to zero in order to satisfy the radiation condition:

$$\mathbf{C} = \left\{ 0 \quad B \quad 0 \quad B_r \quad 0 \quad B_x \right\}^T \quad (\text{D.21})$$

Stresses $\tilde{\boldsymbol{\tau}}_{si}$ and displacements $\tilde{\mathbf{u}}_{si}$ are induced at the tunnel-soil interface. From Eqs. (D.15), (D.16) and (D.21):

$$\tilde{\boldsymbol{\tau}}_{si} = [\mathbf{T}_{\mathbf{r}}^*]_{r=r_{si}} \mathbf{G} \quad (\text{D.22})$$

$$\tilde{\mathbf{u}}_{si} = [\mathbf{U}^*]_{r=r_{si}} \mathbf{G} \quad (\text{D.23})$$

The matrices $[\mathbf{T}_{\mathbf{r}}^*]$ and $[\mathbf{U}^*]$ contain the second, fourth and sixth column of $[\mathbf{T}_{\mathbf{r}}]$ respectively $[\mathbf{U}]$, while the vector \mathbf{G} contains the non-zero elements of \mathbf{C} .

D.1.5 Coupling the tunnel and the soil

Coupling between the tunnel and the soil can be achieved by imposing compatibility of displacements and equilibrium of forces at the tunnel-soil interface. This can be expressed as follows:

$$\tilde{\mathbf{u}}_{to} = \tilde{\mathbf{u}}_{si} \quad (\text{D.24})$$

$$\tilde{\boldsymbol{\tau}}_{to} = \tilde{\boldsymbol{\tau}}_{si} \quad (\text{D.25})$$

These extra equations can be used to solve the set of equations (D.17)–(D.20) and (D.22)–(D.23):

$$\mathbf{C} = \left[\begin{array}{c} [\mathbf{T}_{\mathbf{r}}]_{r=r_{ti}} \\ [\mathbf{T}_{\mathbf{r}}]_{r=r_{to}} - [\mathbf{T}_{\mathbf{r}}^*]_{r=r_{si}} [\mathbf{U}^*]_{r=r_{si}}^{-1} [\mathbf{U}]_{r=r_{to}} \end{array} \right]^{-1} \begin{Bmatrix} \tilde{\mathbf{q}} \\ \mathbf{0} \end{Bmatrix} \quad (\text{D.26})$$

$$\mathbf{G} = [\mathbf{U}^*]_{r=r_{si}}^{-1} [\mathbf{U}]_{r=r_{to}} \mathbf{C} \quad (\text{D.27})$$

where $\mathbf{0}$ is a 3×1 vector of zeros. Once \mathbf{G} is calculated, stresses and displacements at any radius R in the soil can be obtained by means of following relations:

$$\tilde{\boldsymbol{\tau}}_{sR} = [\mathbf{T}_{\mathbf{r}}^*]_{r=R} \mathbf{G} \quad (\text{D.28})$$

$$\tilde{\mathbf{u}}_{sR} = [\mathbf{U}^*]_{r=R} \mathbf{G} \quad (\text{D.29})$$

D.2 The modified PiP model for a tunnel in a half-space

In order to account for the existence of a free surface, a modified version of the PiP model has been developed [23]. In this version, the key assumption is that the near-field displacements are not influenced by the presence of the free surface. It consists of three main steps (Figure D.4):

1. Calculation of the displacements at the tunnel-soil interface by means of the original PiP model for a tunnel embedded in a full-space.
2. The use of Green's functions for a two-and-a-half-dimensional full-space to calculate an equivalent internal source in a full-space that produces the same displacements at the tunnel-soil interface as those obtained in 1.
3. Calculation of the far-field displacements induced by the equivalent internal source in a half-space by means of the appropriate Green's functions.

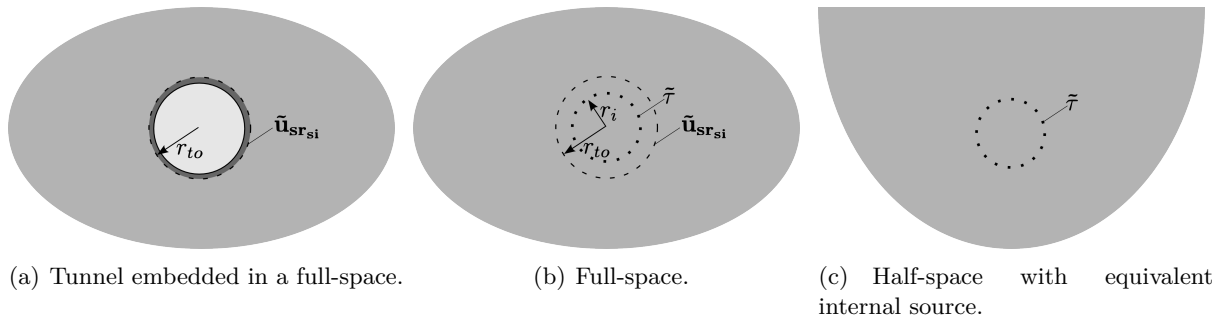


Figure D.4: The methodology of the modified PiP model.

D.2.1 Displacements at the tunnel-soil interface

Eqs. (D.28) and (D.29) can be used to calculate stresses and displacements at any radius R in the soil for a tunnel embedded in a full-space. For the special case $R = r_{to} = r_{si}$, stresses and displacements at the tunnel-soil interface become:

$$\tilde{\boldsymbol{\tau}}_{sr_{si}} = [\mathbf{T}_{\mathbf{r}}^*]_{r=r_{si}} \mathbf{G} \quad (\text{D.30})$$

$$\tilde{\mathbf{u}}_{sr_{si}} = [\mathbf{U}^*]_{r=r_{si}} \mathbf{G} \quad (\text{D.31})$$

D.2.2 The equivalent internal source

The second step in the modified PiP model is the calculation of the equivalent internal source which produces the same displacements $\tilde{\mathbf{u}}_{\text{sr}_{si}}$ in a full-space. The internal source consists of M line loads located on a virtual cylinder of radius r_i , as illustrated in Figure D.4(b), and these can be expressed as $\mathbf{F}_j = \tilde{\mathbf{F}}_j e^{i(\omega t + \xi x)}$ ($j = 1 \dots M$). It has been demonstrated by Rikse [40] that the radius r_i of the virtual cylinder has to be smaller than the outer radius r_{to} of the tunnel in order to produce the correct far-field displacements.

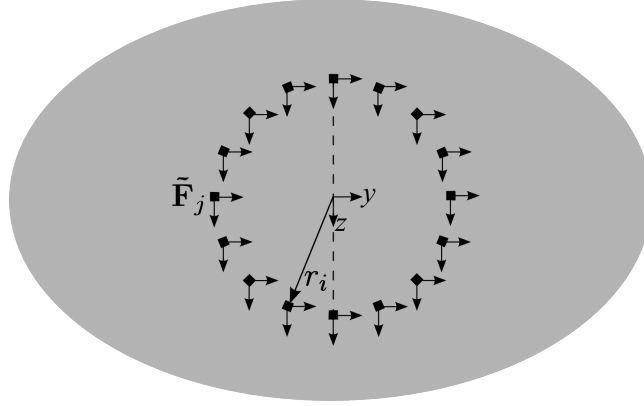


Figure D.5: The equivalent internal source is represented by M line loads $\tilde{\mathbf{F}}_j$ along a virtual cylinder with radius r_i .

A way to calculate the internal source is to use the analytical expressions for the two-and-a-half-dimensional Green's functions for a full-space obtained by Tadeu and Kausel [44]. This way of working has been presented by Hussein in [23]. However, an alternative method to calculate the Green's functions for a full-space has been implemented in the MATLAB code. This formulation comprises two submodels:

- A thick shell with an inner radius equal to r_i and an outer radius equal to infinity. This represents a full-space with a cylindrical cavity.
- A solid cylinder with radius r_i .

Both submodels are modelled by means of the elastic continuum equations of paragraph D.1.2. The dimensions of the second subproblem can be reduced by considering the fact that the modified Bessel functions of the second kind K_n tends to infinity as r goes to zero. Therefore, the coefficients associated with these Bessel functions must be set to zero. Incorporating compatibility of displacements at $r = r_i$ results in an expression for the equivalent internal source $\tilde{\boldsymbol{\tau}}$:

$$\tilde{\boldsymbol{\tau}} = \left([\mathbf{T}'_{\mathbf{r}}]_{r=r_i} - [\mathbf{T}'_{\mathbf{r}}]_{r=r_i} [\mathbf{U}'_{\mathbf{r}}]_{r=r_i}^{-1} [\mathbf{U}'_{\mathbf{r}}]_{r=r_i} \right) \mathbf{G} \quad (\text{D.32})$$

The matrices $[\mathbf{T}'_{\mathbf{r}}]$ and $[\mathbf{U}'_{\mathbf{r}}]$ contain the first, third and fifth column of $[\mathbf{T}_{\mathbf{r}}]$ respectively $[\mathbf{U}]$. A more detailed description of this alternative method can be found in [40]. From the internal source $\tilde{\boldsymbol{\tau}}$,

expressions for the M line loads $\tilde{\mathbf{F}}_j$ can be obtained. Only $M/2 + 1$ line loads on the left-hand side of the virtual cylinder have to be calculated, as symmetry can be used. It should be noted that the calculation of the internal source could also be performed by means of two-and-a-half-dimensional Green's functions for a half-space. However, analytical expressions for these functions are not available, and hence numerical integrations are required. Therefore, in order to maintain the numerical efficiency of the model, it is chosen to work with full-space functions by assuming that the free surface is sufficiently far from the tunnel so as not to have a significant influence on the near-field calculations [23].

Up to this point, the line loads $\tilde{\mathbf{F}}_j$ are expressed in the wavenumber - spatial domain (for the longitudinal coordinate x and the horizontal coordinate y respectively). As the two-and-a-half-dimensional Green's functions for a half-space which, will be used in paragraph D.2.3, are formulated in the wavenumber - wavenumber domain, a Fourier transformation of the line loads $\tilde{\mathbf{F}}_j$ is required. The expression in the wavenumber - spatial domain for the longitudinal component of $\tilde{\mathbf{F}}_j$ reads as follows (based on the right-handed Cartesian coordinate system presented in Figure D.5):

$$F_{jx}(\xi, y) = F_{jx}(\xi)(\delta(y - r_i \sin \theta) + \delta(y + r_i \sin \theta)) \quad (\text{D.33})$$

Using the definition presented in section A.2, and taking benefit from symmetry gives:

$$\tilde{F}_{jx}(\xi, \gamma) = \int_{-\infty}^{+\infty} F_{jx}(\xi, y)e^{-i\gamma y} dy = F_{jx}(\xi) \left(e^{-i\gamma r_i \sin \theta} + e^{i\gamma r_i \sin \theta} \right) \quad (\text{D.34})$$

$$= 2F_{jx}(\xi) \cos(\gamma r_i \sin \theta) \quad (\text{D.35})$$

Similar expressions for the horizontal and vertical component of $\tilde{\mathbf{F}}_j$ can be obtained:

$$\tilde{F}_{jy}(\xi, \gamma) = 2iF_{jy}(\xi) \sin(\gamma r_i \sin \theta) \quad (\text{D.36})$$

$$\tilde{F}_{jz}(\xi, \gamma) = 2F_{jz}(\xi) \cos(\gamma r_i \sin \theta) \quad (\text{D.37})$$

For the special case of $\theta = 0$ and $\theta = \pi$, the forces have to be divided by two.

D.2.3 The far-field displacements

In the final step of the modified PiP model, the line loads $\tilde{\mathbf{F}}_j$ are applied in a half-space. Green's functions for a two-and-a-half-dimensional half-space $\tilde{\mathbf{G}}^{\text{half}}$, presented by Tadeu [45], are used to obtain the far-field displacements:

$$\mathbf{u} = \tilde{\mathbf{u}}e^{i(\omega t + \xi x + \gamma y)} = \tilde{\mathbf{G}}^{\text{half}} \tilde{\mathbf{F}}e^{i(\omega t + \xi x + \gamma y)} \quad (\text{D.38})$$

The calculation of the half-space Green's functions requires numerical integrations, as no analytical expressions are available. Attention has to be paid to the wavenumber sampling when performing these integrations ([23], [40]). Moreover, caution has to be paid to the implementation in MATLAB, as Tadeu uses a different coordinate system and a different definition of the Fourier transform with respect to the spatial coordinate than the PiP model. The major differences are summarized in Table D.1.

The modified PiP model in its current formulation can only be used to calculate the displacements \mathbf{u} in the soil. However, it is also necessary to obtain the stresses $\boldsymbol{\sigma}$ in the soil:

$$\boldsymbol{\sigma} = \tilde{\boldsymbol{\sigma}}e^{i(\omega t + \xi x + \gamma y)} = \tilde{\mathbf{G}}_{\boldsymbol{\sigma}}^{\text{half}} \tilde{\mathbf{F}}e^{i(\omega t + \xi x + \gamma y)} \quad (\text{D.39})$$

	Tadeu	PiP
Coordinate system	Left-handed	Right-handed
Longitudinal coordinate	x	x
Vertical coordinate	y	z
Horizontal coordinate	z	y
Fourier transformation w.r.t. a spatial coordinate	$F(\xi) = \int_{-\infty}^{+\infty} f(x)e^{i\xi x} dx$	$F(\xi) = \int_{-\infty}^{+\infty} f(x)e^{-i\xi x} dx$

Table D.1: Differences in definitions between Tadeu and PiP.

Eq. (D.39) requires the two-and-a-half-dimensional half-space Green's functions $\tilde{\mathbf{G}}_{\sigma}^{\text{half}}$ for stresses. These functions can easily be found by means of the well-known equations relating displacements, strains and stresses:

$$\varepsilon_{ij} = \frac{1}{2} \left(\frac{\partial u_i}{\partial x_j} + \frac{\partial u_j}{\partial x_i} \right) \quad (\text{D.40})$$

$$\sigma_{ij} = \lambda \varepsilon_{\text{vol}} \delta_{ij} + 2\mu \varepsilon_{ij} \quad (\text{D.41})$$

where $\varepsilon_{\text{vol}} = \varepsilon_{xx} + \varepsilon_{yy} + \varepsilon_{zz}$ and δ_{ij} is the Kronecker delta. λ and μ are the Lamé constants of the soil.

Derivation of the displacement Green's functions results in lengthy expressions which are summarized here. The definitions of Tadeu (as presented in Table D.1) are used:

$$\frac{\partial G_{xx}(k_n, k_z)}{\partial x} = -ik_n G_{xx}(k_n, k_z) \quad (\text{D.42})$$

$$\frac{\partial G_{yx}(k_n, k_z)}{\partial y} = \frac{k_n}{2\rho\omega^2} \left(-\nu_n(E_b + A_n^x E_{b0}) + \gamma_n(E_c + C_n^x E_{c0}) \right) \quad (\text{D.43})$$

$$\frac{\partial G_{zx}(k_n, k_z)}{\partial z} = -ik_z G_{zx}(k_n, k_z) \quad (\text{D.44})$$

$$\begin{aligned} \frac{\partial G_{xx}(k_n, k_z)}{\partial y} = & \frac{-1}{2\rho\omega^2} \left(k_n^2 (\text{sgn}(y - y_0) E_b + A_n^x E_{b0}) \dots \right. \\ & \left. + (\gamma_n^2 + k_z^2) \text{sgn}(y - y_0) E_c + (\gamma_n^2 C_n^x + k_z^2 B_n^x) E_{c0} \right) \quad (\text{D.45}) \end{aligned}$$

$$\frac{\partial G_{yx}(k_n, k_z)}{\partial x} = -ik_n G_{yx}(k_n, k_z) \quad (\text{D.46})$$

$$\frac{\partial G_{yx}(k_n, k_z)}{\partial z} = -ik_z G_{yx}(k_n, k_z) \quad (\text{D.47})$$

$$\frac{\partial G_{zx}(k_n, k_z)}{\partial y} = \frac{k_n k_z}{2\rho\omega^2} \left(\text{sgn}(y - y_0) (-E_b + E_c) - A_n^x E_{b0} + B_n^x E_{c0} \right) \quad (\text{D.48})$$

$$\frac{\partial G_{zx}(k_n, k_z)}{\partial x} = -ik_n G_{zx}(k_n, k_z) \quad (\text{D.49})$$

$$\frac{\partial G_{xx}(k_n, k_z)}{\partial z} = -ik_z G_{xx}(k_n, k_z) \quad (\text{D.50})$$

$$\frac{\partial G_{xy}(k_n, k_z)}{\partial x} = -ik_n G_{xy}(k_n, k_z) \quad (\text{D.51})$$

$$\begin{aligned} \frac{\partial G_{yy}(k_n, k_z)}{\partial y} = \frac{-1}{2\rho\omega^2} & \left(\nu_n^2 (\text{sgn}(y - y_0)E_b + A_n^y E_{b0}) \dots \right. \\ & \left. - \nu_{zn}^2 \text{sgn}(y - y_0)E_c + (k_n^2 B_n^y + k_z^2 C_n^y) E_{c0} \right) \end{aligned} \quad (\text{D.52})$$

$$\frac{\partial G_{zy}(k_n, k_z)}{\partial z} = -ik_z G_{zy}(k_n, k_z) \quad (\text{D.53})$$

$$\frac{\partial G_{xy}(k_n, k_z)}{\partial y} = \frac{k_n}{2\rho\omega^2} \left(-\nu_n (E_b + A_n^y E_{b0}) + \gamma_n (E_c + B_n^y E_{c0}) \right) \quad (\text{D.54})$$

$$\frac{\partial G_{yy}(k_n, k_z)}{\partial x} = -ik_n G_{yy}(k_n, k_z) \quad (\text{D.55})$$

$$\frac{\partial G_{yy}(k_n, k_z)}{\partial z} = -ik_z G_{yy}(k_n, k_z) \quad (\text{D.56})$$

$$\frac{\partial G_{zy}(k_n, k_z)}{\partial y} = \frac{k_z}{2\rho\omega^2} \left(-\nu_n (E_b + A_n^y E_{b0}) + \gamma_n (E_c + C_n^y E_{c0}) \right) \quad (\text{D.57})$$

$$\frac{\partial G_{zy}(k_n, k_z)}{\partial x} = -ik_n G_{zy}(k_n, k_z) \quad (\text{D.58})$$

$$\frac{\partial G_{xy}(k_n, k_z)}{\partial z} = -ik_z G_{xy}(k_n, k_z) \quad (\text{D.59})$$

$$\frac{\partial G_{xz}(k_n, k_z)}{\partial x} = -ik_n G_{xz}(k_n, k_z) \quad (\text{D.60})$$

$$\frac{\partial G_{yz}(k_n, k_z)}{\partial y} = \frac{k_z}{2\rho\omega^2} \left(-\nu_n (E_b + A_n^z E_{b0}) + \gamma_n (E_c + B_n^z E_{c0}) \right) \quad (\text{D.61})$$

$$\frac{\partial G_{zz}(k_n, k_z)}{\partial z} = -ik_z G_{zz}(k_n, k_z) \quad (\text{D.62})$$

$$\frac{\partial G_{xz}(k_n, k_z)}{\partial y} = \frac{k_n k_z}{2\rho\omega^2} \left(\text{sgn}(y - y_0) (-E_b + E_c) - A_n^z E_{b0} + C_n^z E_{c0} \right) \quad (\text{D.63})$$

$$\frac{\partial G_{yz}(k_n, k_z)}{\partial x} = -ik_n G_{yz}(k_n, k_z) \quad (\text{D.64})$$

$$\frac{\partial G_{yz}(k_n, k_z)}{\partial z} = -ik_z G_{yz}(k_n, k_z) \quad (\text{D.65})$$

$$\begin{aligned} \frac{\partial G_{zz}(k_n, k_z)}{\partial y} = \frac{-1}{2\rho\omega^2} & \left(k_z^2 (\text{sgn}(y - y_0)E_b + A_n^z E_{b0}) \dots \right. \\ & \left. + (\gamma_n^2 + k_n^2) \text{sgn}(y - y_0)E_c + (\gamma_n^2 B_n^z + k_n^2 C_n^z) E_{c0} \right) \end{aligned} \quad (\text{D.66})$$

$$\frac{\partial G_{zz}(k_n, k_z)}{\partial x} = -ik_n G_{zz}(k_n, k_z) \quad (\text{D.67})$$

$$\frac{\partial G_{xz}(k_n, k_z)}{\partial z} = -ik_z G_{xz}(k_n, k_z) \quad (\text{D.68})$$

In Eqs. (D.42)–(D.42), following relations hold:

- $k_n = -\xi^{\text{PiP}}, k_z = -\gamma^{\text{PiP}}$
- $k_p = \frac{\omega}{c_p}, k_s = \frac{\omega}{c_s}$
- $\nu_n = \sqrt{k_p^2 - k_z^2 - k_n^2}$ with $\Im(\nu_n) \leq 0$, $\gamma_n = \sqrt{k_s^2 - k_z^2 - k_n^2}$ with $\Im(\gamma_n) \leq 0$, $\nu_{zn} = \sqrt{-k_z^2 - k_n^2}$
- $E_b = e^{-i\nu_n|y-y_0|}, E_c = e^{-i\gamma_n|y-y_0|}$
- $E_{b0} = e^{-i\nu_n y}, E_{c0} = e^{-i\gamma_n y}$

The expressions for $G_{ij}(k_n, k_z)$ and the coefficients A_n^j, B_n^j and C_n^j can be found in [45].

Finally, a double inverse Fourier transformation is needed to find the displacements and stresses in the spatial-spatial-frequency domain. First¹, the transformation from wavenumber γ to spatial coordinate y is carried out, according to the definition in section A.2:

$$\tilde{u}_j(\xi, y) = \frac{1}{2\pi} \int_{-\infty}^{+\infty} \tilde{u}_j(\xi, \gamma) e^{i\gamma y} d\gamma \quad (\text{D.69})$$

$$\begin{aligned} &= \frac{1}{2\pi} \int_0^{+\infty} \tilde{u}_j(\xi, \gamma) \cos(\gamma y) d\gamma + \frac{1}{2\pi} \int_0^{+\infty} \tilde{u}_j(\xi, -\gamma) \cos(\gamma y) d\gamma \\ &+ \frac{i}{2\pi} \int_0^{+\infty} \tilde{u}_j(\xi, \gamma) \sin(\gamma y) d\gamma - \frac{i}{2\pi} \int_0^{+\infty} \tilde{u}_j(\xi, -\gamma) \sin(\gamma y) d\gamma \end{aligned} \quad (\text{D.70})$$

Likewise:

$$u_j(x, y) = \frac{1}{2\pi} \int_{-\infty}^{+\infty} \tilde{u}_j(\xi, y) e^{i\xi x} d\xi \quad (\text{D.71})$$

$$\begin{aligned} &= \frac{1}{2\pi} \int_0^{+\infty} \tilde{u}_j(\xi, y) \cos(\xi x) d\xi + \frac{1}{2\pi} \int_0^{+\infty} \tilde{u}_j(-\xi, y) \cos(\xi x) d\xi \\ &+ \frac{i}{2\pi} \int_0^{+\infty} \tilde{u}_j(\xi, y) \sin(\xi x) d\xi - \frac{i}{2\pi} \int_0^{+\infty} \tilde{u}_j(-\xi, y) \sin(\xi x) d\xi \end{aligned} \quad (\text{D.72})$$

Eqs. (D.70) and (D.72) can be simplified if the function $u_j(x, y)$ has specific properties, i.e. if it is real or imaginary, or odd or even. Table D.2 indicates the (anti)symmetry of the displacements $u_j(x, y)$ and stresses $\sigma_{ij}(x, y)$ with respect to the (y, z) - respectively (z, x) -plane. If a function $u_j(x, y)$ or $\sigma_{ij}(x, y)$ is even with respect to x or y , the sine terms in Eq. (D.70) or (D.72) must be zero. Analogously, if a function is odd, the cosine terms must be zero. Therefore, the equations for the displacements $u_j(x, y)$ and stresses $\sigma_{ij}(x, y)$ reduce to:

$$u_x(x, y) = \frac{1}{\pi^2} \int_0^{\infty} \int_0^{\infty} \tilde{u}_x(\xi, \gamma) i \sin(\xi x) \cos(\gamma y) d\xi d\gamma \quad (\text{D.73})$$

$$u_y(x, y) = \frac{1}{\pi^2} \int_0^{\infty} \int_0^{\infty} \tilde{u}_y(\xi, \gamma) \cos(\xi x) i \sin(\gamma y) d\xi d\gamma \quad (\text{D.74})$$

$$u_z(x, y) = \frac{1}{\pi^2} \int_0^{\infty} \int_0^{\infty} \tilde{u}_z(\xi, \gamma) \cos(\xi x) \cos(\gamma y) d\xi d\gamma \quad (\text{D.75})$$

¹The sequence of transformations is theoretically of no importance.

	(x, y)	$(-x, y)$	$(x, -y)$	$(-x, -y)$
u_x	+	-	+	-
u_y	+	+	-	-
u_z	+	+	+	+
σ_{xx}	+	+	+	+
σ_{yy}	+	+	+	+
σ_{zz}	+	+	+	+
σ_{xy}	+	-	-	+
σ_{yz}	+	+	-	-
σ_{zx}	+	-	+	-

Table D.2: (Anti)symmetry of the displacements $u_j(x, y)$ and stresses $\sigma_{ij}(x, y)$.

and

$$\sigma_{xx}(x, y) = \frac{1}{\pi^2} \int_0^\infty \int_0^\infty \tilde{\sigma}_{xx}(\xi, \gamma) \cos(\xi x) \cos(\gamma y) d\xi d\gamma \quad (\text{D.76})$$

$$\sigma_{yy}(x, y) = \frac{1}{\pi^2} \int_0^\infty \int_0^\infty \tilde{\sigma}_{yy}(\xi, \gamma) \cos(\xi x) \cos(\gamma y) d\xi d\gamma \quad (\text{D.77})$$

$$\sigma_{zz}(x, y) = \frac{1}{\pi^2} \int_0^\infty \int_0^\infty \tilde{\sigma}_{zz}(\xi, \gamma) \cos(\xi x) \cos(\gamma y) d\xi d\gamma \quad (\text{D.78})$$

$$\sigma_{xy}(x, y) = \frac{1}{\pi^2} \int_0^\infty \int_0^\infty \tilde{\sigma}_{xy}(\xi, \gamma) i \sin(\xi x) i \sin(\gamma y) d\xi d\gamma \quad (\text{D.79})$$

$$\sigma_{yz}(x, y) = \frac{1}{\pi^2} \int_0^\infty \int_0^\infty \tilde{\sigma}_{yz}(\xi, \gamma) \cos(\xi x) i \sin(\gamma y) d\xi d\gamma \quad (\text{D.80})$$

$$\sigma_{zx}(x, y) = \frac{1}{\pi^2} \int_0^\infty \int_0^\infty \tilde{\sigma}_{zx}(\xi, \gamma) i \sin(\xi x) \cos(\gamma y) d\xi d\gamma \quad (\text{D.81})$$

Appendix E

Matrix expressions

E.1 Two adjacent piles with unconstrained pile-heads

In paragraph 5.1.1, the equations for a two-pile model with unconstrained pile-heads are derived. It results finally in expressions for the pile displacements \mathbf{u}_p^A and \mathbf{u}_p^B in function of the different possible loads \mathbf{f}_{ph}^A , \mathbf{f}_{ph}^B and \mathbf{p}_{fs} :

$$\mathbf{u}_p^A = [\mathbf{E}]^{-1}[\mathbf{F}]\mathbf{f}_{ph}^A + [\mathbf{E}]^{-1}[\mathbf{G}]\mathbf{f}_{ph}^B + [\mathbf{E}]^{-1}[\mathbf{X}]\mathbf{p}_{fs} \quad (\text{E.1})$$

$$\mathbf{u}_p^B = [\mathbf{H}]^{-1}[\mathbf{I}]\mathbf{f}_{ph}^A + [\mathbf{H}]^{-1}[\mathbf{J}]\mathbf{f}_{ph}^B + [\mathbf{H}]^{-1}[\mathbf{Y}]\mathbf{p}_{fs} \quad (\text{E.2})$$

The expressions for the matrices $[\mathbf{E}]$, $[\mathbf{F}]$, $[\mathbf{G}]$ and $[\mathbf{X}]$ (as well for $[\mathbf{H}]$, $[\mathbf{I}]$, $[\mathbf{J}]$ and $[\mathbf{Y}]$) are summarized here:

$$[\mathbf{E}] = \mathbf{I} - b_p^A h_p^A b_p^B h_p^B [\mathbf{C}]^{-1} \mathbf{H}_p^{A22} \mathbf{Q}_1^{AT} [\mathbf{A}]^{-1} \dots \mathbf{H}_s^{23} [\mathbf{H}_s^{33}]^{-1} \mathbf{Q}_1^B [\mathbf{D}]^{-1} \mathbf{H}_p^{B22} \mathbf{Q}_1^{BT} [\mathbf{B}]^{-1} \mathbf{H}_s^{32} [\mathbf{H}_s^{22}]^{-1} \mathbf{Q}_1^A \quad (\text{E.3})$$

$$[\mathbf{F}] = [\mathbf{C}]^{-1} \mathbf{H}_p^{A21} \quad (\text{E.4})$$

$$[\mathbf{G}] = b_p^A h_p^A [\mathbf{C}]^{-1} \mathbf{H}_p^{A22} \mathbf{Q}_1^{AT} [\mathbf{A}]^{-1} \mathbf{H}_s^{23} [\mathbf{H}_s^{33}]^{-1} \mathbf{Q}_1^B [\mathbf{D}]^{-1} \mathbf{H}_p^{B21} \quad (\text{E.5})$$

$$[\mathbf{X}] = b_p^A h_p^A [\mathbf{C}]^{-1} \mathbf{H}_p^{A22} \mathbf{Q}_1^{AT} [\mathbf{A}]^{-1} \left(b_p^B h_p^B \mathbf{H}_s^{23} [\mathbf{H}_s^{33}]^{-1} \mathbf{Q}_1^B [\mathbf{D}]^{-1} \mathbf{H}_p^{B22} \mathbf{Q}_1^{BT} [\mathbf{B}]^{-1} \dots \right. \\ \left. \left(\mathbf{H}_s^{31} - \mathbf{H}_s^{32} [\mathbf{H}_s^{22}]^{-1} \mathbf{H}_s^{21} \right) + \left(\mathbf{H}_s^{21} - \mathbf{H}_s^{23} [\mathbf{H}_s^{33}]^{-1} \mathbf{H}_s^{31} \right) \right) \quad (\text{E.6})$$

and

$$[\mathbf{H}] = \mathbf{I} - b_p^A h_p^A b_p^B h_p^B [\mathbf{D}]^{-1} \mathbf{H}_p^{B22} \mathbf{Q}_1^{BT} [\mathbf{B}]^{-1} \dots$$

$$\mathbf{H}_s^{32} [\mathbf{H}_s^{22}]^{-1} \mathbf{Q}_1^A [\mathbf{C}]^{-1} \mathbf{H}_p^{A22} \mathbf{Q}_1^{AT} [\mathbf{A}]^{-1} \mathbf{H}_s^{23} [\mathbf{H}_s^{33}]^{-1} \mathbf{Q}_1^B \quad (\text{E.7})$$

$$[\mathbf{I}] = b_p^B h_p^B [\mathbf{D}]^{-1} \mathbf{H}_p^{A22} \mathbf{Q}_1^{BT} [\mathbf{B}]^{-1} \mathbf{H}_s^{32} [\mathbf{H}_s^{22}]^{-1} \mathbf{Q}_1^A [\mathbf{C}]^{-1} \mathbf{H}_p^{A21} \quad (\text{E.8})$$

$$[\mathbf{J}] = [\mathbf{D}]^{-1} \mathbf{H}_p^{B21} \quad (\text{E.9})$$

$$[\mathbf{Y}] = b_p^B h_p^B [\mathbf{D}]^{-1} \mathbf{H}_p^{B22} \mathbf{Q}_1^{BT} [\mathbf{B}]^{-1} \left(b_p^A h_p^A \mathbf{H}_s^{32} [\mathbf{H}_s^{22}]^{-1} \mathbf{Q}_1^A [\mathbf{C}]^{-1} \mathbf{H}_p^{A22} \mathbf{Q}_1^{AT} [\mathbf{A}]^{-1} \dots \right.$$

$$\left. \left(\mathbf{H}_s^{21} - \mathbf{H}_s^{23} [\mathbf{H}_s^{33}]^{-1} \mathbf{H}_s^{31} \right) + \left(\mathbf{H}_s^{31} - \mathbf{H}_s^{32} [\mathbf{H}_s^{22}]^{-1} \mathbf{H}_s^{21} \right) \right) \quad (\text{E.10})$$

It is clear that the matrices $[\mathbf{H}]$, $[\mathbf{I}]$, $[\mathbf{J}]$ and $[\mathbf{Y}]$ are completely analogous to the matrices $[\mathbf{E}]$, $[\mathbf{F}]$, $[\mathbf{G}]$ and $[\mathbf{X}]$: the superscripts A and B have to be reversed, as well as the superscripts 2 and 3 in the submatrices of \mathbf{H}_s .

The matrices $[\mathbf{A}]$, $[\mathbf{B}]$, $[\mathbf{C}]$ and $[\mathbf{D}]$ have already been defined in paragraph 5.1.1 and will not be repeated here.

E.2 Two adjacent piles with semi-infinite columns

The incorporation of semi-infinite columns in the two-pile model is considered in paragraph 5.2.1. It results in expressions for the pile displacements \mathbf{u}_p^A and \mathbf{u}_p^B in function of \mathbf{p}_{fs} :

$$\mathbf{u}_p^A = [\mathbf{T}_A]^{-1} [\mathbf{U}_A] \mathbf{p}_{fs} \quad (\text{E.11})$$

$$\mathbf{u}_p^B = [\mathbf{T}_B]^{-1} [\mathbf{U}_B] \mathbf{p}_{fs} \quad (\text{E.12})$$

Expressions for $[\mathbf{T}_A]$ and $[\mathbf{U}_A]$ are given below:

$$[\mathbf{T}_A] = [\mathbf{K}_A] - [\mathbf{M}_A] [\mathbf{K}_B]^{-1} [\mathbf{M}_B] \quad (\text{E.13})$$

$$[\mathbf{U}_A] = [\mathbf{N}_A] + [\mathbf{M}_A] [\mathbf{K}_B]^{-1} [\mathbf{N}_B] \quad (\text{E.14})$$

with

$$[\mathbf{L}_A] = \mathbf{I} + \mathbf{H}_p^{A11} [\mathbf{H}_b^A]^{-1} \quad (\text{E.15})$$

$$[\mathbf{K}_A] = \mathbf{I} + b_p^A h_p^A \left(\mathbf{H}_p^{A22} - \mathbf{H}_p^{A21} [\mathbf{H}_b^A]^{-1} [\mathbf{L}_A]^{-1} \mathbf{H}_p^{A12} \right) \mathbf{Q}_1^{AT} [\mathbf{A}]^{-1} \mathbf{Q}_1^A \quad (\text{E.16})$$

$$[\mathbf{M}_A] = b_p^A h_p^A \left(\mathbf{H}_p^{A22} - \mathbf{H}_p^{A21} [\mathbf{H}_b^A]^{-1} [\mathbf{L}_A]^{-1} \mathbf{H}_p^{A12} \right) \mathbf{Q}_1^{A T} [\mathbf{A}]^{-1} \mathbf{H}_s^{23} [\mathbf{H}_s^{33}]^{-1} \mathbf{Q}_1^B \quad (\text{E.17})$$

$$[\mathbf{N}_A] = b_p^A h_p^A \left(\mathbf{H}_p^{A22} - \mathbf{H}_p^{A21} [\mathbf{H}_b^A]^{-1} [\mathbf{L}_A]^{-1} \mathbf{H}_p^{A12} \right) \mathbf{Q}_1^{A T} [\mathbf{A}]^{-1} \left(\mathbf{H}_s^{21} - \mathbf{H}_s^{23} [\mathbf{H}_s^{33}]^{-1} \mathbf{H}_s^{31} \right) \quad (\text{E.18})$$

The matrices $[\mathbf{T}_B]$, $[\mathbf{U}_B]$, $[\mathbf{L}_B]$, $[\mathbf{K}_B]$, $[\mathbf{M}_B]$ and $[\mathbf{N}_B]$ are completely analogous to those given above.

E.3 Tunnel and piles with semi-infinite columns

In chapter 7, the response of piled foundations to underground railway induced loadings is investigated by means of a two-step approach. It results in expressions for the pile displacements in function of the stresses and displacements induced by the incident wavefield. Section E.3.1 gives expressions for the relevant matrices if two piles are considered, and section E.3.2 if four piles are considered.

E.3.1 Two piles

$$\mathbf{u}_p^A = [\eta_A]^{-1} [\Delta \mathbf{A} \mathbf{A}_u] \mathbf{u}_{sp}^{Ainc} + [\eta_A]^{-1} [\Delta \mathbf{A} \mathbf{A}_\sigma] \mathbf{p}_{sp}^{Ainc} + [\eta_A]^{-1} [\Delta \mathbf{A} \mathbf{B}_u] \mathbf{u}_{sp}^{Binc} + [\eta_A]^{-1} [\Delta \mathbf{A} \mathbf{B}_\sigma] \mathbf{p}_{sp}^{Binc} \quad (\text{E.19})$$

$$\mathbf{u}_p^B = [\eta_B]^{-1} [\Delta \mathbf{B} \mathbf{A}_u] \mathbf{u}_{sp}^{Ainc} + [\eta_B]^{-1} [\Delta \mathbf{B} \mathbf{A}_\sigma] \mathbf{p}_{sp}^{Ainc} + [\eta_B]^{-1} [\Delta \mathbf{B} \mathbf{B}_u] \mathbf{u}_{sp}^{Binc} + [\eta_B]^{-1} [\Delta \mathbf{B} \mathbf{B}_\sigma] \mathbf{p}_{sp}^{Binc} \quad (\text{E.20})$$

Expressions for $[\eta_A]$, $[\Delta \mathbf{A} \mathbf{A}_u]$, $[\Delta \mathbf{A} \mathbf{A}_\sigma]$, $[\Delta \mathbf{A} \mathbf{B}_u]$ and $[\Delta \mathbf{A} \mathbf{B}_\sigma]$ are given below:

$$[\eta_A] = [\mathbf{K}_A] - [\mathbf{M}_A] [\mathbf{K}_B]^{-1} [\mathbf{M}_B] \quad (\text{E.21})$$

$$[\Delta \mathbf{A} \mathbf{A}_u] = [\mathbf{Q}_A] + [\mathbf{M}_A] [\mathbf{K}_B]^{-1} [\mathbf{R}_B] \quad (\text{E.22})$$

$$[\Delta \mathbf{A} \mathbf{A}_\sigma] = -b_p^A h_p^A \left(\mathbf{H}_p^{A22} - \mathbf{H}_p^{A21} [\mathbf{H}_b^A]^{-1} [\mathbf{L}_A]^{-1} \mathbf{H}_p^{A12} \right) \mathbf{Q}_1^{A T} \quad (\text{E.23})$$

$$[\Delta \mathbf{A} \mathbf{B}_u] = [\mathbf{Q}_A] + [\mathbf{M}_A] [\mathbf{K}_B]^{-1} [\mathbf{Q}_B] \quad (\text{E.24})$$

$$[\Delta \mathbf{A} \mathbf{B}_\sigma] = [\mathbf{M}_A] [\mathbf{K}_B]^{-1} [\Delta \mathbf{B} \mathbf{B}_\sigma] \quad (\text{E.25})$$

with

$$[\mathbf{L}_A] = \mathbf{I} + \mathbf{H}_p^{A11} [\mathbf{H}_b^A]^{-1} \quad (\text{E.26})$$

$$[\mathbf{K}_A] = \mathbf{I} + b_p^A h_p^A \left(\mathbf{H}_p^{A22} - \mathbf{H}_p^{A21} [\mathbf{H}_b^A]^{-1} [\mathbf{L}_A]^{-1} \mathbf{H}_p^{A12} \right) \mathbf{Q}_1^{A T} [\mathbf{A}]^{-1} \mathbf{Q}_1^A \quad (\text{E.27})$$

$$[\mathbf{M}_A] = b_p^A h_p^A \left(\mathbf{H}_p^{A22} - \mathbf{H}_p^{A21} [\mathbf{H}_b^A]^{-1} [\mathbf{L}_A]^{-1} \mathbf{H}_p^{A12} \right) \mathbf{Q}_1^{A T} [\mathbf{A}]^{-1} \mathbf{H}_s^{23} [\mathbf{H}_s^{33}]^{-1} \mathbf{Q}_1^B \quad (\text{E.28})$$

$$[\mathbf{Q}_A] = b_p^A h_p^A \left(\mathbf{H}_p^{A22} - \mathbf{H}_p^{A21} [\mathbf{H}_b^A]^{-1} [\mathbf{L}_A]^{-1} \mathbf{H}_p^{A12} \right) \mathbf{Q}_1^{A T} [\mathbf{A}]^{-1} \quad (\text{E.29})$$

$$[\mathbf{R}_A] = -b_p^A h_p^A \left(\mathbf{H}_p^{A22} - \mathbf{H}_p^{A21} [\mathbf{H}_b^A]^{-1} [\mathbf{L}_A]^{-1} \mathbf{H}_p^{A12} \right) \mathbf{Q}_1^{A T} [\mathbf{A}]^{-1} \mathbf{H}_s^{23} [\mathbf{H}_s^{33}]^{-1} \quad (\text{E.30})$$

Again, the matrices $[\eta_B]$, $[\Delta \mathbf{B} \mathbf{B}_u]$, $[\Delta \mathbf{B} \mathbf{B}_\sigma]$, $[\Delta \mathbf{B} \mathbf{A}_u]$ and $[\Delta \mathbf{B} \mathbf{A}_\sigma]$ are completely analogous to those given above.

E.3.2 Four piles

$$\begin{aligned} \mathbf{u}_p^A &= [\eta_A]^{-1}[\Delta AA_u]\mathbf{u}_{sp}^{Ainc} + [\eta_A]^{-1}[\Delta AA_\sigma]\mathbf{p}_{sp}^{Ainc} + [\eta_A]^{-1}[\Delta AB_u]\mathbf{u}_{sp}^{Binc} + [\eta_A]^{-1}[\Delta AB_\sigma]\mathbf{p}_{sp}^{Binc} \\ &+ [\eta_A]^{-1}[\Delta AC_u]\mathbf{u}_{sp}^{Cinc} + [\eta_A]^{-1}[\Delta AC_\sigma]\mathbf{p}_{sp}^{Cinc} + [\eta_A]^{-1}[\Delta AD_u]\mathbf{u}_{sp}^{Dinc} + [\eta_A]^{-1}[\Delta AD_\sigma]\mathbf{p}_{sp}^{Dinc} \end{aligned} \quad (E.31)$$

$$\begin{aligned} \mathbf{u}_p^B &= [\eta_B]^{-1}[\Delta BA_u]\mathbf{u}_{sp}^{Ainc} + [\eta_B]^{-1}[\Delta BA_\sigma]\mathbf{p}_{sp}^{Ainc} + [\eta_B]^{-1}[\Delta BB_u]\mathbf{u}_{sp}^{Binc} + [\eta_B]^{-1}[\Delta BB_\sigma]\mathbf{p}_{sp}^{Binc} \\ &+ [\eta_B]^{-1}[\Delta BC_u]\mathbf{u}_{sp}^{Cinc} + [\eta_B]^{-1}[\Delta BC_\sigma]\mathbf{p}_{sp}^{Cinc} + [\eta_B]^{-1}[\Delta BD_u]\mathbf{u}_{sp}^{Dinc} + [\eta_B]^{-1}[\Delta BD_\sigma]\mathbf{p}_{sp}^{Dinc} \end{aligned} \quad (E.32)$$

$$\begin{aligned} \mathbf{u}_p^C &= [\eta_C]^{-1}[\Delta CA_u]\mathbf{u}_{sp}^{Ainc} + [\eta_C]^{-1}[\Delta CA_\sigma]\mathbf{p}_{sp}^{Ainc} + [\eta_C]^{-1}[\Delta CB_u]\mathbf{u}_{sp}^{Binc} + [\eta_C]^{-1}[\Delta CB_\sigma]\mathbf{p}_{sp}^{Binc} \\ &+ [\eta_C]^{-1}[\Delta CC_u]\mathbf{u}_{sp}^{Cinc} + [\eta_C]^{-1}[\Delta CC_\sigma]\mathbf{p}_{sp}^{Cinc} + [\eta_C]^{-1}[\Delta CD_u]\mathbf{u}_{sp}^{Dinc} + [\eta_C]^{-1}[\Delta CD_\sigma]\mathbf{p}_{sp}^{Dinc} \end{aligned} \quad (E.33)$$

$$\begin{aligned} \mathbf{u}_p^D &= [\eta_D]^{-1}[\Delta DA_u]\mathbf{u}_{sp}^{Ainc} + [\eta_D]^{-1}[\Delta DA_\sigma]\mathbf{p}_{sp}^{Ainc} + [\eta_D]^{-1}[\Delta DB_u]\mathbf{u}_{sp}^{Binc} + [\eta_D]^{-1}[\Delta DB_\sigma]\mathbf{p}_{sp}^{Binc} \\ &+ [\eta_D]^{-1}[\Delta DC_u]\mathbf{u}_{sp}^{Cinc} + [\eta_D]^{-1}[\Delta DC_\sigma]\mathbf{p}_{sp}^{Cinc} + [\eta_D]^{-1}[\Delta DD_u]\mathbf{u}_{sp}^{Dinc} + [\eta_D]^{-1}[\Delta DD_\sigma]\mathbf{p}_{sp}^{Dinc} \end{aligned} \quad (E.34)$$

Expressions for $[\eta_A]$, $[\Delta AA_u]$, $[\Delta AA_\sigma]$, $[\Delta AB_u]$, $[\Delta AB_\sigma]$, $[\Delta AC_u]$, $[\Delta AC_\sigma]$, $[\Delta AD_u]$ and $[\Delta AD_\sigma]$ are given below. Expressions for the other matrices are completely analogous to those presented here.

$$\begin{aligned} [\eta_A] &= [\xi_A] - [\psi_{AB}][\mathbf{YB}]^{-1}[\mathbf{YA}] - [\psi_{AD}][\xi_D]^{-1}([\psi_{DA}] + [\psi_{DB}][\mathbf{YB}]^{-1}[\mathbf{YA}]) \\ &\quad - ([\psi_{AC}] + [\psi_{AD}][\xi_D]^{-1}[\psi_{DC}])[\mathbf{XC}]^{-1}([\mathbf{XA}] + [\mathbf{XB}][\mathbf{YB}]^{-1}[\mathbf{YA}]) \end{aligned} \quad (E.35)$$

$$\begin{aligned} [\Delta AA_u] &= ([\psi_{AC}] + [\psi_{AD}][\xi_D]^{-1}[\psi_{DC}])[\mathbf{XC}]^{-1}[\mathbf{XBFA}] + [\psi_{AD}][\xi_D]^{-1}[\eta_{DA}] + [\eta_{AA}] \dots \\ &\quad + ([\psi_{AB}] + [\psi_{AC}][\mathbf{XC}]^{-1}[\mathbf{XB}]) \dots \\ &\quad + [\psi_{AD}][\xi_D]^{-1}([\psi_{DB}] + [\psi_{DC}][\mathbf{XC}]^{-1}[\mathbf{XB}])[\mathbf{YB}]^{-1}[\mathbf{YBFA}] \end{aligned} \quad (E.36)$$

$$[\Delta AA_\sigma] = [\zeta_A] \quad (E.37)$$

$$\begin{aligned} [\Delta AB_u] &= ([\psi_{AC}] + [\psi_{AD}][\xi_D]^{-1}[\psi_{DC}])[\mathbf{XC}]^{-1}[\mathbf{XBFB}] + [\psi_{AD}][\xi_D]^{-1}[\eta_{DB}] + [\eta_{AB}] \dots \\ &\quad + ([\psi_{AB}] + [\psi_{AC}][\mathbf{XC}]^{-1}[\mathbf{XB}]) \dots \\ &\quad + [\psi_{AD}][\xi_D]^{-1}([\psi_{DB}] + [\psi_{DC}][\mathbf{XC}]^{-1}[\mathbf{XB}])[\mathbf{YB}]^{-1}[\mathbf{YBFB}] \end{aligned} \quad (E.38)$$

$$\begin{aligned} [\Delta AB_\sigma] &= ([\psi_{AB}] + [\psi_{AC}][\mathbf{XC}]^{-1}[\mathbf{XB}]) \dots \\ &\quad + [\psi_{AD}][\xi_D]^{-1}([\psi_{DB}] + [\psi_{DC}][\mathbf{XC}]^{-1}[\mathbf{XB}])[\mathbf{YB}]^{-1}[\zeta_B] \end{aligned} \quad (E.39)$$

$$\begin{aligned} [\Delta AC_u] &= ([\psi_{AC}] + [\psi_{AD}][\xi_D]^{-1}[\psi_{DC}])[\mathbf{XC}]^{-1}[\mathbf{XBFC}] + [\psi_{AD}][\xi_D]^{-1}[\eta_{DC}] + [\eta_{AC}] \dots \\ &\quad + ([\psi_{AB}] + [\psi_{AC}][\mathbf{XC}]^{-1}[\mathbf{XB}]) \dots \\ &\quad + [\psi_{AD}][\xi_D]^{-1}([\psi_{DB}] + [\psi_{DC}][\mathbf{XC}]^{-1}[\mathbf{XB}])[\mathbf{YB}]^{-1}[\mathbf{YBFC}] \end{aligned} \quad (E.40)$$

$$[\Delta \mathbf{A} \mathbf{C}_\sigma] = \left([\psi_{AC}] + [\psi_{AD}][\xi_D]^{-1}[\psi_{DC}] \right) [\mathbf{X} \mathbf{C}]^{-1} [\zeta_C] + \left([\psi_{AB}] + [\psi_{AC}][\mathbf{X} \mathbf{C}]^{-1} [\mathbf{X} \mathbf{B}] \dots \right. \\ \left. + [\psi_{AD}][\xi_D]^{-1} \left([\psi_{DB}] + [\psi_{DC}][\mathbf{X} \mathbf{C}]^{-1} [\mathbf{X} \mathbf{B}] \right) \right) [\mathbf{Y} \mathbf{B}]^{-1} [\mathbf{Y} \mathbf{P} \mathbf{B} \mathbf{F} \mathbf{C}] \quad (\text{E.41})$$

$$[\Delta \mathbf{A} \mathbf{D}_u] = \left([\psi_{AC}] + [\psi_{AD}][\xi_D]^{-1}[\psi_{DC}] \right) [\mathbf{X} \mathbf{C}]^{-1} [\mathbf{X} \mathbf{B} \mathbf{F} \mathbf{D}] + [\psi_{AD}][\xi_D]^{-1} [\eta_{DD}] + [\eta_{AD}] \dots \\ + \left([\psi_{AB}] + [\psi_{AC}][\mathbf{X} \mathbf{C}]^{-1} [\mathbf{X} \mathbf{B}] \dots \right. \\ \left. + [\psi_{AD}][\xi_D]^{-1} \left([\psi_{DB}] + [\psi_{DC}][\mathbf{X} \mathbf{C}]^{-1} [\mathbf{X} \mathbf{B}] \right) \right) [\mathbf{Y} \mathbf{B}]^{-1} [\mathbf{Y} \mathbf{B} \mathbf{F} \mathbf{D}] \quad (\text{E.42})$$

$$[\Delta \mathbf{A} \mathbf{D}_\sigma] = \left(\left([\psi_{AC}] + [\psi_{AD}][\xi_D]^{-1}[\psi_{DC}] \right) [\mathbf{X} \mathbf{C}]^{-1} [\psi_{CD}] + [\psi_{AD}] \right) [\xi_D]^{-1} [\xi_D]^{-1} \dots \\ + \left([\psi_{AB}] + [\psi_{AC}][\mathbf{X} \mathbf{C}]^{-1} [\mathbf{X} \mathbf{B}] \dots \right. \\ \left. + [\psi_{AD}][\xi_D]^{-1} \left([\psi_{DB}] + [\psi_{DC}][\mathbf{X} \mathbf{C}]^{-1} [\mathbf{X} \mathbf{B}] \right) \right) [\mathbf{Y} \mathbf{B}]^{-1} [\mathbf{Y} \mathbf{P} \mathbf{B} \mathbf{F} \mathbf{D}] \quad (\text{E.43})$$

with

$$[\mathbf{a}] = \mathbf{I} - [\mathbf{H}_s^{44}]^{-1} \mathbf{H}_s^{45} [\mathbf{H}_s^{55}]^{-1} \mathbf{H}_s^{54} \quad (\text{E.44})$$

$$[\mathbf{b}] = [\mathbf{H}_s^{44}]^{-1} \left(\mathbf{H}_s^{45} [\mathbf{H}_s^{55}]^{-1} \mathbf{H}_s^{52} - \mathbf{H}_s^{42} \right) \quad (\text{E.45})$$

$$[\mathbf{c}] = [\mathbf{H}_s^{44}]^{-1} \left(\mathbf{H}_s^{45} [\mathbf{H}_s^{55}]^{-1} \mathbf{H}_s^{53} - \mathbf{H}_s^{43} \right) \quad (\text{E.46})$$

$$[\mathbf{d}] = \mathbf{I} + [\mathbf{H}_s^{33}]^{-1} \left(\mathbf{H}_s^{34} [\mathbf{a}]^{-1} [\mathbf{c}] - \mathbf{H}_s^{35} [\mathbf{H}_s^{55}]^{-1} \left(\mathbf{H}_s^{53} - \mathbf{H}_s^{54} [\mathbf{a}]^{-1} [\mathbf{c}] \right) \right) \quad (\text{E.47})$$

$$[\mathbf{e}] = [\mathbf{H}_s^{33}]^{-1} \left(\mathbf{H}_s^{35} [\mathbf{H}_s^{55}]^{-1} \mathbf{H}_s^{54} - \mathbf{H}_s^{34} \right) [\mathbf{a}]^{-1} [\mathbf{H}_s^{44}]^{-1} \quad (\text{E.48})$$

$$[\mathbf{f}] = [\mathbf{H}_s^{33}]^{-1} \left(\left(\mathbf{H}_s^{34} - \mathbf{H}_s^{35} [\mathbf{H}_s^{55}]^{-1} \mathbf{H}_s^{54} \right) [\mathbf{a}]^{-1} [\mathbf{H}_s^{44}]^{-1} \mathbf{H}_s^{45} - \mathbf{H}_s^{35} \right) [\mathbf{H}_s^{55}]^{-1} \quad (\text{E.49})$$

$$[\mathbf{g}] = [\mathbf{H}_s^{33}]^{-1} \left(-\mathbf{H}_s^{32} + \mathbf{H}_s^{35} [\mathbf{H}_s^{55}]^{-1} \left(\mathbf{H}_s^{52} + \mathbf{H}_s^{54} [\mathbf{a}]^{-1} [\mathbf{b}] \right) - \mathbf{H}_s^{34} [\mathbf{a}]^{-1} [\mathbf{b}] \right) \quad (\text{E.50})$$

$$[\mathbf{A} \mathbf{A}] = \mathbf{H}_s^{22} + \mathbf{H}_s^{23} [\mathbf{d}]^{-1} [\mathbf{g}] + \mathbf{H}_s^{34} [\mathbf{a}]^{-1} \left([\mathbf{b}] + [\mathbf{c}] [\mathbf{d}]^{-1} [\mathbf{g}] \right) \dots \\ - \mathbf{H}_s^{25} [\mathbf{H}_s^{55}]^{-1} \left(\mathbf{H}_s^{52} + \left(\mathbf{H}_s^{53} + \mathbf{H}_s^{54} [\mathbf{a}]^{-1} [\mathbf{c}] \right) [\mathbf{d}]^{-1} [\mathbf{g}] + \mathbf{H}_s^{54} [\mathbf{a}]^{-1} [\mathbf{b}] [\mathbf{d}]^{-1} [\mathbf{g}] \right) \quad (\text{E.51})$$

$$[\mathbf{A} \mathbf{B}] = \left(-\mathbf{H}_s^{23} [\mathbf{d}]^{-1} - \mathbf{H}_s^{24} [\mathbf{a}]^{-1} [\mathbf{c}] [\mathbf{d}]^{-1} \dots \right. \\ \left. + \mathbf{H}_s^{25} [\mathbf{H}_s^{55}]^{-1} \left(\mathbf{H}_s^{53} + \mathbf{H}_s^{54} [\mathbf{a}]^{-1} [\mathbf{c}] \right) [\mathbf{d}]^{-1} \right) [\mathbf{H}_s^{33}]^{-1} \quad (\text{E.52})$$

$$[\mathbf{A} \mathbf{C}] = -\mathbf{H}_s^{23} [\mathbf{d}]^{-1} [\mathbf{e}] - \mathbf{H}_s^{24} [\mathbf{a}]^{-1} \left([\mathbf{H}_s^{44}]^{-1} + [\mathbf{c}] [\mathbf{d}]^{-1} [\mathbf{e}] \right) \dots \\ + \mathbf{H}_s^{25} [\mathbf{H}_s^{55}]^{-1} \left(\mathbf{H}_s^{53} [\mathbf{d}]^{-1} [\mathbf{e}] + \mathbf{H}_s^{54} [\mathbf{a}]^{-1} \left([\mathbf{H}_s^{44}]^{-1} + [\mathbf{c}] [\mathbf{d}]^{-1} [\mathbf{e}] \right) \right) \quad (\text{E.53})$$

$$[\mathbf{A} \mathbf{D}] = -\mathbf{H}_s^{23} [\mathbf{d}]^{-1} [\mathbf{f}] + \mathbf{H}_s^{24} [\mathbf{a}]^{-1} \left([\mathbf{H}_s^{44}]^{-1} [\mathbf{H}_s^{45}] [\mathbf{H}_s^{55}]^{-1} - [\mathbf{c}] [\mathbf{d}]^{-1} [\mathbf{f}] \right) \dots \\ + \mathbf{H}_s^{25} [\mathbf{H}_s^{55}]^{-1} \left(-\mathbf{I} + \mathbf{H}_s^{53} [\mathbf{d}]^{-1} [\mathbf{f}] \dots \right. \\ \left. + \mathbf{H}_s^{54} [\mathbf{a}]^{-1} \left(-[\mathbf{H}_s^{44}]^{-1} [\mathbf{H}_s^{45}] [\mathbf{H}_s^{55}]^{-1} + [\mathbf{c}] [\mathbf{d}]^{-1} [\mathbf{f}] \right) \right) \quad (\text{E.54})$$

$$[\xi_A] = \mathbf{I} + b_p^A h_p^A \left(\mathbf{H}_p^{A22} - \mathbf{H}_p^{A21} [\mathbf{H}_b^A]^{-1} [\mathbf{L}_A]^{-1} \mathbf{H}_p^{A12} \right) \mathbf{Q}_1^{A\top} [\mathbf{A}\mathbf{A}]^{-1} \mathbf{Q}_1^A \quad (\text{E.55})$$

$$[\psi_{AB}] = -b_p^A h_p^A \left(\mathbf{H}_p^{A22} - \mathbf{H}_p^{A21} [\mathbf{H}_b^A]^{-1} [\mathbf{L}_A]^{-1} \mathbf{H}_p^{A12} \right) \mathbf{Q}_1^{A\top} [\mathbf{A}\mathbf{A}]^{-1} [\mathbf{A}\mathbf{B}] \mathbf{Q}_1^B \quad (\text{E.56})$$

$$[\psi_{AC}] = -b_p^A h_p^A \left(\mathbf{H}_p^{A22} - \mathbf{H}_p^{A21} [\mathbf{H}_b^A]^{-1} [\mathbf{L}_A]^{-1} \mathbf{H}_p^{A12} \right) \mathbf{Q}_1^{A\top} [\mathbf{A}\mathbf{A}]^{-1} [\mathbf{A}\mathbf{C}] \mathbf{Q}_1^C \quad (\text{E.57})$$

$$[\psi_{AD}] = -b_p^A h_p^A \left(\mathbf{H}_p^{A22} - \mathbf{H}_p^{A21} [\mathbf{H}_b^A]^{-1} [\mathbf{L}_A]^{-1} \mathbf{H}_p^{A12} \right) \mathbf{Q}_1^{A\top} [\mathbf{A}\mathbf{A}]^{-1} [\mathbf{A}\mathbf{D}] \mathbf{Q}_1^D \quad (\text{E.58})$$

$$[\zeta_A] = -b_p^A h_p^A \left(\mathbf{H}_p^{A22} - \mathbf{H}_p^{A21} [\mathbf{H}_b^A]^{-1} [\mathbf{L}_A]^{-1} \mathbf{H}_p^{A12} \right) \mathbf{Q}_1^{A\top} \quad (\text{E.59})$$

$$[\eta_{AA}] = b_p^A h_p^A \left(\mathbf{H}_p^{A22} - \mathbf{H}_p^{A21} [\mathbf{H}_b^A]^{-1} [\mathbf{L}_A]^{-1} \mathbf{H}_p^{A22} \right) \mathbf{Q}_1^{A\top} [\mathbf{A}\mathbf{A}]^{-1} \quad (\text{E.60})$$

$$[\eta_{AB}] = b_p^A h_p^A \left(\mathbf{H}_p^{A22} - \mathbf{H}_p^{A21} [\mathbf{H}_b^A]^{-1} [\mathbf{L}_A]^{-1} \mathbf{H}_p^{A22} \right) \mathbf{Q}_1^{A\top} [\mathbf{A}\mathbf{A}]^{-1} [\mathbf{A}\mathbf{B}] \quad (\text{E.61})$$

$$[\eta_{AC}] = b_p^A h_p^A \left(\mathbf{H}_p^{A22} - \mathbf{H}_p^{A21} [\mathbf{H}_b^A]^{-1} [\mathbf{L}_A]^{-1} \mathbf{H}_p^{A22} \right) \mathbf{Q}_1^{A\top} [\mathbf{A}\mathbf{A}]^{-1} [\mathbf{A}\mathbf{C}] \quad (\text{E.62})$$

$$[\eta_{AD}] = b_p^A h_p^A \left(\mathbf{H}_p^{A22} - \mathbf{H}_p^{A21} [\mathbf{H}_b^A]^{-1} [\mathbf{L}_A]^{-1} \mathbf{H}_p^{A22} \right) \mathbf{Q}_1^{A\top} [\mathbf{A}\mathbf{A}]^{-1} [\mathbf{A}\mathbf{D}] \quad (\text{E.63})$$

$$[\mathbf{X}\mathbf{C}] = [\xi_C] - [\psi_{CD}] [\xi_D]^{-1} [\psi_{DC}] \quad (\text{E.64})$$

$$[\mathbf{X}\mathbf{A}] = [\psi_{CA}] + [\psi_{CD}] [\xi_D]^{-1} [\psi_{DA}] \quad (\text{E.65})$$

$$[\mathbf{X}\mathbf{B}] = [\psi_{CB}] + [\psi_{CD}] [\xi_D]^{-1} [\psi_{DB}] \quad (\text{E.66})$$

$$[\mathbf{X}\mathbf{B}\mathbf{F}\mathbf{A}] = [\eta_{CA}] + [\psi_{CD}] [\xi_D]^{-1} [\eta_{DA}] \quad (\text{E.67})$$

$$[\mathbf{X}\mathbf{B}\mathbf{F}\mathbf{B}] = [\eta_{CB}] + [\psi_{CD}] [\xi_D]^{-1} [\eta_{DB}] \quad (\text{E.68})$$

$$[\mathbf{X}\mathbf{B}\mathbf{F}\mathbf{C}] = [\eta_{CC}] + [\psi_{CD}] [\xi_D]^{-1} [\eta_{DC}] \quad (\text{E.69})$$

$$[\mathbf{X}\mathbf{B}\mathbf{F}\mathbf{D}] = [\eta_{CD}] + [\psi_{CD}] [\xi_D]^{-1} [\eta_{DD}] \quad (\text{E.70})$$

$$[\mathbf{Y}\mathbf{B}] = [\xi_B] - [\psi_{CD}] [\mathbf{X}\mathbf{C}]^{-1} [\mathbf{X}\mathbf{B}] - [\psi_{BD}] [\xi_D]^{-1} \left([\psi_{DB} + [\psi_{DC}]] [\mathbf{X}\mathbf{C}]^{-1} [\mathbf{X}\mathbf{B}] \right) \quad (\text{E.71})$$

$$[\mathbf{Y}\mathbf{A}] = [\psi_{BA}] + [\psi_{BC}] [\mathbf{X}\mathbf{C}]^{-1} [\mathbf{X}\mathbf{A}] + [\psi_{BD}] [\xi_D]^{-1} \left([\psi_{DA} + [\psi_{DC}]] [\mathbf{X}\mathbf{C}]^{-1} [\mathbf{X}\mathbf{A}] \right) \quad (\text{E.72})$$

$$[\mathbf{Y}\mathbf{P}\mathbf{B}\mathbf{F}\mathbf{C}] = \left([\psi_{BC}] + [\psi_{BD}] [\xi_D]^{-1} [\psi_{DC}] \right) [\mathbf{X}\mathbf{C}]^{-1} [\zeta_C] \quad (\text{E.73})$$

$$[\mathbf{Y}\mathbf{P}\mathbf{B}\mathbf{F}\mathbf{D}] = \left(\left([\psi_{BC}] + [\psi_{BD}] [\xi_D]^{-1} [\psi_{DC}] \right) \mathbf{X}\mathbf{C}^{-1} [\psi_{CD}] + [\psi_{BD}] \right) [\xi_D]^{-1} \zeta_D \quad (\text{E.74})$$

$$[\mathbf{Y}\mathbf{B}\mathbf{F}\mathbf{A}] = \left([\psi_{BC}] + [\psi_{BD}] [\xi_D]^{-1} [\psi_{DC}] \right) [\mathbf{X}\mathbf{C}]^{-1} [\mathbf{X}\mathbf{B}\mathbf{F}\mathbf{A}] + [\psi_{BD}] [\xi_D]^{-1} [\eta_{DA}] + [\eta_{BA}] \quad (\text{E.75})$$

$$[\mathbf{Y}\mathbf{B}\mathbf{F}\mathbf{B}] = \left([\psi_{BC}] + [\psi_{BD}] [\xi_D]^{-1} [\psi_{DC}] \right) [\mathbf{X}\mathbf{C}]^{-1} [\mathbf{X}\mathbf{B}\mathbf{F}\mathbf{B}] + [\psi_{BD}] [\xi_D]^{-1} [\eta_{DB}] + [\eta_{BB}] \quad (\text{E.76})$$

$$[\mathbf{Y}\mathbf{B}\mathbf{F}\mathbf{C}] = \left([\psi_{BC}] + [\psi_{BD}] [\xi_D]^{-1} [\psi_{DC}] \right) [\mathbf{X}\mathbf{C}]^{-1} [\mathbf{X}\mathbf{B}\mathbf{F}\mathbf{C}] + [\psi_{BD}] [\xi_D]^{-1} [\eta_{DC}] + [\eta_{BC}] \quad (\text{E.77})$$

$$[\mathbf{Y}\mathbf{B}\mathbf{F}\mathbf{D}] = \left([\psi_{BC}] + [\psi_{BD}] [\xi_D]^{-1} [\psi_{DC}] \right) [\mathbf{X}\mathbf{C}]^{-1} [\mathbf{X}\mathbf{B}\mathbf{F}\mathbf{D}] + [\psi_{BD}] [\xi_D]^{-1} [\eta_{DD}] + [\eta_{BD}] \quad (\text{E.78})$$

